Velocity imaging and monitoring based on seismic noise
What some studies don´t tell

Marco Pilz

Swiss Seismological Service

Swiss Federal Institute of Technology

Stefano Parolai

German Research Center for

Geosciences

2 September 2016

Array analysis for site characterization

Aki in 1957 proposed the analysis of ambient seismic noise as a tool for investigating the S-wave velocity structure below a site.

This S-wave velocity structure can be used to calculate the site response by numerical simulations. He derived dispersion curves by analyzing the correlation between noise recordings made at sites close to each other.

22. *Space and Time Spectra of Stationary Stochastic Waves, with Special Reference to Microtremors.*

By Keiiti AKI,

Earthquake Research Institute.

(Read May 28, 1957.—Received June 30, 1957.)

Array analysis for site characterization

However, although most popular, Aki was not the first one.

It has been known since the 1950s that surface wave information can be extracted from ambient seismic noise using correlation techniques (Eckart 1953, Akamatu 1956, Tomoda 1956).

The theory of noise in continous media
Carl Eckart

JOURNAL OF PHYSICS OF THE EARTH, VOL. 4, NO. 2, 1956.

A Simple Method for Calculating the Correlation Coefficients.

By
Yoshibumi TOMODA
Geophysical Institute, Faculty of Science, Tokyo University.

JOURNAL OF PHYSICS OF THE EARTH, VOL. 4, NO. 2, 1956

TOMODA's Method for Calculating the Correlation Coefficients as Applied to Microtremor Analysis.

By
Kei AKAMATU
Geophysical Institute, Faculty of Science, Tokyo University, Tokyo.

Array analysis for site characterization

In particular, Aki was aware of this fact.

It is well known that the characteristics of the ground are reflected more or less in its vibration whatever the origin of the vibration may be. This fact was noticed early in the beginning of this century by K. Sekiya and F. Omori who made a comparative study of seismograms recorded at Hongo and Hitotsubashi, both in Tokyo. Later, many Japanese seismologists studied ground vibrations from the view point of frequency spectrum. Among them, M. Ishimoto[6] (1937) made a systematic study both of vibrations due to earthquakes and of the background tremors, and proposed a hypothesis that the predominant period of vibration due to earthquakes coincides with that of the background tremors.

Though some negative results against the above hypothesis have been obtained by P. Byerly[7] (1947) and by K. Aki[8] (1955), the spectral study of the background tremors was succeeded in by various authors.

Y. Tomoda and K. Aki[9] (1952) made a frequency analysis by the use of a spectrometer, and confirmed the fact that vibrations having frequencies higher than 1 c/s are due to traffic. K. Kanai, T. Tanaka and K. Osada[10] (1954) made an extensive study and showed that the form of the spectral distribution of microtremors coincides with that of earthquake motions, and that it depends on the geology of the place. K. Akamatu[11] (1956) investigated the tremors observed at Hongo in more detail from the view point of correlograms in space and time.

Array analysis for site characterization

In particular, Aki was aware of this fact.

Those studies have been primarily concerned with the spectrum of waves in time, while the spectrum in space has not yet attracted due attentions. The recent study by K. Akamatsu[1] (1956) of the autocorrelation of microtremor waves in space is among the few made on the latter subject. She has made clear the spatial character of vibration of the ground. The process for obtaining the spatial autocorrelation coefficient, however, consists of troublesome steps such as simultanous recordings of vibrations at several points, readings of the recorded amplitudes, and computations of the autocorrelation coefficient among the waves to be studied. In order to secure rapidness and efficiency of measurments in the study of this kind, K. Aki[2] (1956) built a simple automatic computer by which the computation of spatial autocorrelation coefficients can be made without following individual steps stated above.

Array analysis for site characterization

In particular, Aki was aware of this fact.

In the study of waves from the viewpoint of "phases", the recording of vibration is essential for identifying the phases and for reading travel times. In our method, on the other hand, what we need is not the original record, but the result of the above described operations applied to them. Those operations may be carried out manually, but it should be emphasized that the troublesome labours involved in the manual operations make the application of our method practically impossible. The present study has been made possible by the automation of the operations. In fact, the theoretical studies given in Chapter 1 were initiated after the completion of a correlation computer in our laboratory, though the use of filters in our method was based on the theoretical results.

Important remarks on the importance of the chosen seismometer

tremors is 1/10 second. Of course, not only the pulse interval but also the frequency range of the resonator and the characteristics of the seismometers should be appropriate to the spectral nature of the waves concerned. The whole apparatus designed for microtremors will be ap-

Bulletin of the Seismological Society of America, Vol. 98, No. 2, pp. 671–681, April 2008, doi: 10.1785/0120070055

Suitability of Short-Period Sensors for Retrieving Reliable H/V Peaks for Frequencies Less Than 1 Hz

by A. Strollo, S. Parolai, K.-H. Jäckel, S. Marzorati, and D. Bindi

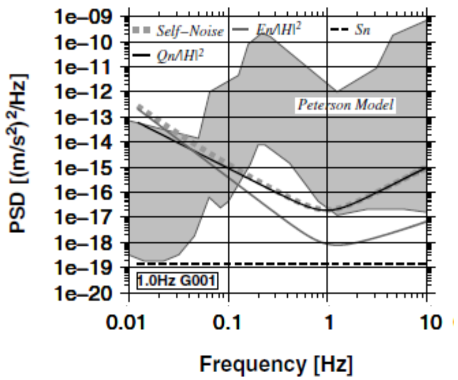

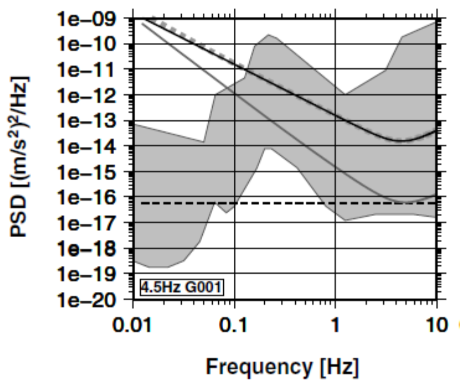

Important remarks on the importance of the duration of selected signal

As far as we are concerned with almost perfectly stationary waves, that is waves having sufficiently long durations that we can, not only obtain the correlation coefficients from large samples, but also repeat the measurement several times under the same circumstances, we need only one set of apparatus, i.e. a pair of seismometers, a pair of filters, and one correlation computer. There is, however, another important

Bulletin of the Seismological Society of America, Vol. 95, No. 5, pp. 1779–1786, October 2005, doi: 10.1785/0120040152

Statistical Analysis of Noise Horizontal-to-Vertical Spectral Ratios (HVSR)

by Matteo Picozzi, Stefano Parolai, and Dario Albarello

Composition of the noise wavefield

Microseisms: Mode Structure and Sources

M. Nafi Toksöz[1], Richard T. Lacoss[1]

+ Author Affiliations

Science 23 Feb 1968:

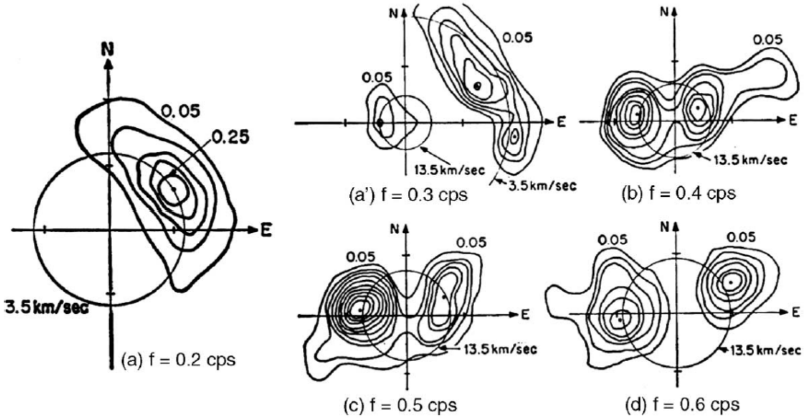

At 0.2 Hz, phase velocity is around 3.5 km/h
→ 1st or 2nd higher mode Rayleigh waves

At 0.3 Hz, there are two distinct velocities corresponding to Rayleigh waves and P waves

Between 0.4 and 0.6 Hz only P wave velocities can be observed.

Composition of the noise wavefield

Bulletin of the Seismological Society of America. Vol. 57, No. 1, pp. 55–81. February, 1967

SHORT-PERIOD SEISMIC NOISE

By E. J. Douze

Comparing Fourier spectra amplitudes with theoretical values for Rayleigh and P waves

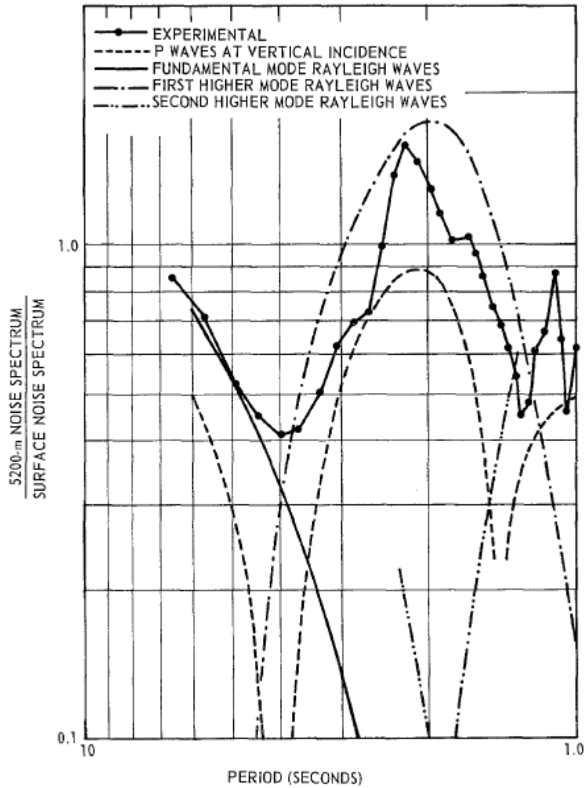

Fig. 2. Deep-hole (5200 m) vertical noise spectrum divided by surface noise spectrum. Theoretical amplitudes are included. FO-TX 300 sec sample, 10 samples/sec, 5 per cent lags.

Composition of the wavefield

Geophys. J. Int. (2006) 167, 827–837 doi: 10.1111/j.1365-246X.2006.03154.x

H/V ratio: a tool for site effects evaluation. Results from 1-D noise simulations

Sylvette Bonnefoy-Claudet,[1,*] Cécile Cornou,[1,2] Pierre-Yves Bard,[1,3] Fabrice Cotton,[1] Peter Moczo,[4,5] Jozef Kristek[4,5] and Donat Fäh[2]

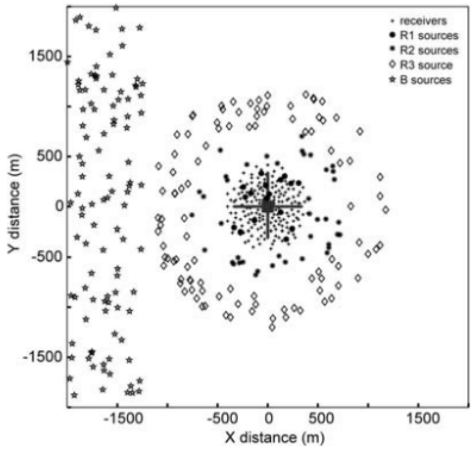

Relative portion of Rayleigh and body waves is linked to the distribution of noise sources

Deep sources → only non-dispersive body waves

Surface sources → if distant, then mixture of Rayleigh and body waves
if close, then mainly fundamental mode Rayleigh waves

H/V spectral ratio

Geophys. J. Int. (2006) 167, 827–837 doi: 10.1111/j.1365-246X.2006.03154.x

H/V ratio: a tool for site effects evaluation. Results from 1-D noise simulations

Sylvette Bonnefoy-Claudet,[1,*] Cécile Cornou,[1,2] Pierre-Yves Bard,[1,3] Fabrice Cott
Peter Moczo,[4,5] Jozef Kristek[4,5] and Donat Fäh[2]

free surface

soft layer

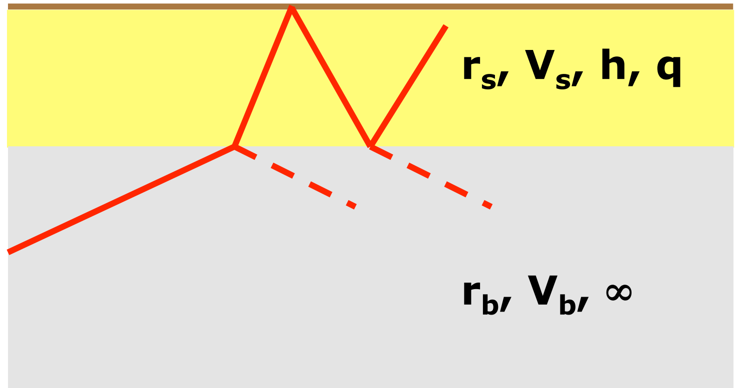

rock layer

Fourier spectra

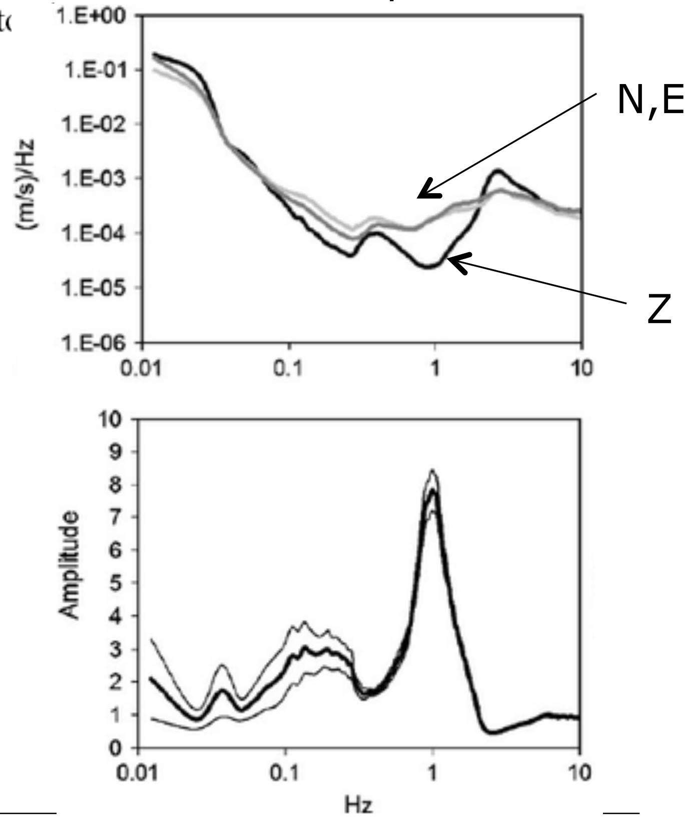

H/V spectral ratio

Using seismic noise to estimate the characteristics of a site

Procedure for calculating the correlation coefficient proposed by Aki in 1957

In the method due to Tomoda, the original stochastic variable is replaced by $+1$ when it is above the mean value, and by -1 when it is below the mean value. Then the computation of the correlation coefficient in the ordinary way is applied to the resultant series of $+1$ and -1. If this value obtained is r, the true correlation coefficient ρ is deduced by the following formula,

$$\rho = \sin \frac{\pi}{2} r .$$

Since the mean value of the deflection of a seimometer pendulum can be assumed as zero, we can write the above r in the form,

$$r = \frac{n_+ - n_-}{n_+ + n_-}$$

where n_+ is the number of sample pairs for which the deflection of one of the seismometers has the same sign as that of the other, while n_- is the number of sample pairs for which their signs are opposite.

This simplified method was applied to seismograms in a correlogram analysis by Aki[1] (1956) which proved its effectiveness.

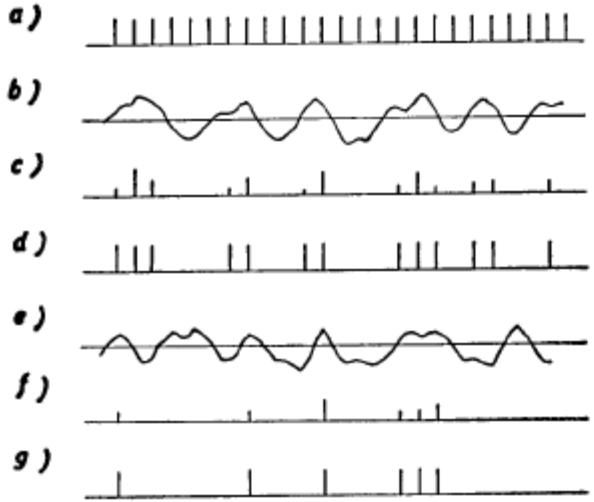

Fig. 4. Process of computation shown schematically,
a) pulses from a pulse generator,
b) signal from the seismometer 1,
c) and *d*) pulses which exist when the signal from *S*1 is positive,
e) signal from the seismometer 2,
f) and *g*) pulses which exist when the signals from both seismometers are both positive.

The one bit normalisation has a long history…

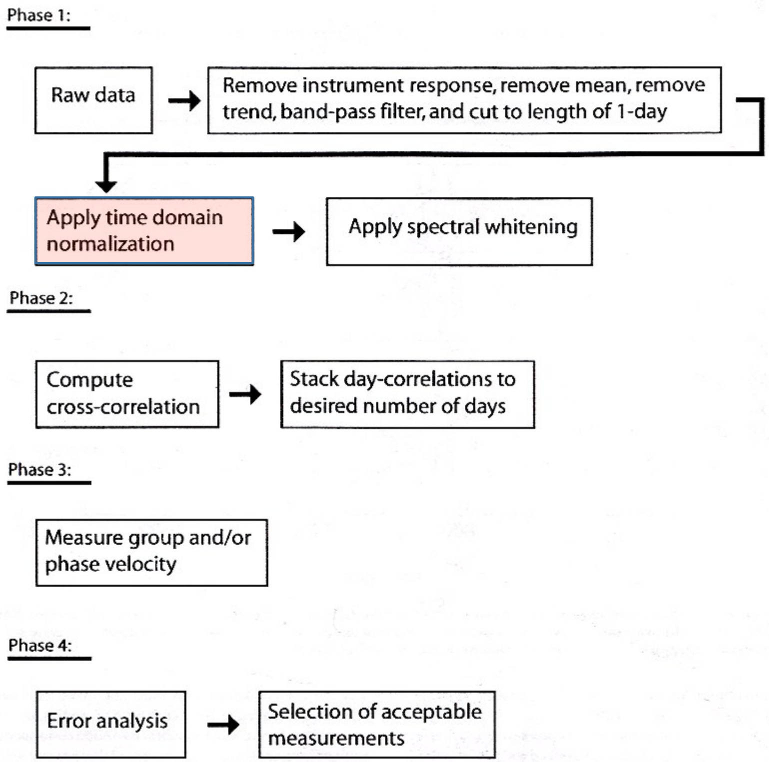

Figure 2. Schematic representation of the data processing scheme. Phase 1 (described in Section 2 of the paper) shows the steps involved in preparing single-station data prior to cross-correlation. Phase 2 (Section 3) outlines the cross-correlation procedure and stacking. Phase 3 (Section 4) includes dispersion measurement and Phase 4 (Section 5) is the error analysis and data selection process.

JOURNAL OF PHYSICS OF THE EARTH, VOL. 4, NO. 2, 1956

TOMODA's Method for Calculating the Correlation Coefficients as Applied to Microtremor Analysis.

By
Kei AKAMATU
Geophysical Institute, Faculty of Science, Tokyo University, Tokyo.

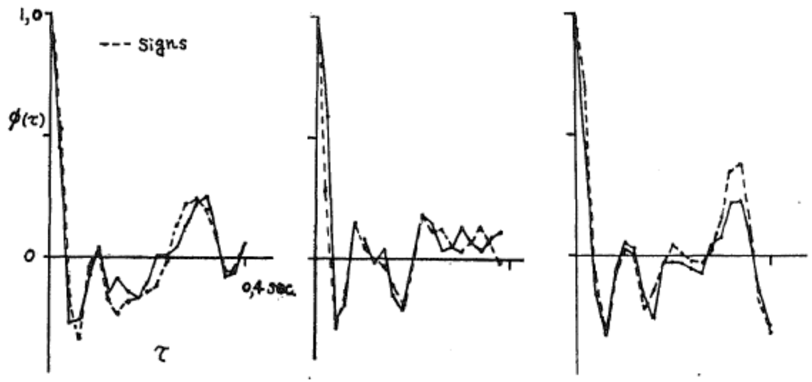

Using seismic noise to estimate the characteristics of a site

Assumption: Seismic noise represents the sum of all waves propagating in a horizontal plane in different directions with different powers but with the same phase velocity for a given frequency.
Waves with different propagation directions and different frequencies are statistically independent.
Plane waves with no attenuation

A spatial correlation function can therefore be defined as

$$\phi(r,\lambda) =< u(x,y,t)(x + r\cos(\lambda), y + r\sin(\lambda), t) > \quad (1)$$

u(*x*, *y* ,*t*) is the velocity observed at point (*x*,*y*) at time *t*
r is the inter-station distance
λ *i*s the azimuth
< > denotes the ensemble average

Using seismic noise to estimate the characteristics of a site

Aki (1957):

We shall now proceed to the case of dispersive waves, and show that Eq. (15) obtained above holds also in this case without any modification except the substitution of the function $c(\omega)$ of frequency ω for the constant velocity c. For this, we notice that if we take $\Delta\rho_n$ as constant for all n, the interval $\Delta\omega_n$ between consecutive ω_n is no longer constant in the dispersive case and varies with n. Then we may write

$$\Delta\omega_n = \left(\frac{d\omega}{d\rho}\right)_n \Delta\rho_n . \tag{16}$$

The equation corresponding to Eq. (14) is now written as

$$\Phi(\omega) = \frac{|G(\omega/c)|^2}{d\omega/d\rho} . \tag{17}$$

Introducing of this into Eq. (10) yields the final formula,

$$\begin{aligned}\phi(\xi) &= \frac{1}{2\pi}\int_{-\infty}^{\infty} |G(\omega/c)|^2 \exp\left(\frac{i\omega}{c(\omega)}\xi\right)\frac{d\rho}{d\omega}\, d\omega \\ &= \frac{1}{\pi}\int_0^{\infty} \Phi(\omega)\cos\left(\frac{\omega}{c(\omega)}\xi\right)d\omega \qquad (18)\end{aligned}$$

Using seismic noise to estimate the characteristics of a site

An azimutal average of this function is given by

$$\phi(r) = \frac{1}{\pi}\int_0^{\pi} \phi(r,\lambda)\,d\lambda \qquad (2)$$

The autocorrelation function is related to the power spectrum $\phi(\omega)$ by

$$\phi(r) = \frac{1}{\pi}\int_0^{\infty} \phi(\omega)\,J_0\left(\frac{\omega r}{c(\omega)}\right)d\omega \qquad (3)$$

J_0 $(\omega r/c(\omega))$ is the zeroth order Bessel function
$c(\omega)$is the frequency-dependent phase velocity

Using seismic noise to estimate the characteristics of a site

The space-correlation function for one angular frequency ω_0, normalized to the power spectrum, will be of the form

$$\phi(r, \omega_o) = J_0\left(\frac{\omega_0}{c(\omega_0)} r\right) \qquad (4)$$

J_0 is the zero order Bessel function.
$c(\omega)$ is the frequency-dependent phase velocity

In this way, the averaged coherencies yield a purely real number; all phase data are lost, and scalar wave velocity is extracted from the amplitude of J0.

Using seismic noise to estimate the characteristics of a site

For every couple of stations (fixed distance r) the function $\phi(\omega)$ can be calculated in the frequency domain by means of (Malagnini et al. 1993; Ohori et al. 2002; Okada 2003):

$$\phi(\omega) = \frac{\frac{1}{M}\sum_{m=1}^{M} \mathrm{Re}\left({}_m S_{jn}(\omega)\right)}{\sqrt{\frac{1}{M}\sum_{m=1}^{M} {}_m S_{jj}(\omega) \sum_{m=1}^{M} {}_m S_{nn}(\omega)}} \qquad (5)$$

${}_mS_{jn}$ is the cross-spectrum for the *m*-th segment of data between the *j*-th and the *n*-th station
M is the total number of used segments.
The power spectra of the *m*-th segment at station *j* and station *n* are ${}_mS_{jj}$ and ${}_mS_{nn}$, respectively.

Using seismic noise to estimate the characteristics of a site

Spatial correlation values $\phi(\omega)$ are plotted as function of distance. A grid search procedure is applied to find the $c(\omega)$ that gives the best fit to the data

$$RMS = \sqrt{\frac{\sum_{n=1}^{N}\left[\overline{\rho}(r_n, f_o) - J_o\left(\frac{2\pi f_o r_n}{c(f_o)}\right)\right]^2}{N}}$$

High frequencies lose coherency at shorter distances

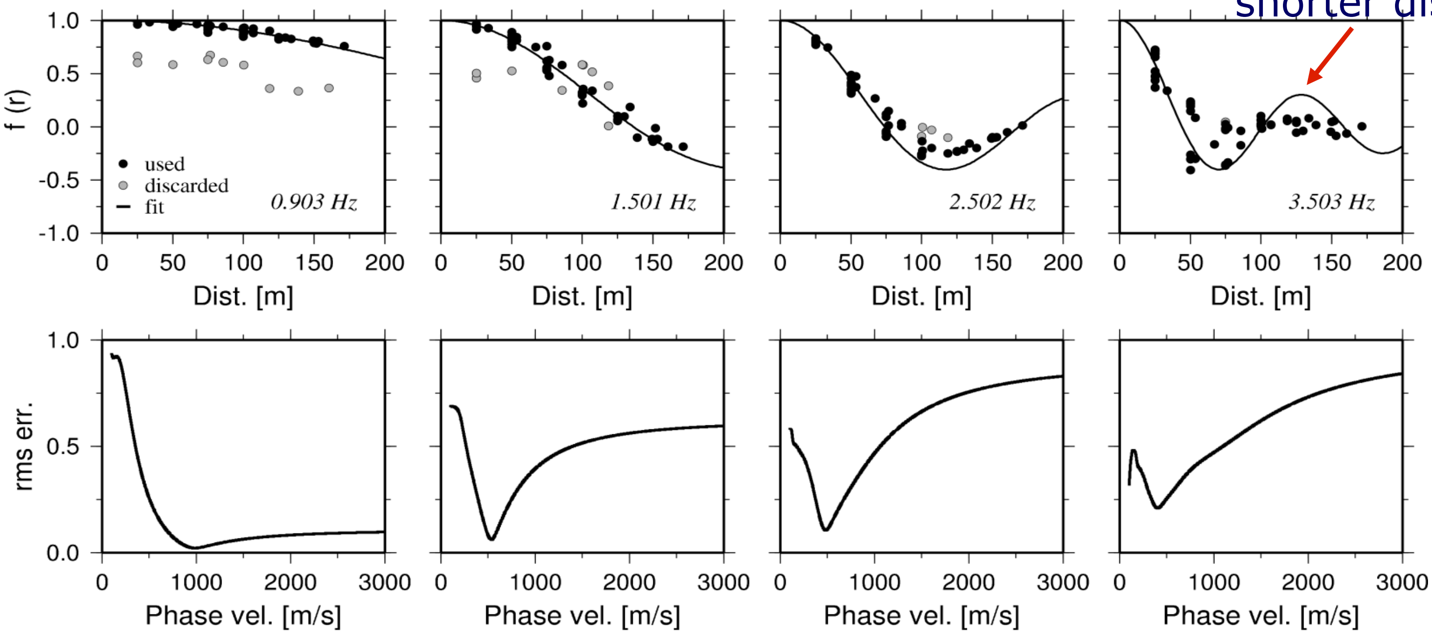

Using seismic noise to estimate the characteristics of a site

$$\phi(r,\omega_o) = J_0\left(\frac{\omega_0}{c(\omega_0)}r\right)$$

The azimuthally averaged coherencies yield a purely real number, meaning that all phase data are lost, and scalar wave velocity is extracted from the amplitude of J0.

The process of modeling SPAC can also be expressed as a summation of complex coherencies each having amplitude unity,with phase given by

$$c_{jc}(f) = \exp\{ir_{jc}k\cos(\theta_{jc} - \phi)\}$$

where $c_{jc}(f)$ is a coherency measured by a single pair of geophones.
r_{jc} is the displacement of the j-th geophone relative to the center at azimuthal angle *jc*
k is the spatial wavenumber at frequency f

Using seismic noise to estimate the characteristics of a site

(3) In the case of a two dimensional wave having a single velocity and being not polarized, a one to one correspondence is found between the azimuthally averaged spatial autocorrelation function

$$\overline{\phi}(r)=\frac{1}{2\pi}\int_0^{2\pi}\phi(r,\ \psi)d\psi$$

and the spectrum density $\Phi(\omega)$ in time as follows,

$$\Phi(\omega)=\frac{\pi\omega}{c^2}\int_0^\infty\overline{\phi}(r)J_0\left(\frac{\omega}{c}r\right)rdr\ , \tag{38}$$

$$\overline{\phi}(r)=\frac{1}{\pi}\int_0^\infty\Phi(\omega)J_0\left(\frac{\omega}{c}r\right)d\omega\ . \tag{39}$$

Using seismic noise to estimate the characteristics of a site

$$c_{jc}(f) = \exp\{i r_{jc} k \cos(\theta_{jc} - \phi)\}$$

$$c(f) = c_r(f) + c_i(f) = \left(\frac{1}{nm}\right) \sum_{j}^{n} \sum_{i}^{m} \exp\{i r_{jc} k \ \cos(\theta_{jc} - \phi_i)\}$$

Imaginary component of SPAC as quality control

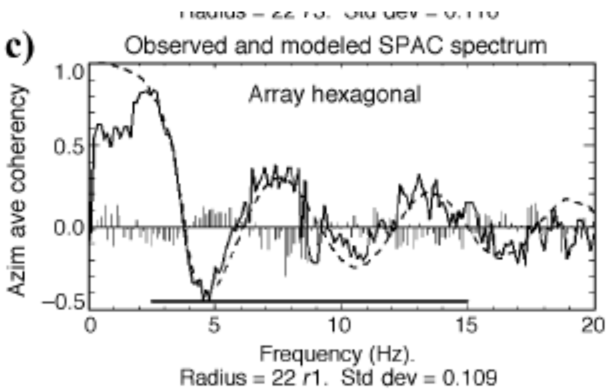

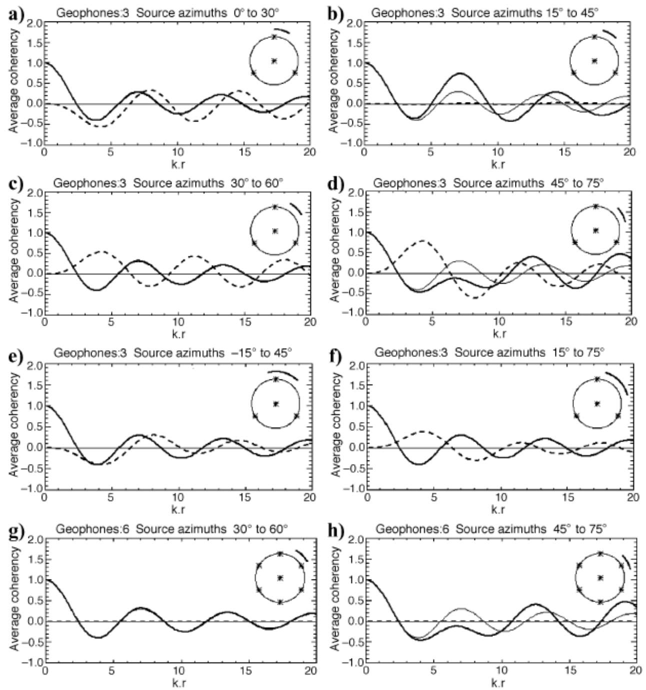

Figure 2. (a–d) Modeled SPAC for a triangular array, $n = 3$, $\Delta = 30°$, for four different dominant directions of wave propagation. The solid line is the real part of the SPAC spectrum $c_r(f)$, the dashed line is the imaginary part $c_i(f)$, and the thin solid line is theoretical

Using seismic noise to estimate the characteristics of a site

Aki states "calculating the spatially averaged correlation function … for a certain interstation distance"

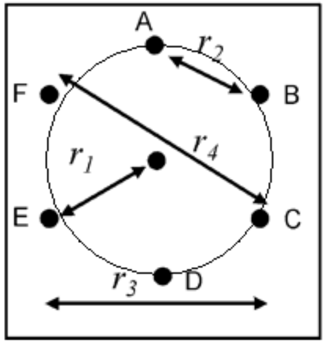

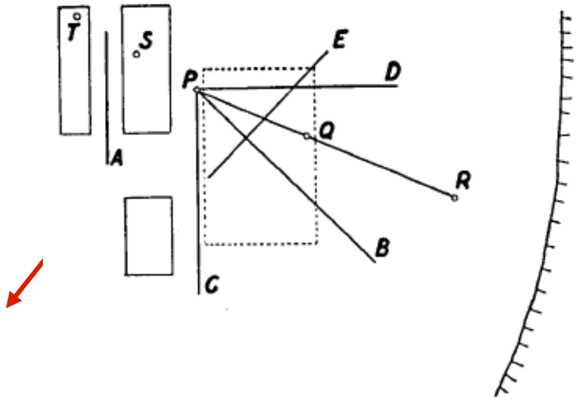

Fig. 9. Map showing lines of measurement.

Common misinterpretation: fixed interstation distance, i.e. circular arrays

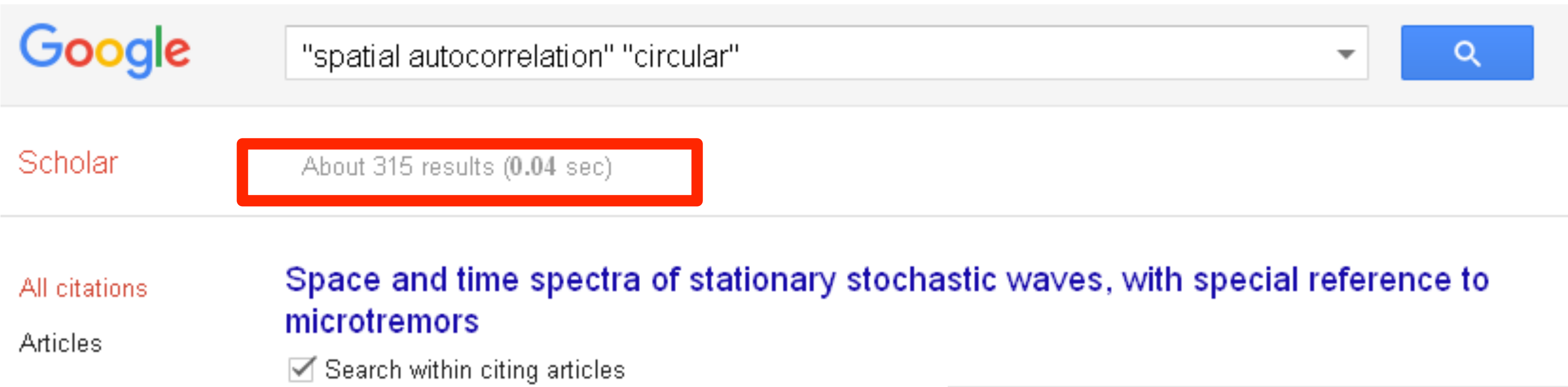

Using seismic noise to estimate the characteristics of a site

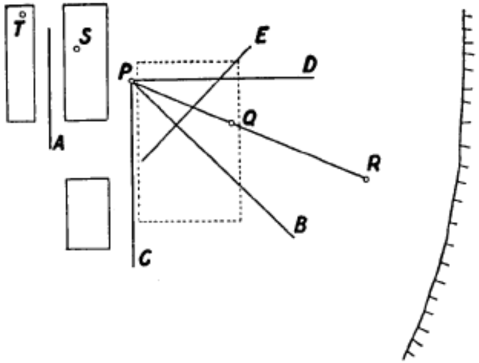

Fig. 9. Map showing lines of measurement.

Fig. 10 shows the autocorrelation coefficients measured along the lines B, C, D, and E in Fig. 9. In this measurement, horizontal seismometers having the frequency of 10 c/s are used and filtration is not applied. Since the curves in the figure differ only slightly from one another, we may regard the micro-tremor as being propagated in every direction, each with almost uniform power. Thus it may be allowed to replace the azimuthally averaged autocorrelation function by the autocorrelation function taken along any line having an arbitrary azimuthal angle. (See Section 8, Chapter 1.)

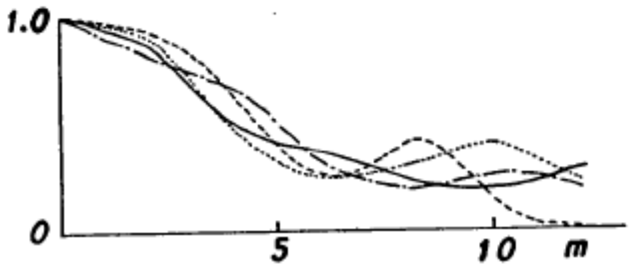

Fig. 10. Autocorrelation coefficients for various directions.

Using seismic noise to estimate the characteristics of a site

Aki (1965)

Toksöz (1964) → He also concluded that there was no way of improving the results by the use of special arrays because, according to him, there were two unknown parameters, direction and phase velocity, and without the knowledge of one the other cannot be found. I thought this problem was already solved in my paper (Aki, 1957), in which a statistical theory of determining the phase velocity of random waves was given with a successful application to microseisms in Tokyo in the frequency range of 5 to 15 cps. Since Toksöz's conclusion might have given a pessimistic view on the use of microseisms, I feel it is necessary to report a brief summary of my old paper published in a Japanese journal which might not be well circulated in the United States.

Using seismic noise to estimate the characteristics of a site

Observed and calculated spatial correlation values $\phi(\omega)$ for all the considered frequencies

From observed data   From grid search best fit

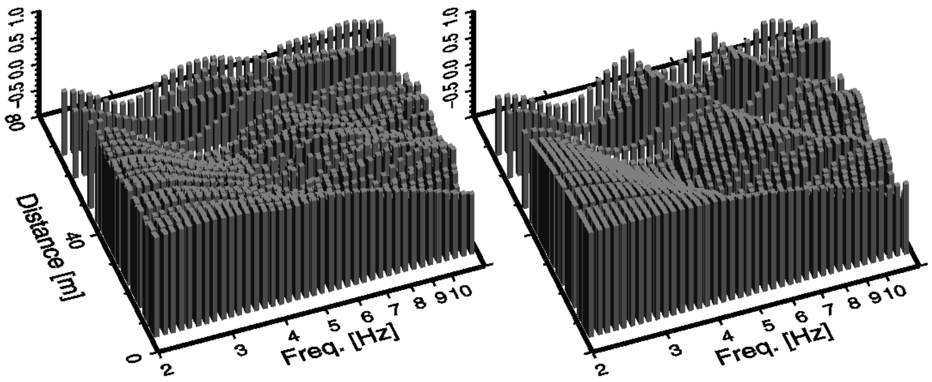

Using seismic noise to estimate the characteristics of a site

The $c(\omega)$ values plotted versus the frequency provide the dispersion curve. Since the phase velocity is related to the S-wave velocity structure of the site, the dispersion curve can be inverted to obtain a 1D model of the velocity structure.

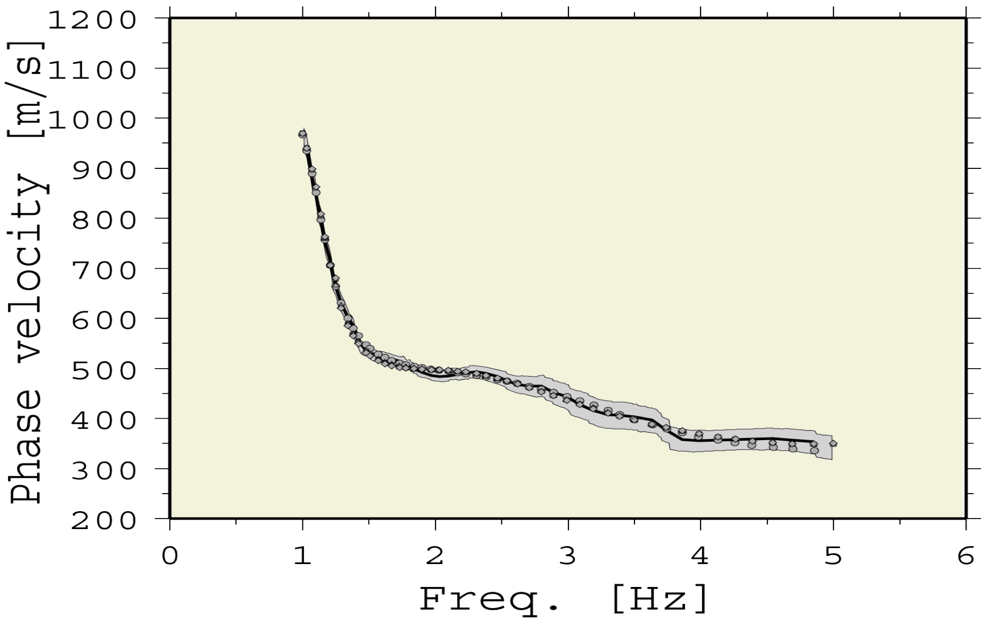

Using seismic noise to estimate the characteristics of a site

As discussed by Aki, the SPAC equations dervied for the analysis of the vertical component of ground motion can, in principle, be adapted also for the analysis of the horizontal components, with the aim of extracting the phase velocities of both Rayleigh and Love waves.

Similar equations to $\bar{\rho}(r,\omega_0) = J_o\left(\frac{\omega_0}{c(\omega_0)}r\right)$ can be derived for the radial and tangential components.

In the study of horizontal motion, we may set the direction of seismograph displacement parallel to the direction connecting the seismograph pair or perpendicular to it. In the former case, the space-correlation function between the pair will take the form

$$J_o\left(\frac{\omega}{c(\omega)}r\right) - J_2\left(\frac{\omega}{c(\omega)}r\right) \longleftarrow \text{tangential}$$

for the waves polarized in the direction of propagation like Rayleigh waves, and the form

$$J_o\left(\frac{\omega}{c(\omega)}r\right) + J_2\left(\frac{\omega}{c(\omega)}r\right) \longleftarrow \text{radial}$$

for the waves polarized perpendicularly to the direction of propagation like Love waves.

Using seismic noise to estimate the characteristics of a site

In the general case of a superposition of Rayleigh and Love waves, under the assumption that the contributions of both waves are statistically independent, the correlation coefficients are given by

$$\overline{\rho_r}(r,\omega) = \alpha\left[J_0(x) - J_2(x)\right] + (1-\alpha)\left[J_0(x') + J_2(x')\right]$$

$$\overline{\rho_t}(r,\omega) = \alpha\left[J_0(x) + J_2(x)\right] + (1-\alpha)\left[J_0(x') - J_2(x')\right],$$

JOURNAL OF GEOPHYSICAL RESEARCH, VOL. 102, NO. B10, PAGES 22,529–22,545, OCTOBER 10, 1997

Permanent tremor of Masaya Volcano, Nicaragua: Wave field analysis and source location

Jean-Philippe Métaxian[1,2] and Philippe Lesage[1]
Laboratoire d'Instrumentation Géophysique, Université de Savoie, Le Bourget-du-Lac, France

Jacques Dorel[1]
Observatoire de Physique du Globe de Clermont-Ferrand (OPGC), Clermont-Ferrand, France

α represents the proportion of Rayleigh waves in the wave field energy ($0 < \alpha < 1$).

Using seismic noise to estimate the characteristics of a site

α represents the proportion of Rayleigh waves in the wave field energy ($0 < \alpha < 1$).

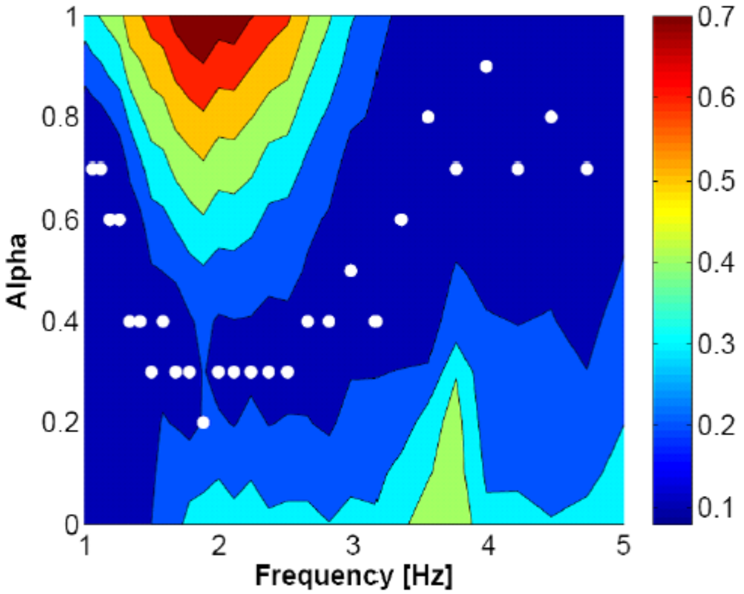

Figure 3: Distribution of α values (white dots) for different frequencies and the associated RMS error.

ELSEVIER
Journal of Applied Geophysics
Volume 75, Issue 2, October 2011, Pages 345–354

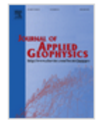

Shallow geology characterization using Rayleigh and Love wave dispersion curves derived from seismic noise array measurements

T. Boxberger, M. Picozzi, S. Parolai

Using seismic noise to estimate the characteristics of a site

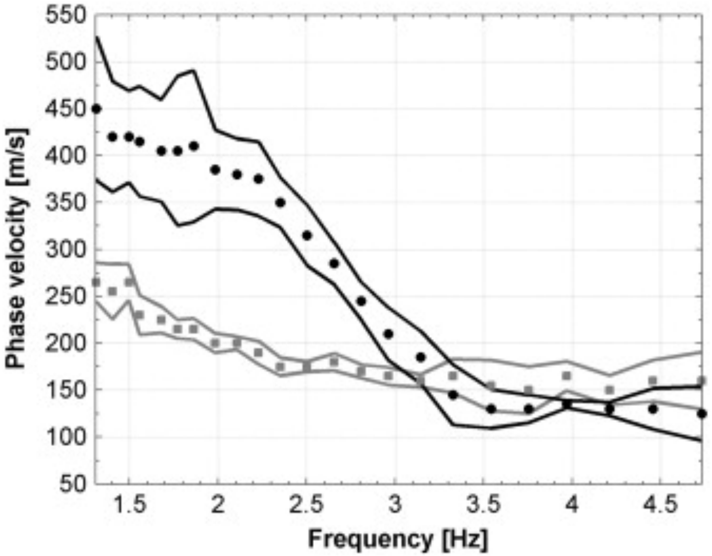

Fig. 5.
Rayleigh (red) and Love (blue) wave dispersion curves.

ELSEVIER
Journal of Applied Geophysics
Volume 75, Issue 2, October 2011, Pages 345–354

Shallow geology characterization using Rayleigh and Love wave dispersion curves derived from seismic noise array measurements

T. Boxberger, M. Picozzi, S. Parolai

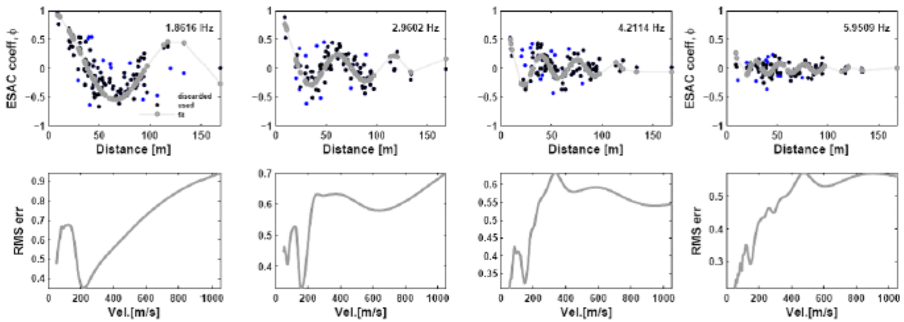

Figure 4: Top row: ESAC function values (black circles) for different frequencies and the horizontal components. The blue circles indicate the discarded values. The grey lines depict the best-fitting Bessel function. Bottom row: RMS error versus phase velocity curves.

Using seismic noise to estimate the characteristics of a site

The dispersion curves of the fundamental and higher mode Rayleigh waves mainly depend **non-linearly** on the S-wave velocity structure, but also the density and P-wave velocity structure.

The inversion can be carry out linearizing the problem, that is calculating the Jacobian matrix that links the model parameters to the phase velocity.

$$C=JDV$$

Where C= vector whose i elements are the $c_{obsi}(w)-c_{calci}(w)$

J=matrix with i rows and j (number of unknown, e.g. S-wave velocity in each layer) whose elements are d $c_{calci}(w)/ dVs_j$
DV is an array whose j elements are the correction values of the starting j layer velocities

The inverse problem can be solved using Singular Value Decomposition (SDV, Press et al., 1986) and the RMS of differences between observed and theoretical phase velocities is generally minimized.

Using seismic noise to estimate the characteristics of a site

However the final results strongly depends on the starting model!

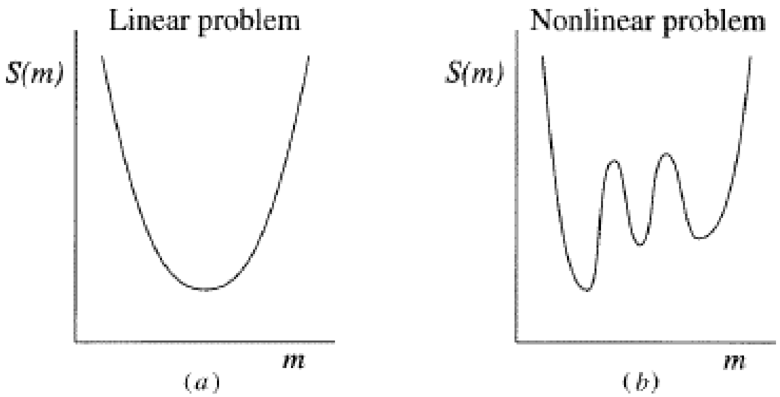

Other methods (genetic algorithm) can be used to solve the non-linear problem.

Inversion of dispersion curves

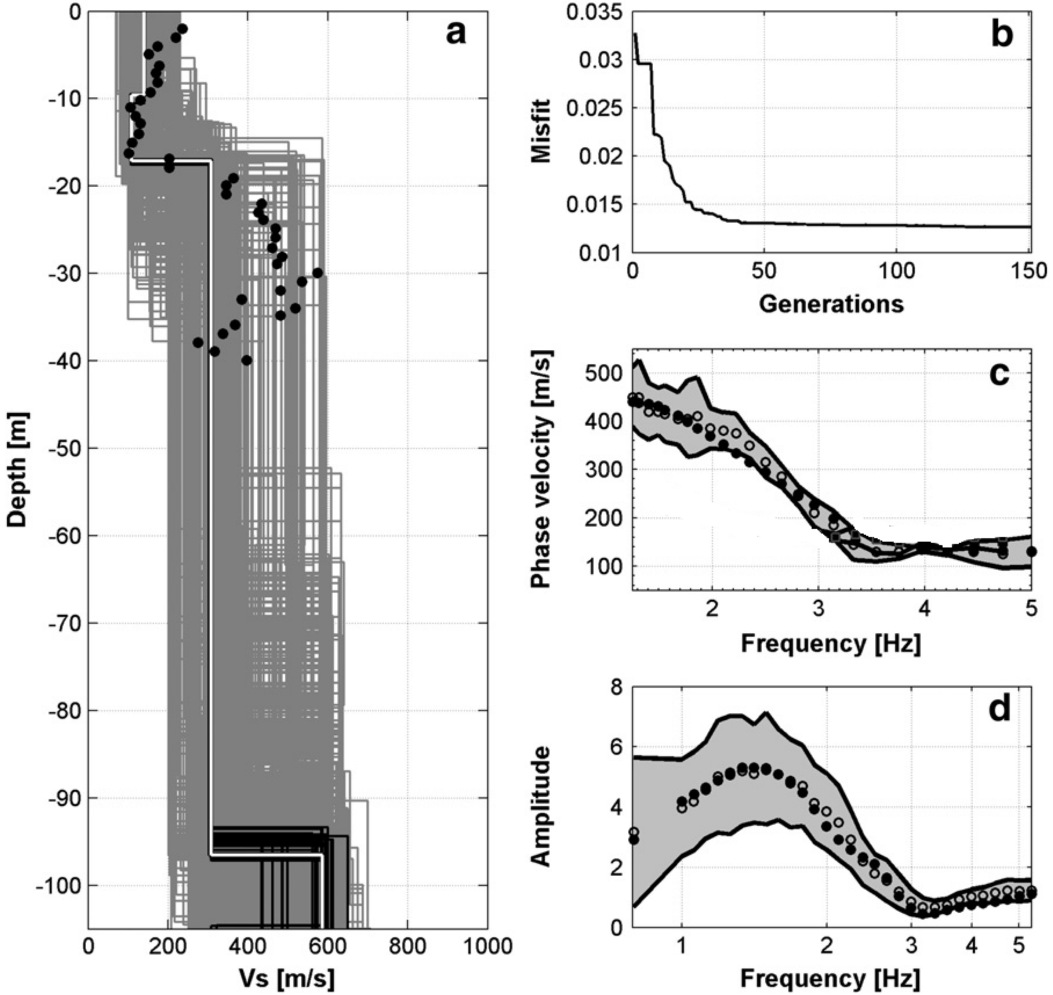

Side note on the calculation of 1D profiles

Bulletin of the Seismological Society of America, Vol. 89, No. 1, pp. 250–259, February 1999

Microtremor Measurements Used to Map Thickness of Soft Sediments

by Malte Ibs-von Seht and Jürgen Wohlenberg

$$f_r = \frac{n \cdot v_s}{4m} \quad (n = 1, 3, 5, \ldots). \tag{1}$$

A velocity-depth function in a sedimentary layer may be written as

$$v_s(z) = v_0 \cdot (1 + Z)^x, \tag{2}$$

where v_0 is the surface shear-wave velocity, $Z = z/z_0$ (with $z_0 = 1m$), and x gives the depth dependence of the velocity. The fundamental resonant frequency f_r is calculated as $1/4T_0$, where T_0 is the shear-wave travel time between the bottom of the layer and the surface. As by definition, $v(z) = dz/dt$, the travel time is calculated as

$$T_0 = \int_0^m \frac{dz}{v_s(z)} = \frac{1}{v_0} \int_0^m (1 + Z)^{-x}\, dz = \frac{1}{v_0} \frac{(1 + m)^{1-x} - 1}{(1 - x)}. \tag{3}$$

The dependency between thickness and resonant frequency becomes

$$f_r = \frac{1}{4T_0} = \frac{v_0(1 - x)}{4[(1 + m)^{1-x} - 1]} \tag{4}$$

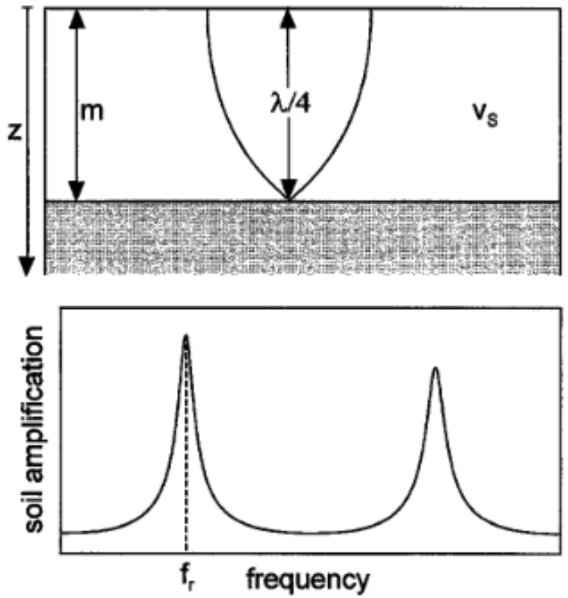

Figure 1. Basic principle of site response, transfer function.

GFZ
Helmholtz Centre
POTSDAM

www.seismo.ethz.ch

Side note on the calculation of 1D profiles

Bulletin of the Seismological Society of America, Vol. 92, No. 6, pp. 2521–2527, August 2002

Short Note

New Relationships between V_s, Thickness of Sediments, and Resonance Frequency Calculated by the H/V Ratio of Seismic Noise for the Cologne Area (Germany)

by S. Parolai, P. Bormann, and C. Milkereit

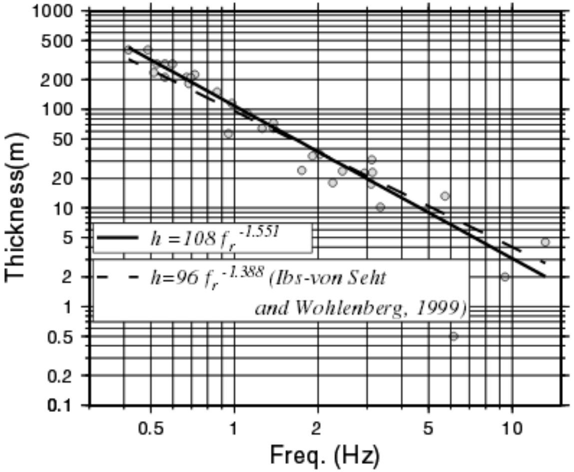

Figure 3. Fundamental resonant frequencies calculated from H/V spectral ratio vs. sediment thickness from borehole data. The solid line is the fit to the data points according to Equation (2). The dashed line is relation (3).

Velocity–Depth Function

A velocity–depth function in a sedimentary layer may be written as

$$v_s(z) = v_{so}\,(1 + Z)^x, \tag{4}$$

$$h = \left[v_{so}\,\frac{(1 - x)}{4f_r} + 1 \right]^{1/(1-x)} - 1, \tag{6}$$

where f_r is to be given in Hz, v_{so} in m/sec, and h (soft sedimentary layer thickness) in m (Ibs-von Seht and Wohlenberg, 1999).

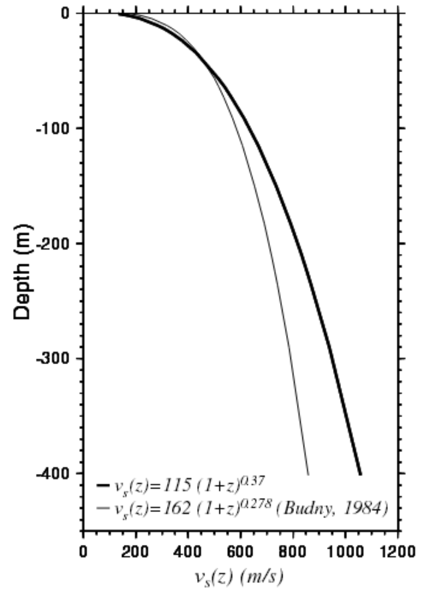

Side note on the calculation of 1D profiles

Caution: The basic formulas are given in an integral form!

$$T_0 = \int_0^m \frac{dz}{v_s(z)} = \frac{1}{v_0}\int_0^m (1 + Z)^{-x}\, dz = \frac{1}{v_0}\,\frac{(1 + m)^{1-x} - 1}{(1 - x)}.$$

from Ibs-von Seht and Wohlenberg (1999)

Approximate formula of peak frequency of H/V ratio curve in multilayered model and its use in H/V ratio technique

Tran Thanh Tuan[1] *, Pham Chi Vinh[1], P. Malischewsky[2], Abdelkrim Aoudia[3]
[1] *Hanoi University of Science, VNU, Vietnam*
[2] *Friedrich-Schiller University Jena, Germany*
[3] *Abdus Salam International Centre for Theoretical Physics, Earth System Physics Section, Trieste, Italy*

March 17, 2015

Analogous to the FGM layer, the average shear-wave velocity of this composite layer is

$$\bar{V}_s^{\text{composite}} = \frac{2h}{\pi\sqrt{\sum\limits_{i=1}^{N-1}\sum\limits_{j=i+1}^{N}\frac{\rho_i}{\rho_j\beta_j^2}h_i h_j + \frac{1}{2}\sum\limits_{i=1}^{N}\frac{h_i^2}{\beta_i^2}}}. \qquad (35)$$

This formula is called the H/V-based average velocity formula.

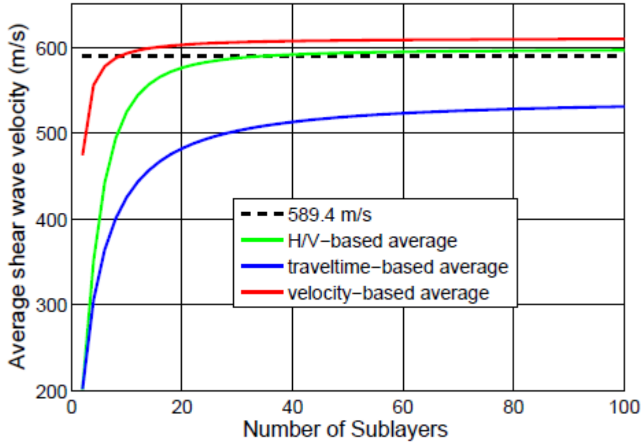

Figure 2: Average shear-wave velocities vs. number of sublayers

This approach takes for one layer only the velocity at the surface!

Inversion of dispersion curves

You have to consider that you are inverting an apparent dispersion curve (not just the fundamental mode).

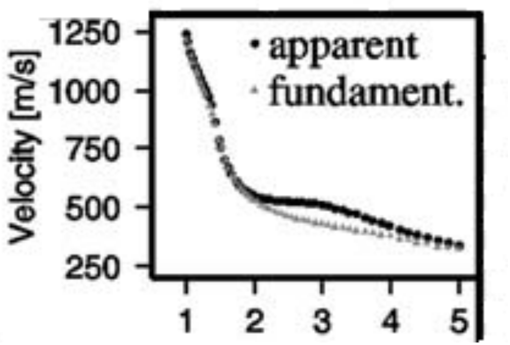

GEOPHYSICAL RESEARCH LETTERS, VOL. 32, L01303, doi:10.1029/2004GL021115, 2005

Joint inversion of phase velocity dispersion and H/V ratio curves from seismic noise recordings using a genetic algorithm, considering higher modes

S. Parolai,[1] M. Picozzi,[2] S. M. Richwalski,[1,3] and C. Milkereit[1]

Fundamental mode assumption is only a good assumption for sites, where the velocity increases with depth.

Dominance of the fundamental and higher modes changes with frequency!

Inversion of dispersion curves

Some of the currently used software packages have limited possibility for including higher modes!

Bulletin of Earthquake Engineering (2006) 4:65–94
DOI 10.1007/s10518-005-5758-2

S-wave Velocity Profiles for Earthquake Engineering Purposes for the Cologne Area (Germany)

S. PAROLAI[1,*], S.M. RICHWALSKI[1,2], C. MILKEREIT[1] and D. FÄH[3]

Is it therefore necessary to include higher modes?

Obviously, the final models deviate more from the input borehole model than the models derived including higher modes (left), especially below 150 m depth, where some significant artifacts are depicted:

Inversion of dispersion curves

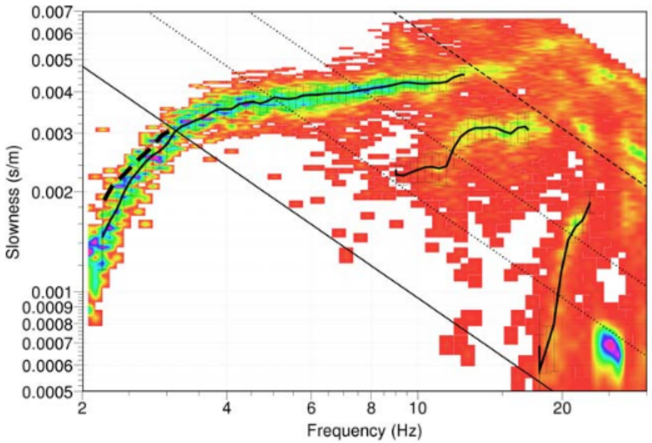

Take care: All programmes will always provide a result.

Check the parameterization!

several tens of layers

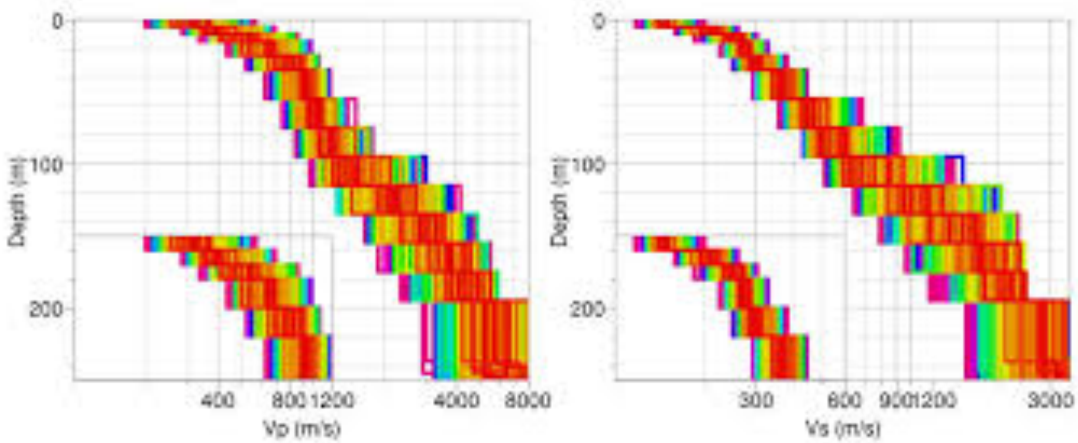

Data resolution matrix

How well can the measured data be predicted?
We have an over-determined system

$$Gm^{true} = d^{obs}$$

with data vectors m and d and data kernel G.

Inversion leads to

$$m^{est} = Hd^{obs}.$$

Equation 2 in equation 1 leads to

$$d^{predict} = Gm^{est} = G(Hd^{obs}) = (GH)d^{obs} = Nd^{obs}$$

with the quadratic data resolution matrix N.

Data resolution matrix

Provides insight into the intrinsic characteristics of the inversion problem.

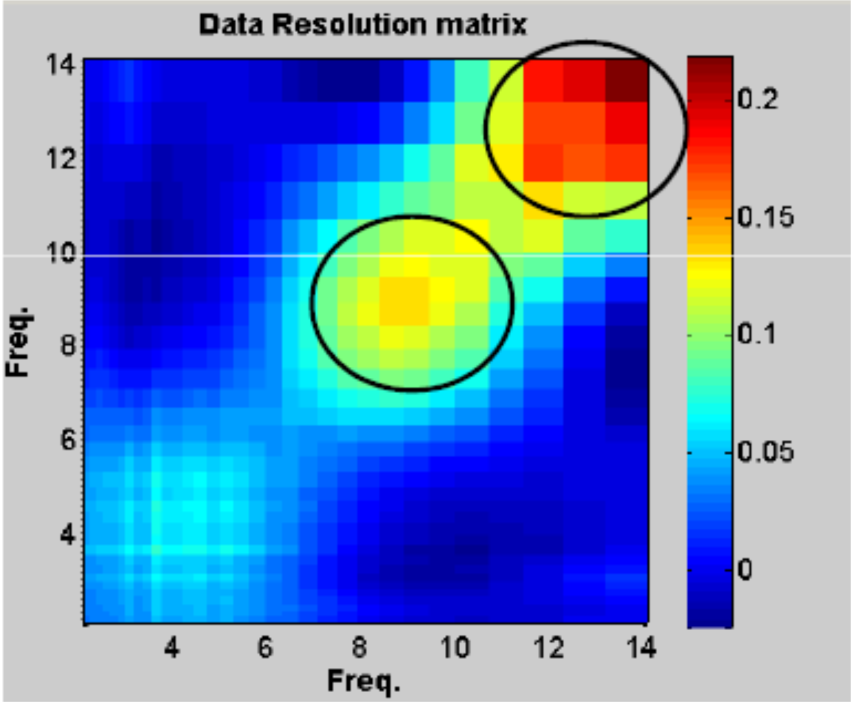

critical for defining the S-wave velocity of the model

Data should be selected based on the data resolution matrix of a good initial model → modifiy investigation depth and/or layer thickness

Model resolution matrix

How well can the parameters be resolved?

Equation 1 in equation 2 leads to

$$m^{est} = HGm^{true} = (G^TG + c\mathbf{1})^{-1} G^TGm^{true} = Rm^{true}$$

with the model resolution matrix R.

inversion to (global) minimum

→ damping factor c → 0

→ R → **1**

→ Model can be perfectly resolved!

Model resolution matrix

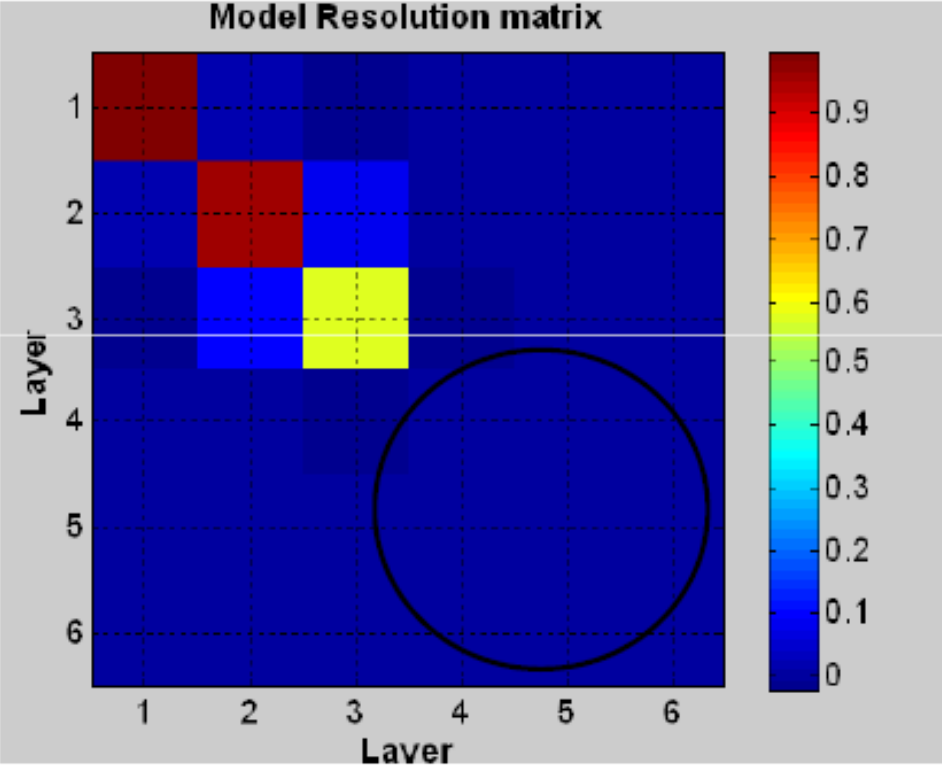

not resolved

Jacobian matrix

Jacobian matrix is the matrix of first order partial derivatives with respect to all model parameters (here: S-wave velocity at different depths).

Maxima within Jacobian matrix indicates for which change in velocity at depth each frequency is more sensitive.

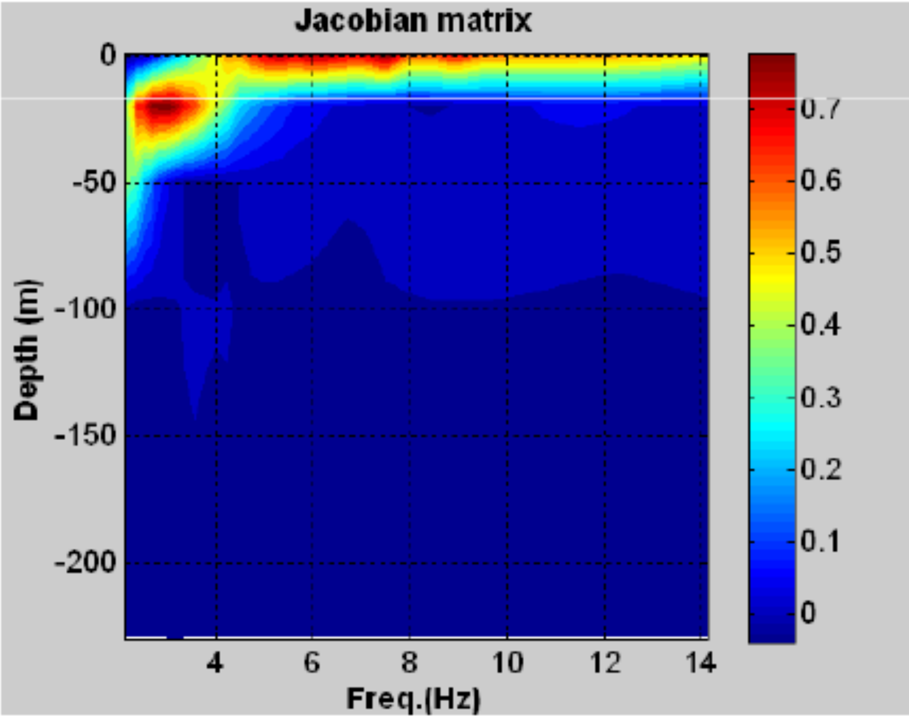

Lateral heterogeneities

Already in 1953, Haskell presented phase velocity dispersion equations, concluding that the scatter in the data might represent "real horizontal heterogeneities of the crust".

THE DISPERSION OF SURFACE WAVES ON MULTILAYERED MEDIA*

By N. A. HASKELL

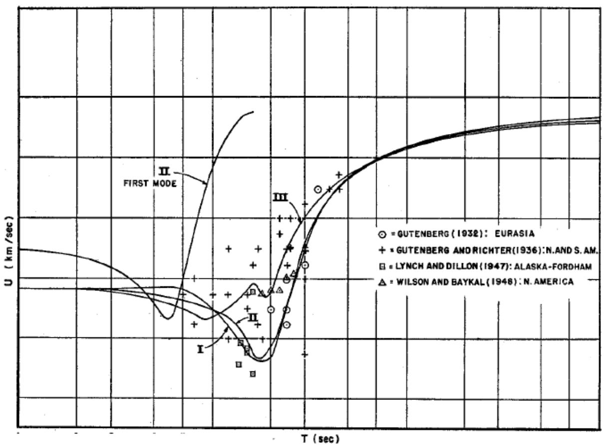

Aki (1957):

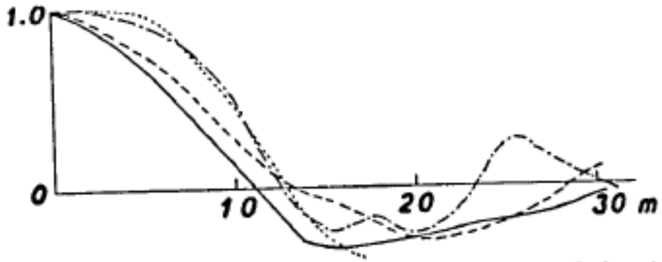

Fig. 21. Autocorrelation coefficients of horizontal motion along the line PQ for

4. Horizontal heterogeneity

It was found, however, that the autocorrelation coefficient taken along a segment of a line sometimes differs significantly from that taken along another segment of the same line.

Seismic interferometry

Claerbout (1968) showed theoretically that the Green's function (i.e., impulse response of a point source) on the Earth's surface could be obtained by autocorrelating traces generated by buried sources.

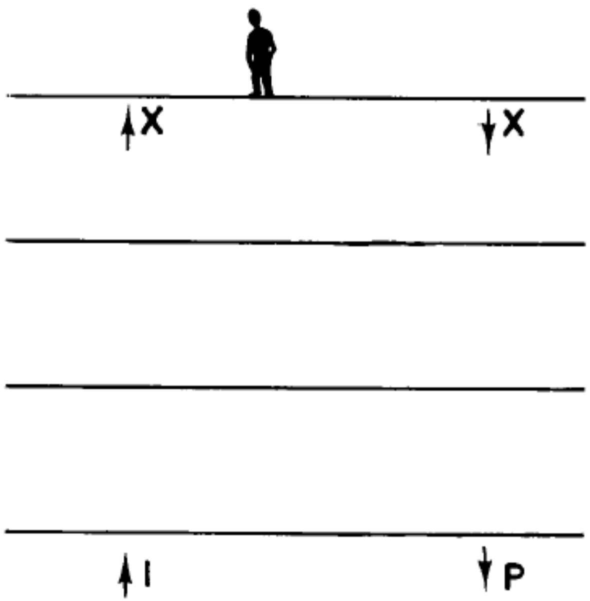

FIG. 3. Incident, observed, and reflected waves in the transmission problem.

GEOPHYSICS, VOL. 33, NO. 2 (APRIL, 1968), P. 264-269, 3 FIGS.

SYNTHESIS OF A LAYERED MEDIUM FROM ITS ACOUSTIC TRANSMISSION RESPONSE

JON F. CLAERBOUT*

Idea of the method

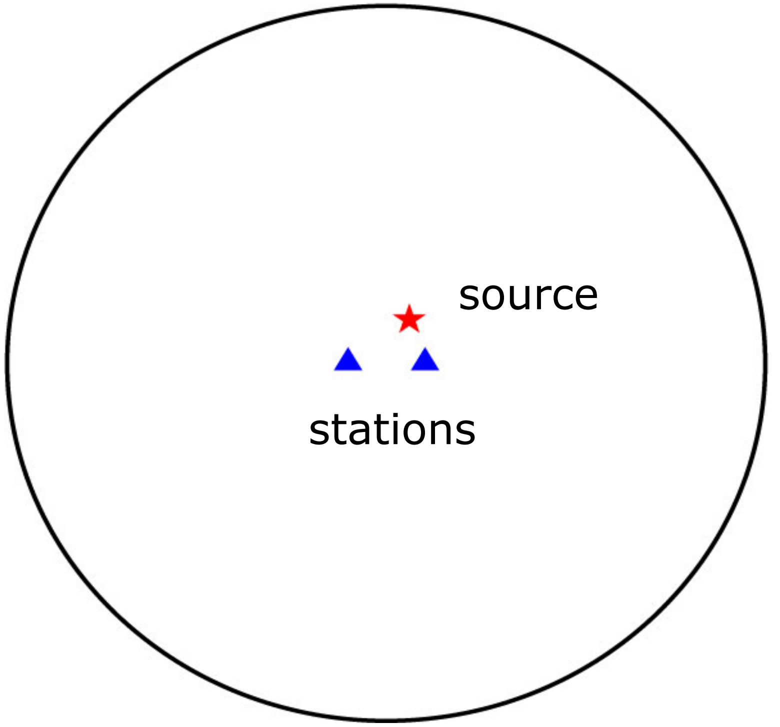

Idea of the method

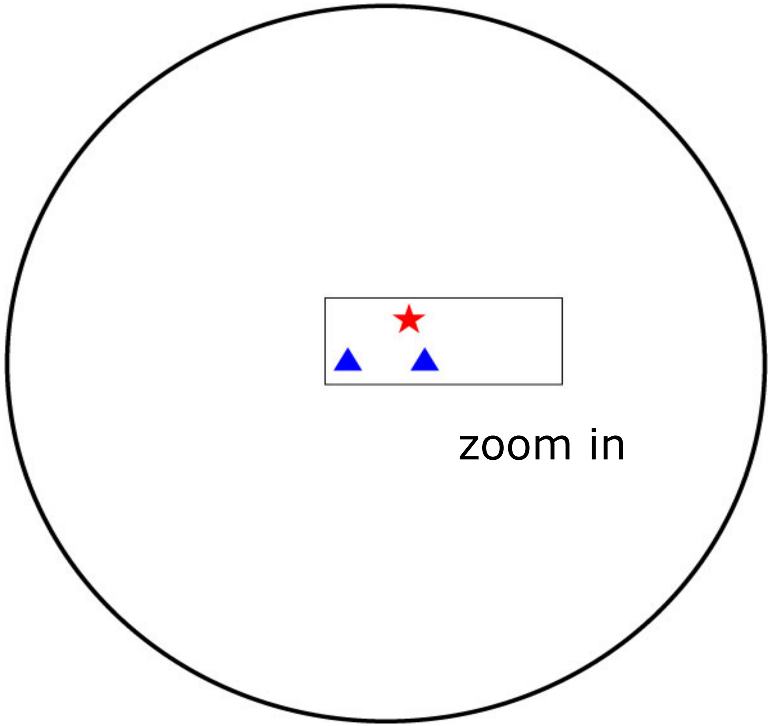

Idea of the method

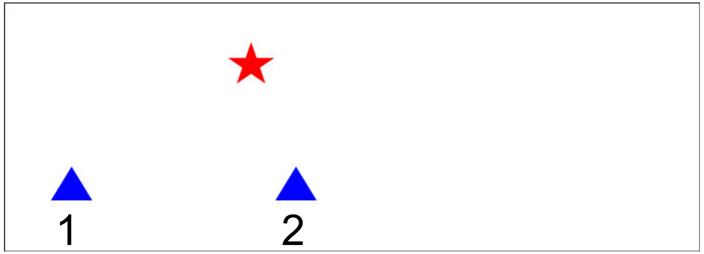

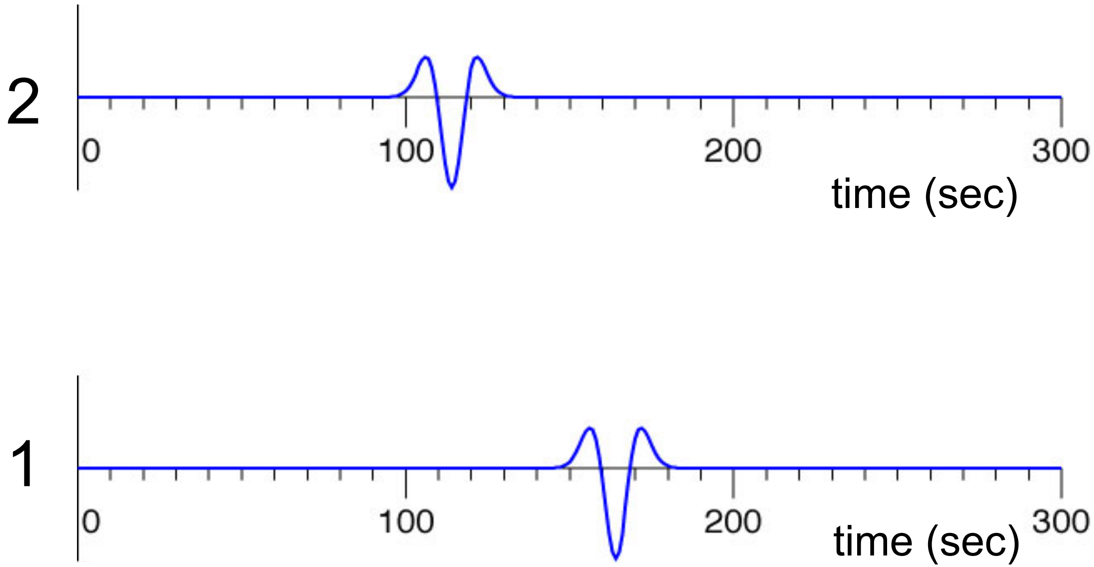

Idea of the method

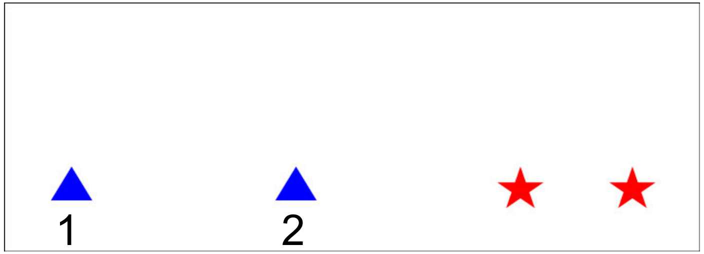

Two sources in line with the stations

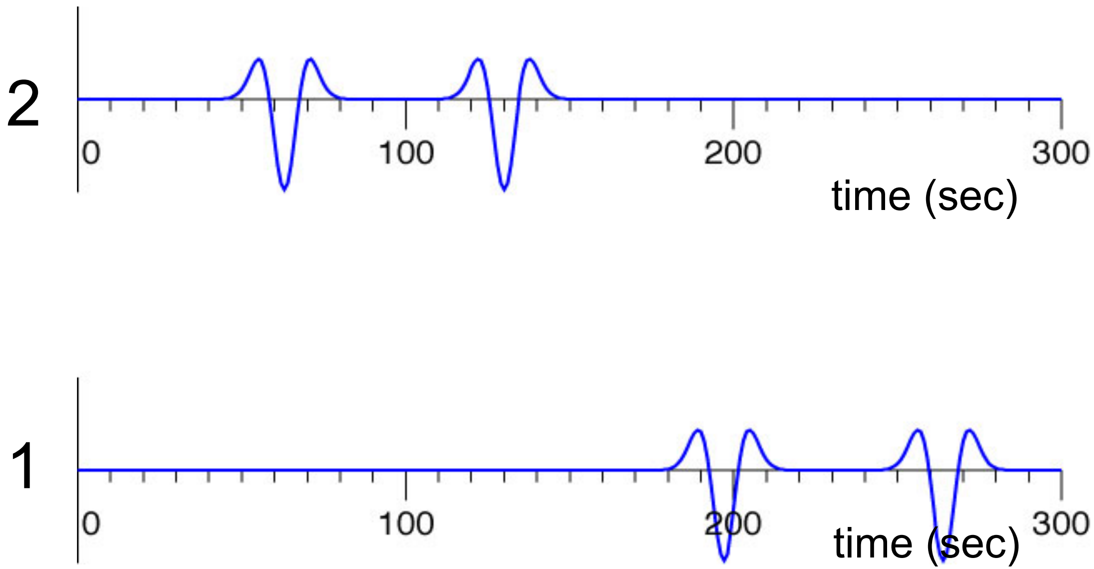

Idea of the method

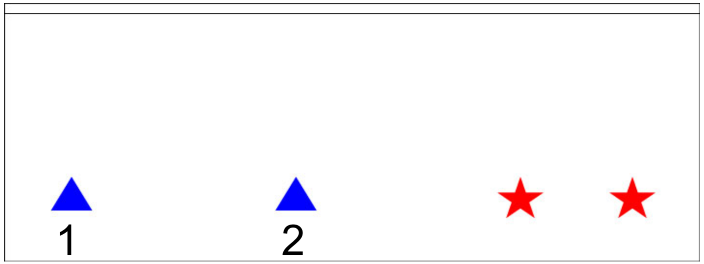

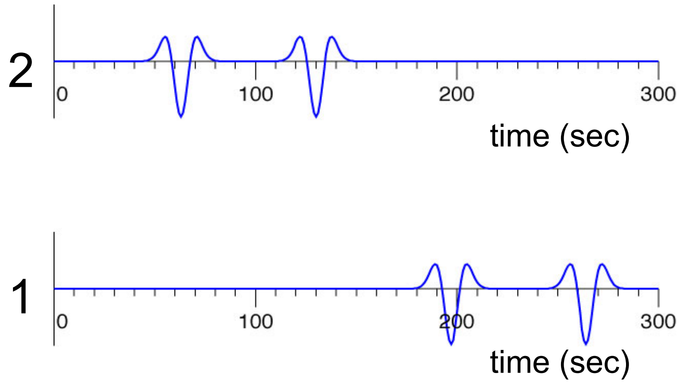

Green function for propagation between the stations.

cross-correlation

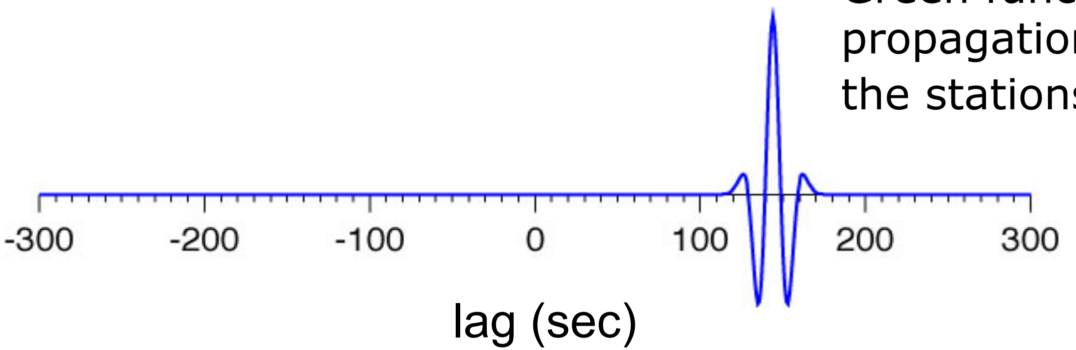

time (sec)

Idea of the method

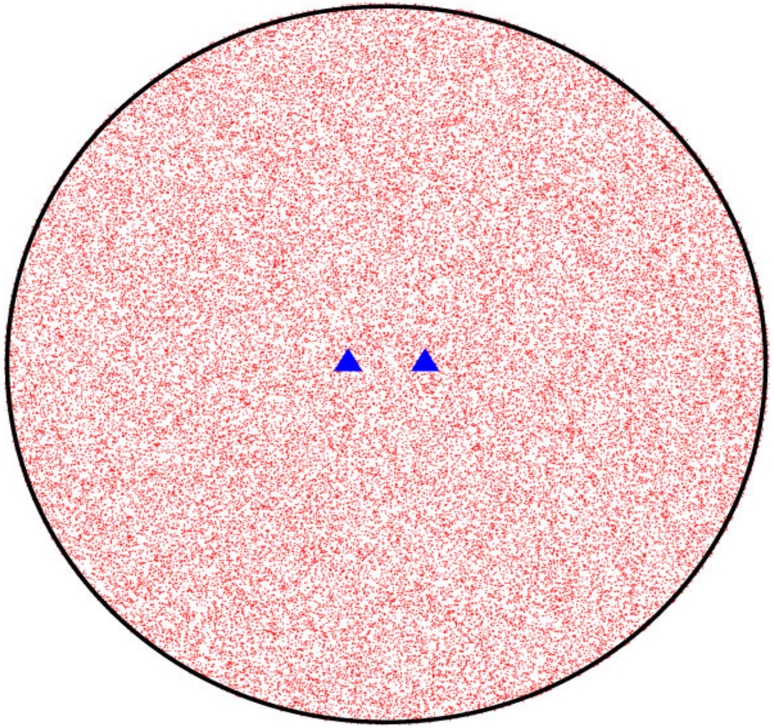

lots of sources

azimuthally homogeneous distribution of sources

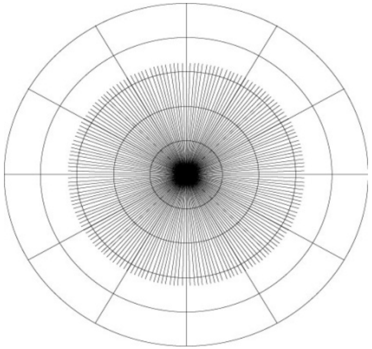

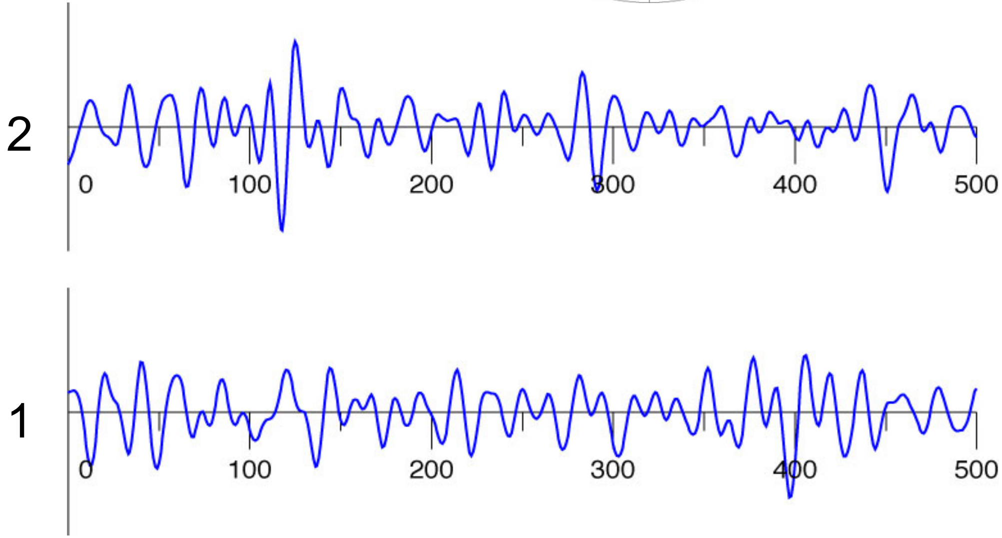

Idea of the method

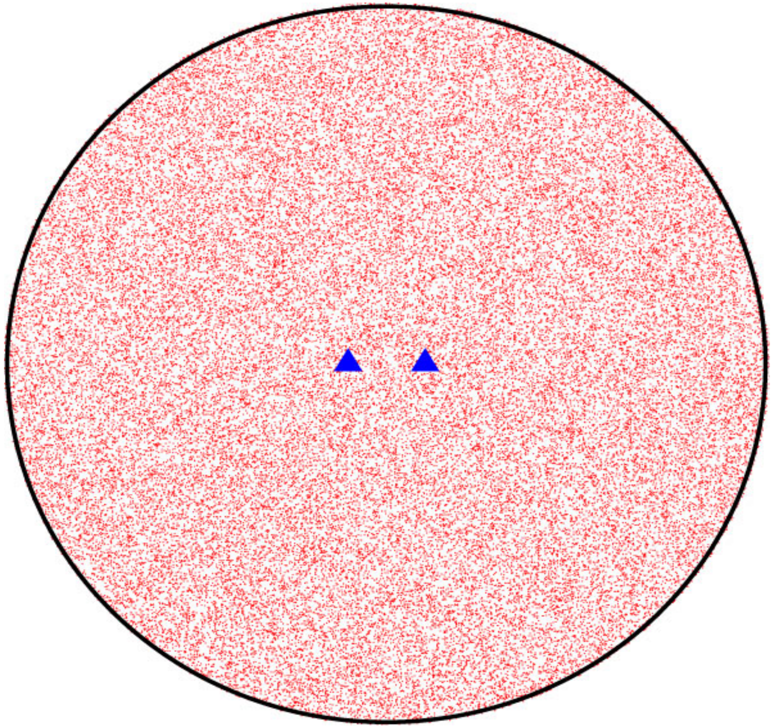

lots of sources

azimuthally homogeneous
distribution of sources

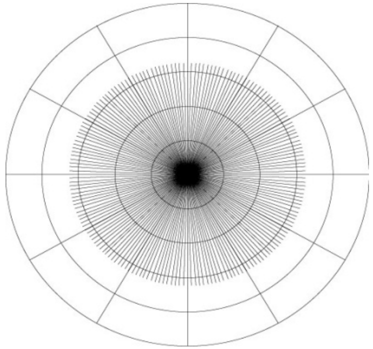

cross-correlation

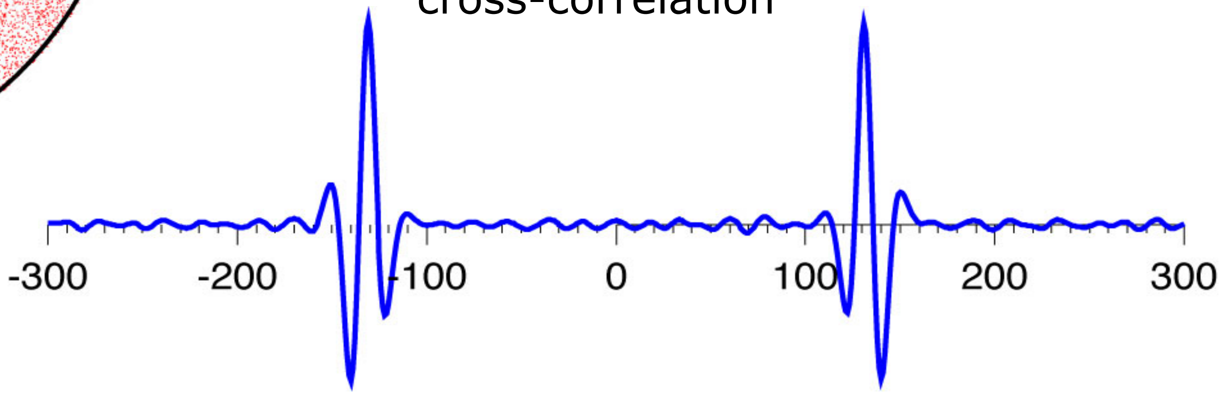

Idea of the method

azimuthally homogeneous
distribution of sources

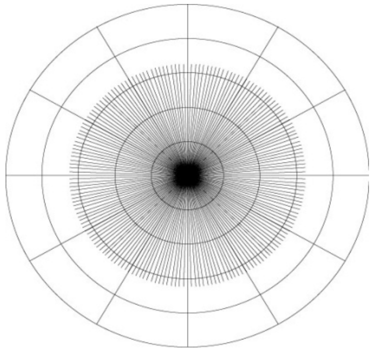

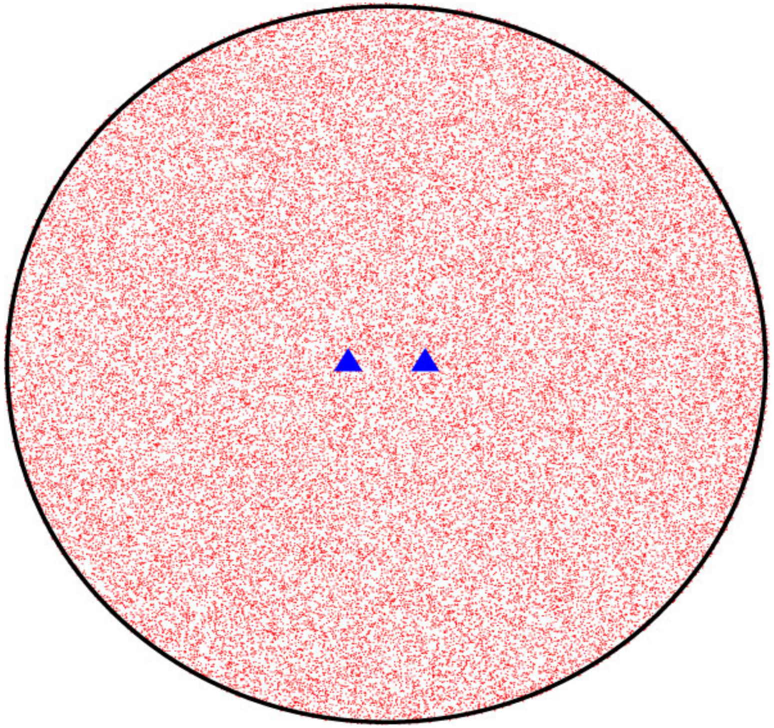

lots of sources

cross-correlation

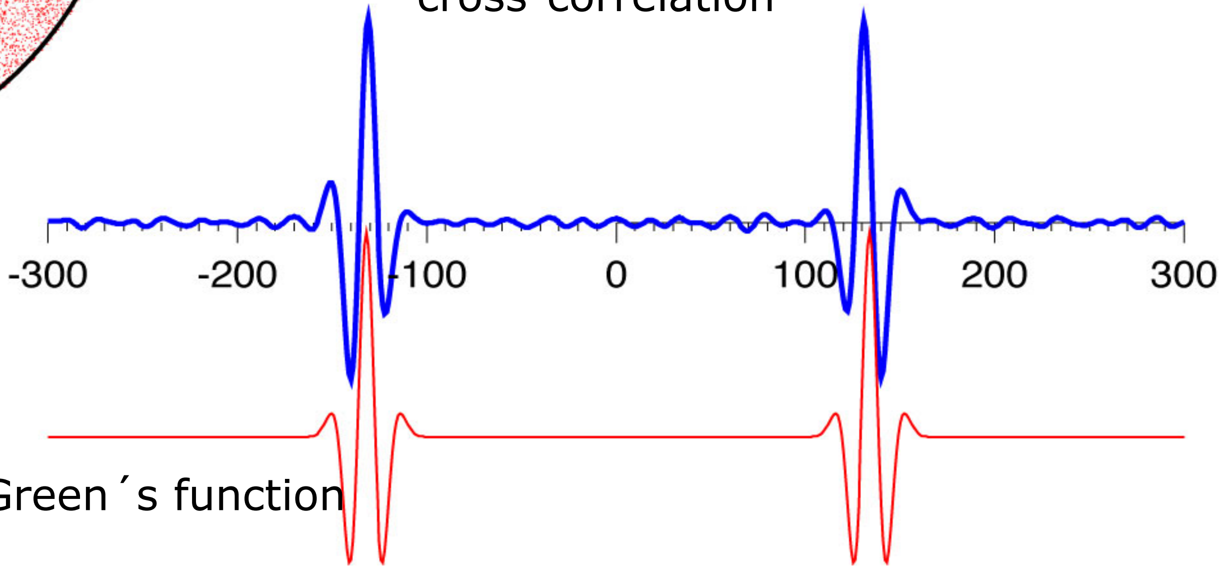

theoretical Green´s function

Seismic interferometry

First works were already published in the 1970s.

VOL. 80, NO. 23 JOURNAL OF GEOPHYSICAL RESEARCH AUGUST 10, 1975

Origin of Coda Waves: Source, Attenuation, and Scattering Effects

KEIITI AKI AND BERNARD CHOUET

Department of Earth and Planetary Sciences, Massachusetts Institute of Technology, Cambridge, Massachusetts 02139

50 *Physics of the Earth and Planetary Interiors*, 21 (1980) 50–60

ATTENUATION OF SHEAR-WAVES IN THE LITHOSPHERE FOR FREQUENCIES FROM 0.05 TO 25 Hz

KEIITI AKI

Department of Earth and Planetary Sciences, Massachusetts Institute of Technology, Cambridge, Massachusetts 02139 (U.S.A.)

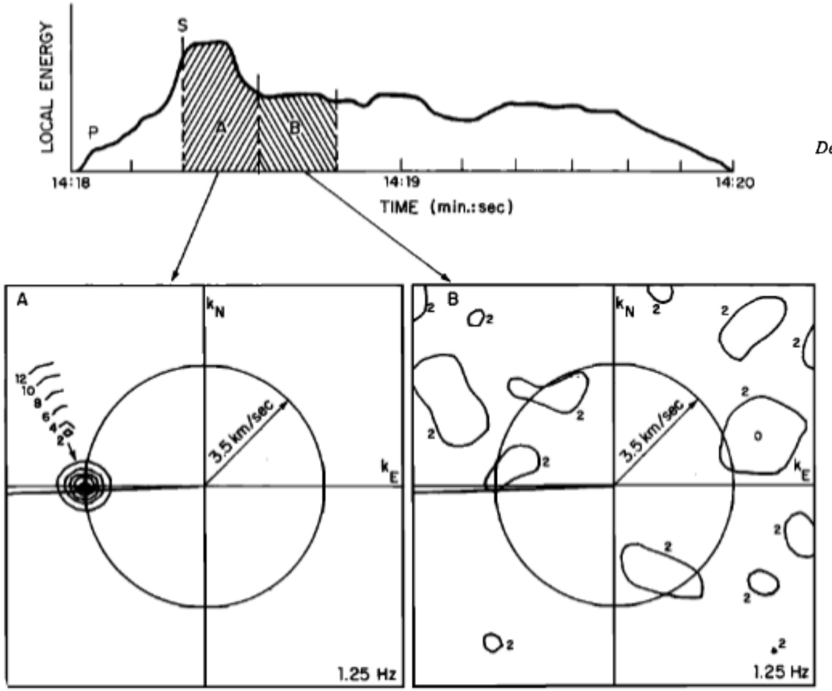

Fig. 2. High-resolution spectra for *S* arrival and *S* coda in frequency band 1.0–2.0 Hz for strip-mining blast near Lasa. This figure is reproduced from *Scheimer and Landers* [1974].

It has been recognized that coda waves, which make up the late part of seismic signals, are the result of scattering from small-scale heterogeneities in the lithosphere

Seismic interferometry

The physics of coda waves cannot be fully understood with classical ray theory. Multiple scattering plays a prominent part in the seismic coda, and seismologists have made use of the radiative transfer theory to model the coda intensity, namely

PAGEOPH, Vol. 128, Nos. 1/2 (1988)   0033-4553/88/020049-32$1.50 + 0.20/0

Multiple Scattering and Energy Transfer of Seismic Waves—Separation of Scattering Effect from Intrinsic Attenuation II. Application of the Theory to Hindu Kush Region

RU-SHAN WU[1] and KEIITI AKI[2]

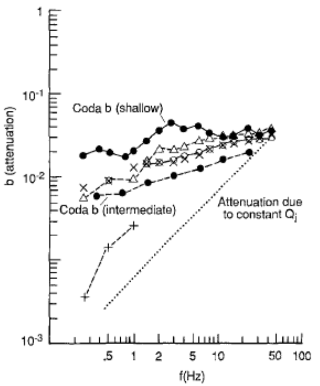

Figure 10

Apparent attenuations derived from the slopes of the energy density for both the total S curves (Figure 7) and the direct S at station PEN, together with the coda attenuations for shallow depth 100 km and for intermediate depth (400 km). Here the depths refer to the approximate maximum sampling depth by the coda waves.

○: for EW component, total S (32 sec window). ×: for Z component, total S (32 sec window). Δ: Z component, direct S (4 sec window). Note: for $f \leq 1$ Hz, the apparent attenuations of total S are calculated by using only the part of the curves for $r > 200$ km.

+: The estimated intrinsic attenuation for $f \leq 1$ Hz, if we adopt the multiple scattering model for $4\pi r^2 E(r)$ curves in Figure 7 (see Table 6). —·— Coda attenuation for shallow sampling depth (<100 km). –·–·– Coda attenuation for intermediate sampling depth (<400 km). ····· Attenuation due to constant Q_i.

Estimation of scattering properties of lithosphere of Kamchatka based on Monte-Carlo simulation of record envelope of a near earthquake

I.R. Abubakirov and A.A. Gusev

Institute of Volcanology, Petropavlovsk-Kamchatsky, 683006 (U.S.S.R.)

(Received August 18, 1989; revision accepted May 1, 1990)

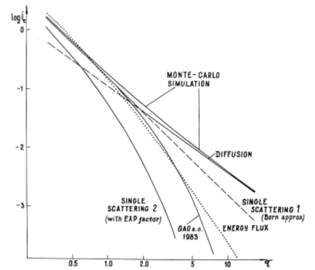

Fig. 4. Dimensionless coda intensity $i_c(\tau)$ according to different models of scattering.

Seismic interferometry

The physics of coda waves cannot be fully understood with classical ray theory. Multiple scattering plays a prominent part in the seismic coda, and seismologists have made use of the radiative transfer theory to model the coda intensity, namely

Physics of the Earth and Planetary Interiors, 67 (1991) 123–136 123
Elsevier Science Publishers B.V., Amsterdam

Simulation of multiple-scattered coda wave excitation based on the energy conservation law

Mitsuyuki Hoshiba *
Meteorological Research Institute, Nagamine 1-1, Tsukuba–shi, Ibaraki 305 (Japan)

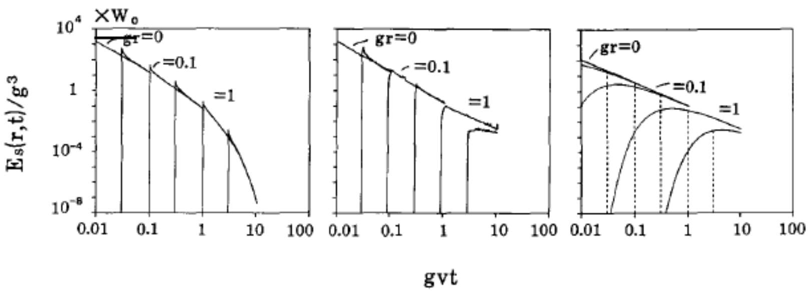

Fig. 6. Time variations of the energy density due to scattered waves at different distances from the source ($gr = 0$, 0.03, 0.1, 0.3, 1.0, 3.0) are shown; horizontal axis represents the non-dimensional time gvt and vertical axis represents $E_s(r, t)/g^3$. The vertical broken lines show the restriction that the maximum velocity of the seismic energy is v. These curves are made from three simulations, $g = 0.1$, 0.01 and 0.001 (km^{-1}).

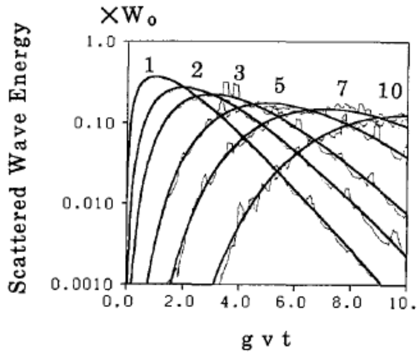

Fig. 5. Partition of scattered energy into different orders of scattering. Fine curves are for the simulation and bold curves denote theoretical prediction $W_0 \cdot (gvt)^n/n! \cdot \exp(-gvt)$. Each numeral is the order of scattering. This figure is based on the scattering coefficient $g = 0.1$ (km^{-1}).

Seismic interferometry

Only a short time ago, the diffusive character of the coda was proven by investigat ing the property of mode equipartition.

VOLUME 86, NUMBER 15 PHYSICAL REVIEW LETTERS 9 APRIL 2001

Observation of Equipartition of Seismic Waves

R. Hennino,[1] N. Trégourès,[2] N. M. Shapiro,[3] L. Margerin,[1,4] M. Campillo,[1] B. A. van Tiggelen,[2,*] and R. L. Weaver[5]

[1]*Laboratoire de Géophysique Interne et Tectonophysique, Observatoire de Grenoble, Université Joseph Fourier, B.P. 53, 38041 Grenoble Cedex, France*

[2]*Laboratoire de Physique et Modélisation des Milieux Condensés, CNRS/Université Joseph Fourier, B.P. 166, 38042 Grenoble Cedex 09, France*

[3]*Instituto de Geofisica, Universidad Nacional Autonoma de México, CU 04510 México, D.F., Mexico*

[4]*Department of Geosciences, Princeton University, Guyot Hall, Princeton, New Jersey 08544*

[5]*Department of Theoretical and Applied Mechanics, University of Illinois at Urbana–Champaign, Urbana, Illinois 61801*

(Received 29 September 2000)

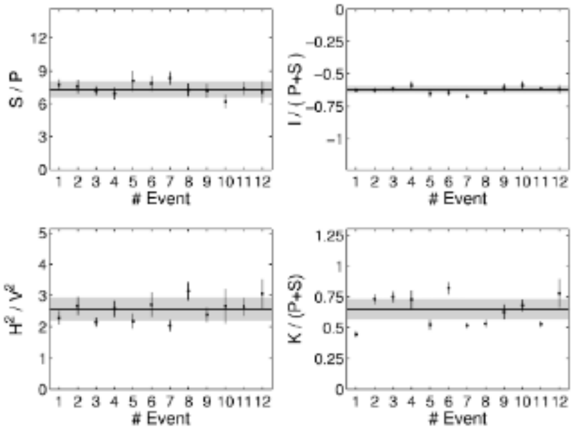

FIG. 2. Observed time-averaged energy ratios S/P (top left), $K/(S+P)$ (top right), H^2/V^2 (bottom left), and $I/(P+S)$ for all 12 events. The shadowed bar denotes the mean value with the standard deviation. The error bars denote the observed time-dependent fluctuations.

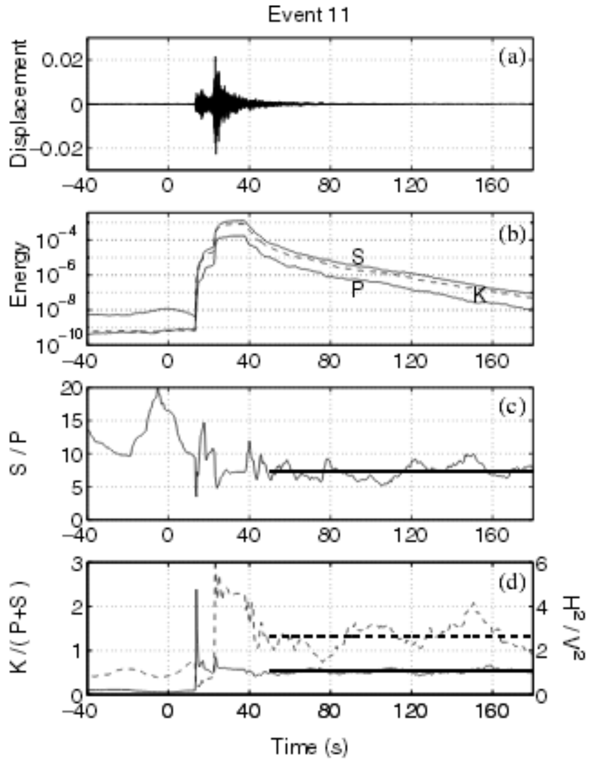

FIG. 1. Observed seismogram, bandpassed between 1 and 3 Hz, for event 11 at an epicentral distance of 35 km from the detection array and a magnitude of 4.3. (a) Linear plot of the bandpassed displacement measured as a function of time. (b) Semilogarithmic plot of the energy density. A distinction is made between kinetic energy (K, dashed line), shear energy (S), and compressional energy (P). (c) Linear plot of the energy ratio S/P. (d) Linear plot of the energy ratios $K/(S+P)$ (solid line) and H^2/V^2 (dashed line). The horizontal lines denote the estimated time average.

Seismic interferometry

Then, rapid developments based on findings which were made in acoustics (e.g., Weaver and Lobkis 2001, Derode et al. 2003).

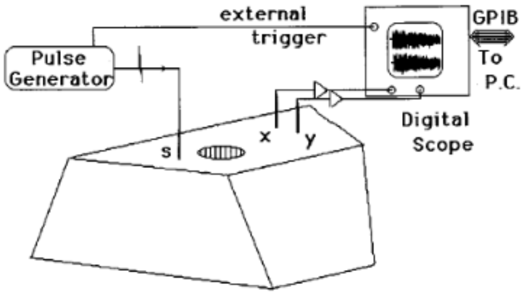

FIG. 1. Irregular block specimen (dimensions ~ $80\times 140\times 200$ mm^3 with 25-mm-diam cylindrical hole) and ultrasonic configuration. A transient pulse is created at s and the resulting diffuse field is detected simultaneously at x and y 20 mm apart.

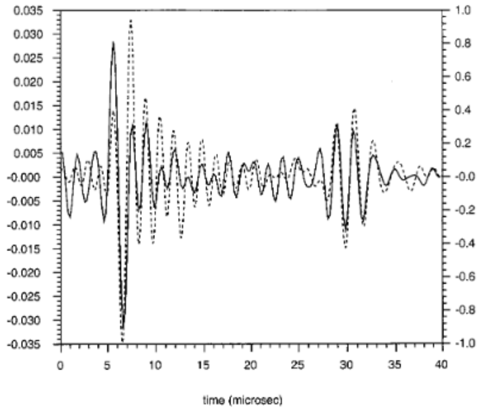

FIG. 3. Comparison of correlation function (solid line) and direct pitch catch signal (dashed line) after low-pass filtering, and including 350 ms of diffuse field data.

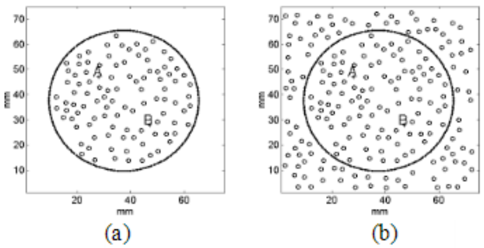

FIG. 4. A and B are receiving points. Two hundred fifty source points are placed regularly around a circle with radius 18.7 mm, 100 scatterers being inside the circle. They completely surround the medium (a), or only partially (b). The boundary conditions on the edges of the grid are absorbing (open medium), in both cases.

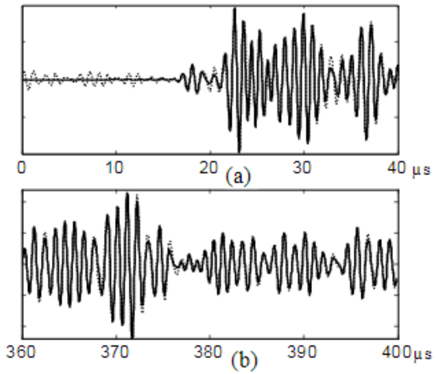

FIG. 5. Comparison between $\Sigma_C\, h_{AC}(t)\otimes h_{BC}(-t)\otimes f(t)$ (dotted line) and $h_{AB}(-t)\otimes f(t)$ in the open scattering medium surrounded by 250 sources C as depicted in Fig. 4(a), at early times (a) and in the late coda, 360 µs later (b). The overall correlation coefficient between waveforms is 97.4%.

Seismic interferometry

Based thereon, Campillo and Paul (2003) correlated earthquake records across a large array to estimate the group velocity distribution.

Long-Range Correlations in the Diffuse Seismic Coda

Michel Campillo* and Anne Paul

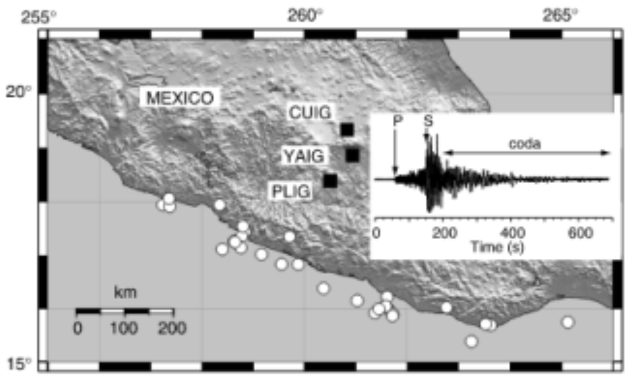

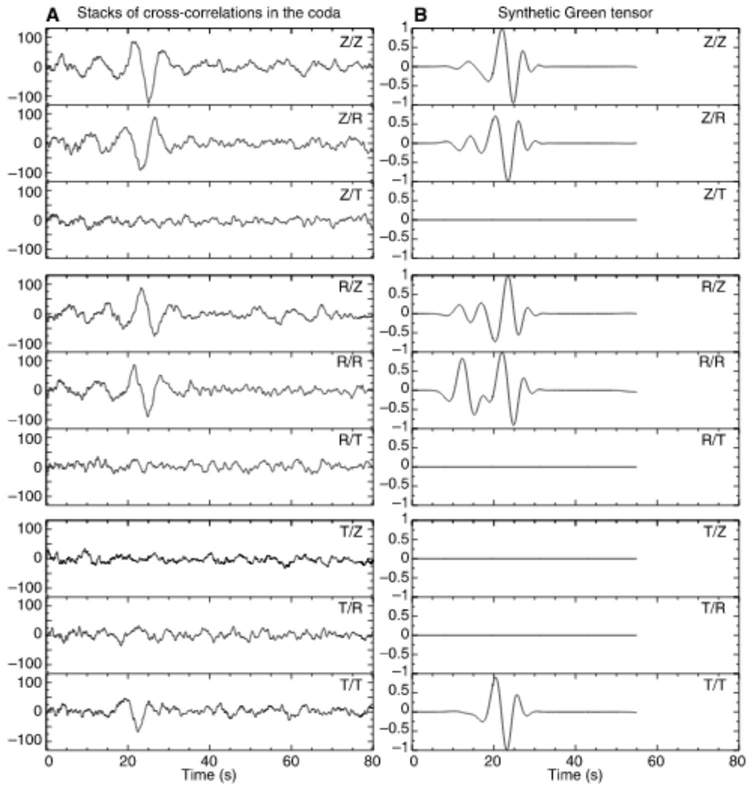

Fig. 3. Comparison between the nine stacks of correlation traces at stations PLIG and YAIG (**A**) and the nine components of the theoretical Green tensor (**B**) computed for a 69-km source-station distance. The 1-D average shear wave velocity model used here was measured for the crust of Central Mexico from inversion of group velocity dispersion curves estimated for paths between the Guerrero-Michoacàn subduction zone and Mexico City (*20*).

GFZ Helmholtz Centre POTSDAM

www.seismo.ethz.ch

Two different issues

time-domain cross correlation

$$C_{fg}(t) \equiv \frac{1}{2T}\int_{-T}^{T} f(\tau)g(\tau+t)\mathrm{d}\tau, \quad \equiv \frac{1}{2T}\int_{-T}^{T} u(x_1,\tau)u(x_2,\tau+t)\mathrm{d}\tau.$$

spatial autocorrelation

$$\phi(\xi) \equiv \frac{1}{A}\int_A F(x)F(x+\xi)\mathrm{d}x,$$

… has been noticed by several authors

JOURNAL OF GEOPHYSICAL RESEARCH, VOL. 110, B11313, doi:10.1029/2005JB003671, 2005

On the correlation of seismic microtremors

Francisco J. Chávez-García
Instituto de Ingeniería, Universidad Nacional Autónoma de México, Torre de Ingeniería, Ciudad Universitaria, Coyoacán, México D.F., México

Francisco Luzón
Departamento de Física Aplicada, Universidad de Almería, Almería, Spain

Bulletin of the Seismological Society of America, Vol. 96, No. 3, pp. 1182–1191, June 2006, doi: 10.1785/0120050181

Retrieval of the Green's Function from Cross Correlation: The Canonical Elastic Problem

by Francisco J. Sánchez-Sesma and Michel Campillo

GEOPHYSICAL RESEARCH LETTERS, VOL. 36, L18301, doi:10.1029/2009GL039131, 2009

Determination of surface-wave phase velocities across USArray from noise and Aki's spectral formulation

Göran Ekström,[1] Geoffrey A. Abers,[1] and Spahr C. Webb[1]

Received 11 May 2009; revised 27 July 2009; accepted 6 August 2009; published 16 September 2009.

Geophys. J. Int. (2006) 167, 1097–1105 doi: 10.1111/j.1365-246X.2006.03170.x

A systematic study of theoretical relations between spatial correlation and Green's function in one-, two- and three-dimensional random scalar wavefields

Hisashi Nakahara
Department of Geophysics, Graduate School of Science, Tohoku University, Aoba-ku, Sendai 980-8578, Japan. E-mail: naka@zisin.geophys.tohoku.ac.jp

Common conclusion: Methods are describing the same physics with a different language.

Two different issues

time-domain cross correlation

$$C_{fg}(t) \equiv \frac{1}{2T}\int_{-T}^{T} f(\tau)g(\tau+t)\mathrm{d}\tau, \ \equiv \frac{1}{2T}\int_{-T}^{T} u(x_1,\tau)u(x_2,\tau+t)\mathrm{d}\tau.$$

spatial autocorrelation

$$\phi(\xi) \equiv \frac{1}{A}\int_A F(x)F(x+\xi)\mathrm{d}x,$$

Geophysical Journal International

Geophys. J. Int. (2010) 182, 454–460 doi: 10.1111/j.1365-246X.2010.04633.x

An explicit relationship between time-domain noise correlation and spatial autocorrelation (SPAC) results

Victor C. Tsai and Morgan P. Moschetti
Geologic Hazards Team, United States Geological Survey, Golden, CO 80401, USA. E-mail: vtsai@post.harvard.edu

$$\begin{aligned}\phi(\xi) &\equiv \frac{1}{2T}\int_{-T}^{T} u(x,t)u(x+\xi,t)\mathrm{d}t.\\ &= \int_0^{2\pi} \rho_S(\theta,\omega)\cos(\omega r\cos\theta/c)\mathrm{d}\theta\\ &= Re\left[\int_0^{2\pi}\rho_S(\theta,\omega)\mathrm{e}^{\mathrm{i}\omega r\cos\theta/c}\mathrm{d}\theta\right],\\ &= 2\pi\,\Phi(\omega)J_0(\omega r/c).\end{aligned}$$

explicit relationship between both theories
e.g., benefit of noise tomography from azimuthal averaging of SPAC

Seismic interferometry

Using long seismic noise sequences (Shapiro and Campillo 2004), it was confirmed that it is possible to estimate the Rayleigh wave component of Green´s functions at low frequencies between two stations by cross-correlating simultaneous recordings.

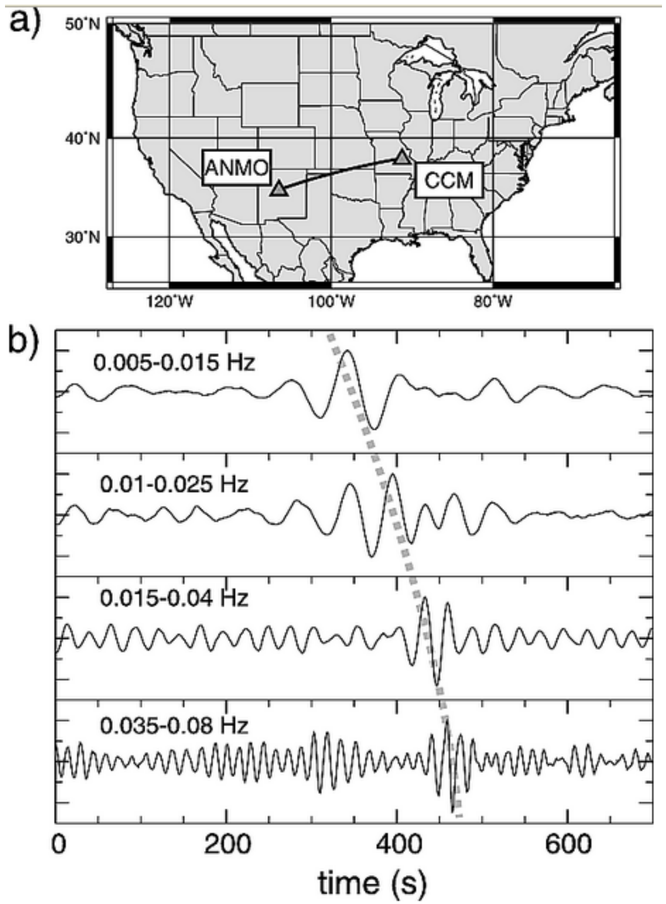

GEOPHYSICAL RESEARCH LETTERS, VOL. 31, L07614, doi:10.1029/2004GL019491, 2004

Emergence of broadband Rayleigh waves from correlations of the ambient seismic noise

N. M. Shapiro[1] and M. Campillo[2]

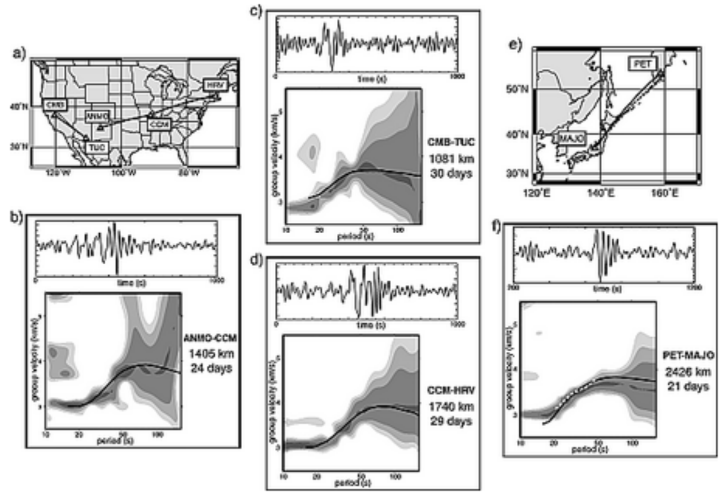

GFZ Helmholtz Centre POTSDAM

www.seismo.ethz.ch

Standard processing

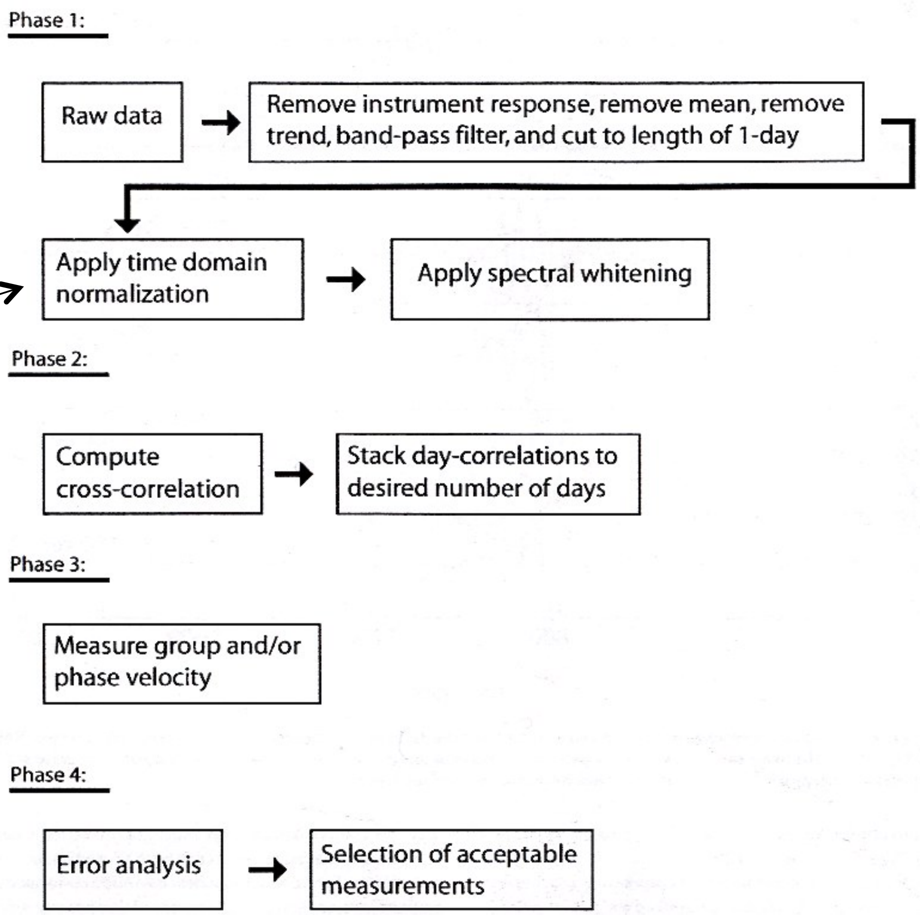

Figure 2. Schematic representation of the data processing scheme. Phase 1 (described in Section 2 of the paper) shows the steps involved in preparing single-station data prior to cross-correlation. Phase 2 (Section 3) outlines the cross-correlation procedure and stacking. Phase 3 (Section 4) includes dispersion measurement and Phase 4 (Section 5) is the error analysis and data selection process.

Remember:
One bit normalization was already proposed by Aki (1957)!

Seismic interferometry

.Surface wave tomography at large regional scales for imaging lateral heterogeneities (e.g., Sabra et al. 2005, Shapiro et al. 2005, Gerstoft et al. 2006, Yao et al. 2006, Cho et al. 2007 and many more)

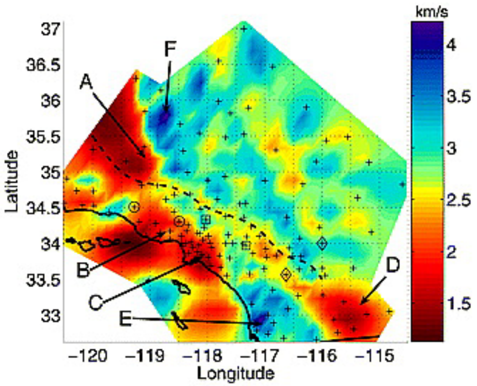

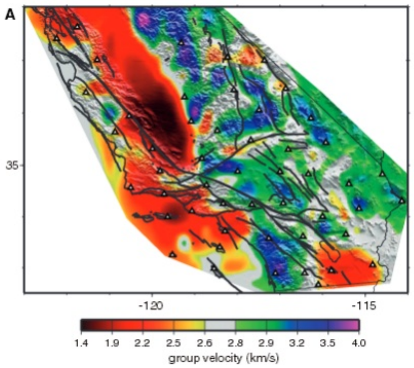

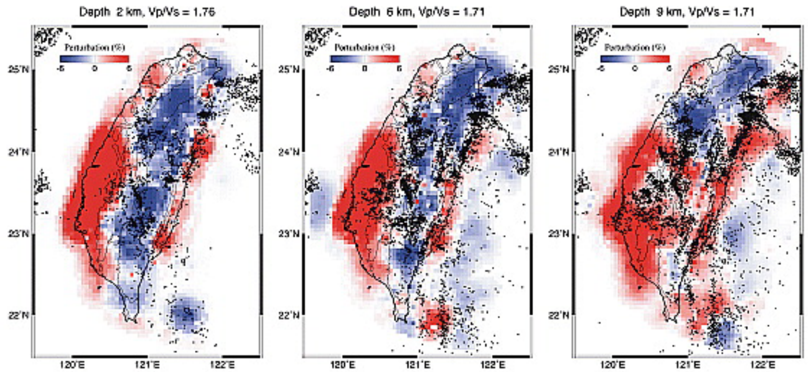

Limitations of seismic interferometry

Global seismic networks have expanded steadily since the 1960s, but are still concentrated on continents and in seismically active regions, i.e. **oceans, particularly in the southern hemisphere, are under-covered**.

The **type of wave used in a model limits the resolution** it can achieve. Longer wavelengths are able to penetrate deeper into the earth, but can only be used to resolve large features. Finer resolution can be achieved with surface waves, with the trade off that they cannot be used in models of the deep mantle. The disparity between wavelength and feature scale causes anomalies to appear of reduced magnitude and size in images.

P- and S-wave models respond differently to the types of anomalies depending on the driving material property. First arrival time based models naturally prefer faster pathways, causing models based on these data to have lower resolution of slow (often hot) features. Shallow models must also consider the significant lateral velocity variations in continental crust.

Limitations of seismic interferometry

Seismic tomography provides **only the current velocity anomalies**. Any prior structures are unknown and the slow rates of movement in the subsurface (mm to cm per year) prohibit resolution of changes over modern timescales.

Tomographic solutions are non-unique. Although statistical methods can be used to analyze the validity of a model, unresolvable uncertainty remains. This contributes to difficulty comparing the validity of different model results.

Computing power can limit the amount of seismic data, number of unknowns, mesh size, and iterations in tomographic models. This is of particular importance in ocean basins, which due to limited network coverage and earthquake density require more complex processing of distant data. Shallow oceanic models also require smaller model mesh size due to the thinner crust.

Tomographic images are typically presented with a color ramp representing the strength of the anomalies. This has the consequence of making equal changes appear of differing magnitude based on visual perceptions of color, such as the change from orange to red being more subtle than blue to yellow. The degree of color saturation can also visually skew interpretations. These factors should be considered when analyzing images.

Seismic interferometry

So far, all presented examples were focusing on large (continental / regional) scales.

First studies reported failures for high-frequency tomography (e.g., Campillo and Paul 2003)

How to go from global / continental scale to the smaller local scale?

It is not just a change of scale / frequency range!

Not just a change of scale...

Spatial variability in the distribution of noise sources

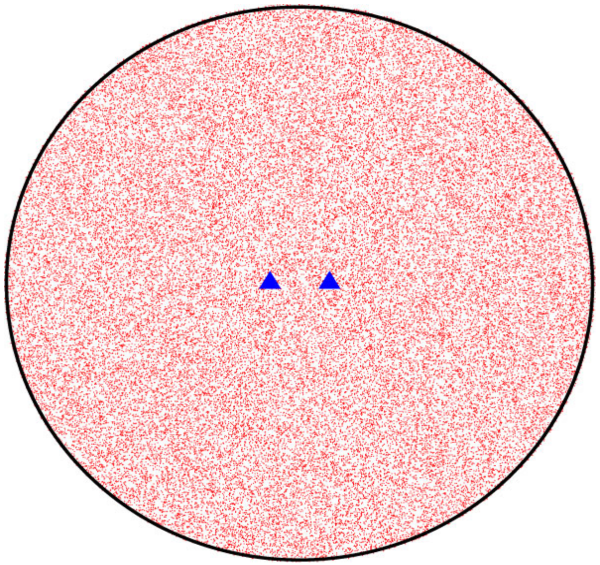

lots of sources

azimuthally homogeneous distribution of sources

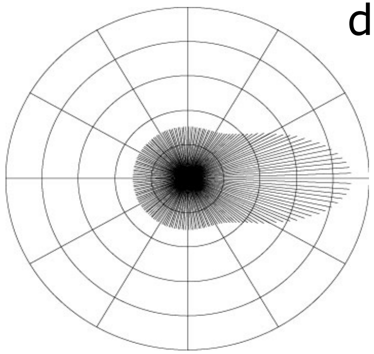

cross-correlation

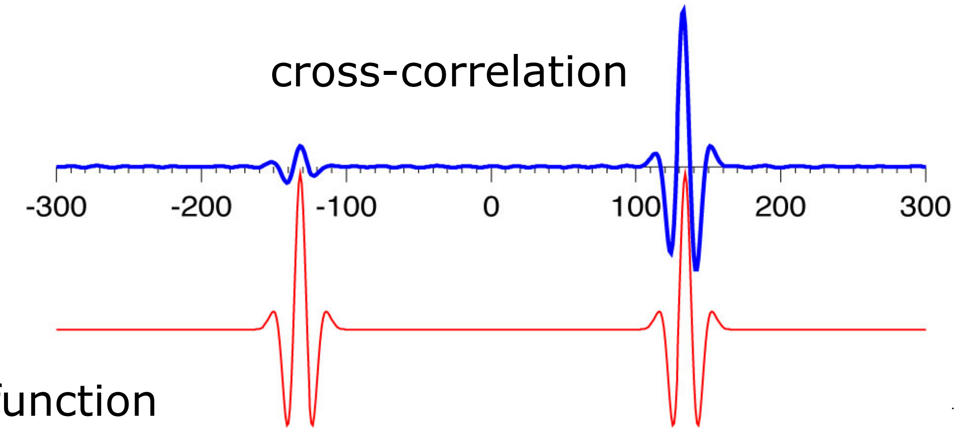

theoretical Green´s function

Not just a change of scale...

Spatial variability in the distribution of noise sources

azimuthally homogeneous
distribution of sources

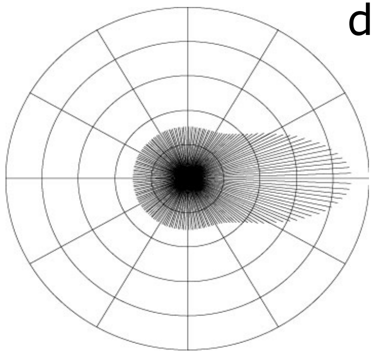

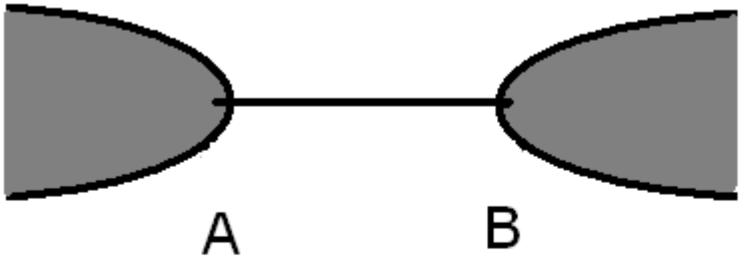

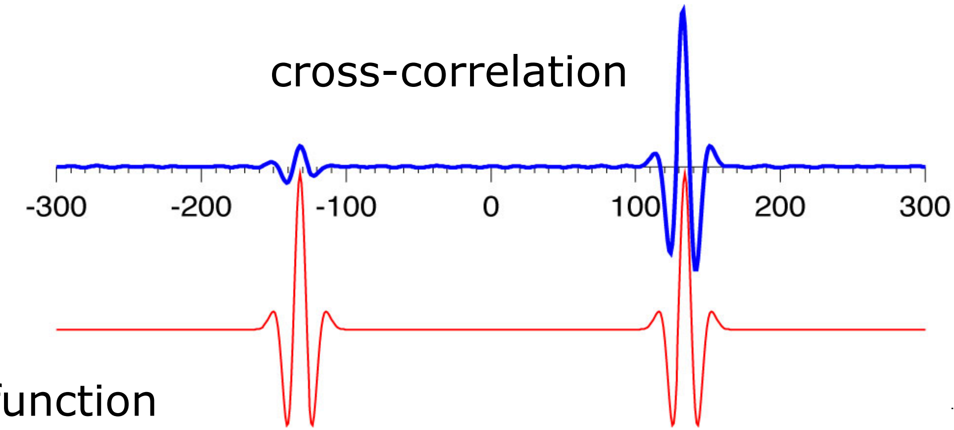

theoretical Green´s function

Not just a change of scale...

Diffusivity of the wave-field at high frequencies

-Wave phases are random

-Waves incident from all directions with equal intensity, i.e. they are azimuthally isotropic.

-Wave amplitude is the same at any point in spacem, i.e. the wavefield is spatially homogeneous.

Mulargia (2012)

The seismic noise wavefield is not diffuse

Francesco Mulargia[a)]
Dipartimento di Fisica, Settore di Geofisica, Università di Bologna, Bologna, Italy

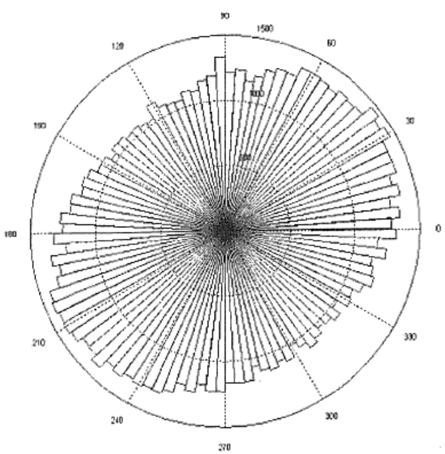

No diffusivity in a strict mathematical / physical sense

Not just a change of scale...

Diffusivity of the wave-field at high frequencies

Pilz and Parolai (2014)


Geophysical Journal International

Geophys. J. Int. (2014) 199, 430–440 doi: 10.1093/gji/ggu273
GJI Seismology

Statistical properties of the seismic noise field: influence of soil heterogeneities

Marco Pilz and Stefano Parolai
Helmholtz Center Potsdam – GFZ German Research Center for Geosciences, Helmholtzstr. 7, D-14467 Potsdam, Germany. E-mail: pilz@gfz-potsdam.de

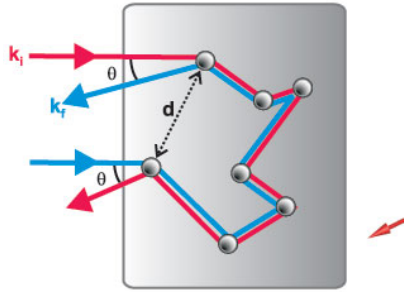

influence of scattering effects

frequency–wavenumber (*f*-*k*) analysis

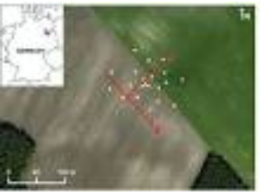

Picozzi et al. (2009)

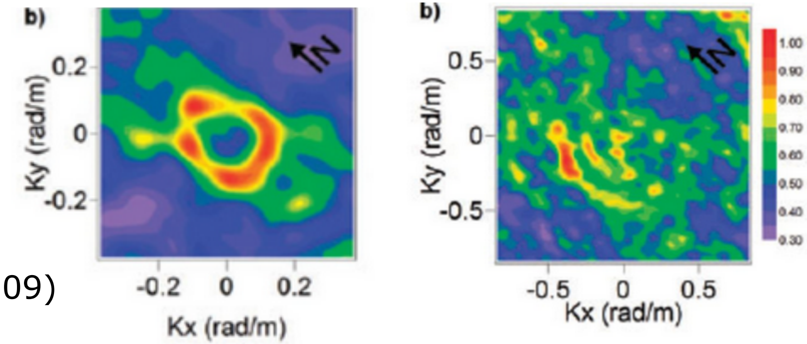

3 Hz 14 Hz

Sufficiently strong seismic noise has to be present for the retrieval of reliable empirical Green´s functions.

If noise is too weak that interstation cross correlations will not provide a reliable Green´s function.

generalization of Claerbout´s conjecture for 3D (Wapenaar 2004) fulfilled

GFZ
Helmholtz Centre
POTSDAM

www.seismo.ethz.ch

Not just a change of scale...

Minimum recording duration required for high-frequency tomography

Chavez-Garcia and Luzon (2005)

JOURNAL OF GEOPHYSICAL RESEARCH, VOL. 110, B11313, doi:10.1029/2005JB003671, 2005

On the correlation of seismic microtremors

Francisco J. Chávez-García
Instituto de Ingeniería, Universidad Nacional Autónoma de México, Torre de Ingeniería, Ciudad Universitaria, Coyoacán
México D.F., México

Francisco Luzón
Departamento de Fisica Aplicada, Universidad de Almeria, Almeria, Spain

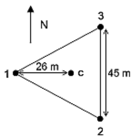

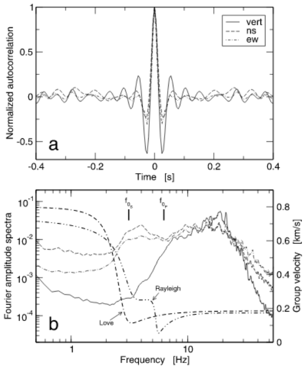

5 minutes?

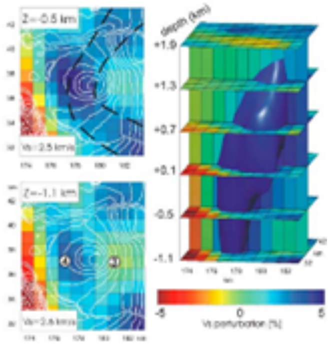

Brenguier et al. (2007)

GEOPHYSICAL RESEARCH LETTERS, VOL. 34, L02305, doi:10.1029/2006GL028586, 2007

3-D surface wave tomography of the Piton de la Fournaise volcano using seismic noise correlations

several months?

Some hours of recording are sufficient.

Renalier et al. (2010)

JOURNAL OF GEOPHYSICAL RESEARCH, VOL. 115, F03032, doi:10.1029/2009JF001538, 2010

Shear wave velocity imaging of the Avignonet landslide (France) using ambient noise cross correlation

F. Renalier,[1] D. Jongmans,[1] M. Campillo,[1] and P.-Y. Bard[1]

Picozzi et al. (2009)

Geophys. J. Int. (2009) 176, 164–174 doi: 10.1111/j.1365-246X.2008.03966.x

Characterization of shallow geology by high-frequency seismic noise tomography

M. Picozzi,[1] S. Parolai,[1] D. Bindi[2] and A. Strollo[1,3]

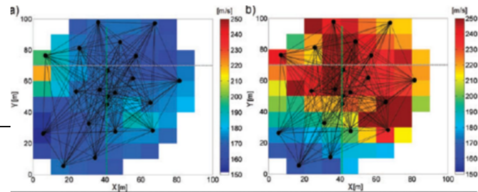

Deriving S-wave velocity models

Seismic noise tomography is usually performed in three steps

Construction of a 2D phase (or group) velocity map

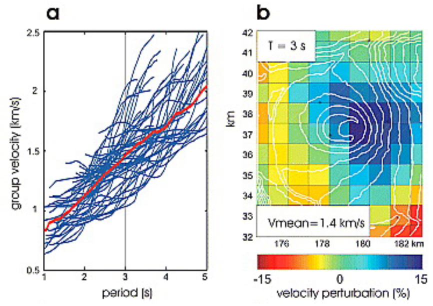

Brenguier et al. (2007)

Pointwise inversion of dispersion data for 1D v_s-depth profiles

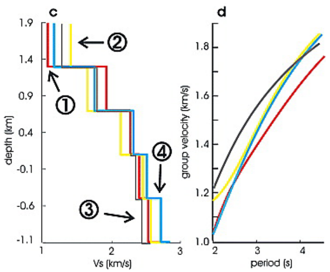

Combination of 1D profiles forming a 3D v_s model

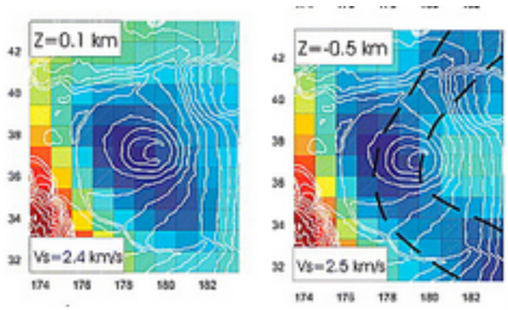

Deriving S-wave velocity models

However, recent developments allow a fast and direct calculation of 3D velocity models

Body-wave tomography

Body waves can propagate vertically, offering a higher resolution for deep velocity structures and discontinuities at depth.

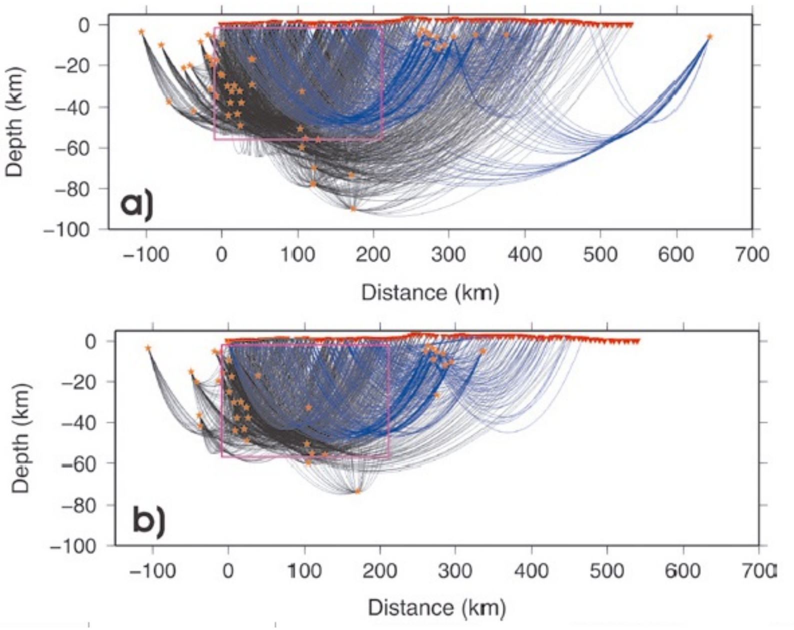

P waves

S waves

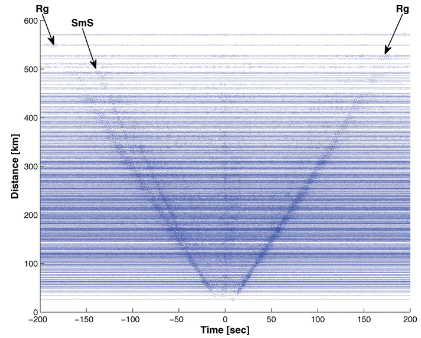

Poli et al. (2012) observed reflected waves from the 410 km and 660 km discontinuities but large uncertainties on the data analysis.

Body-wave tomography

Although the theory suggests that the entire Green's function can be derived from the noise cross-correlation for a diffuse field, in reality, the noise sources are distributed generally near the surface and hence body wave phases are not easily observed.

Takagi et al. (2014) separated body and Rayleigh waves from seismic noise using cross terms of the cross-correlation tensor (which is computationally expensive).

$$\phi^R_{ZZ}(r,\zeta) = a^R_0 J_0(k^R r) + 2\sum_{m=1}^{\infty} i^m c^R_m(\zeta) J_m(k^R r),$$

$$\phi^R_{ZR}(r,\zeta) = -Ha^R_0 J_1(k^R r) - 2H\sum_{m=1}^{\infty} i^m c^R_m(\zeta)\frac{J_{m+1}(k^R r) - J_{m-1}(k^R r)}{2},$$

$$\phi^P_{ZZ}(r,\zeta) = \sum_{n=0}^{\infty}\sum_{m=0}^{n} i^m c^P_{nm}(\zeta)\int_0^{\pi/2} d\theta \sin\theta \left[w^{P*}(\theta) w^P(\theta)\right] P^m_n(\cos\theta) J_m(k^P r\sin\theta),$$

$$\phi^P_{ZR}(r,\zeta) = i\sum_{n=0}^{\infty}\sum_{m=0}^{n} i^m c^P_{nm}(\zeta)\int_0^{\pi/2} d\theta \sin\theta \left[w^{P*}(\theta) u^P(\theta)\right] P^m_n(\cos\theta)\frac{J_{m+1}(k^P r\sin\theta) - J_{m-1}(k^P r\sin\theta)}{2}.$$

Here $c^R_m(\zeta)$ and $c^P_{nm}(\zeta)$ represent the azimuthal dependences as follows:

$$c^R_m(\zeta) = a^R_m \cos m\zeta + b^R_m \sin m\zeta,$$

$$c^P_{nm}(\zeta) = a^P_{nm} \cos m\zeta + b^P_{nm} \sin m\zeta.$$

Body wave tomography from seismic noise

Significant signal processing required

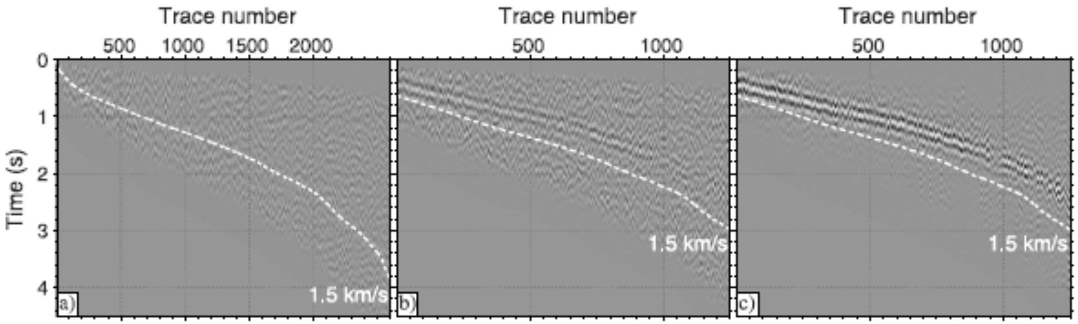

Nakata et al. (2015)

after applying a bandpass-filter trace selection noise suppression filter

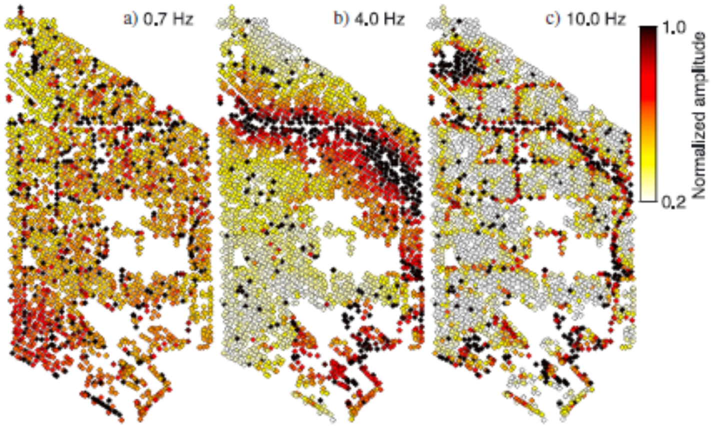

Figure 2. Absolute amplitude of observed ambient noise averaged over 2 h (2:00–4:00 P.M. local time on 17 January (Tue) 2012) in narrow-frequency bands centered at (a) 0.7, (b) 4.0, and (c) 10.0 Hz. Each dot represents each receiver. Amplitudes are normalized at each panel.

GFZ
Helmholtz Centre
POTSDAM

www.seismo.ethz.ch

Body wave tomography from seismic noise

More than 50% of correlation functions discarded!
→ Dense array coverage required

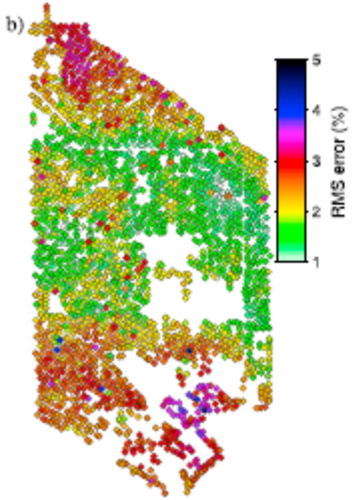

Nakata et al. (2015)

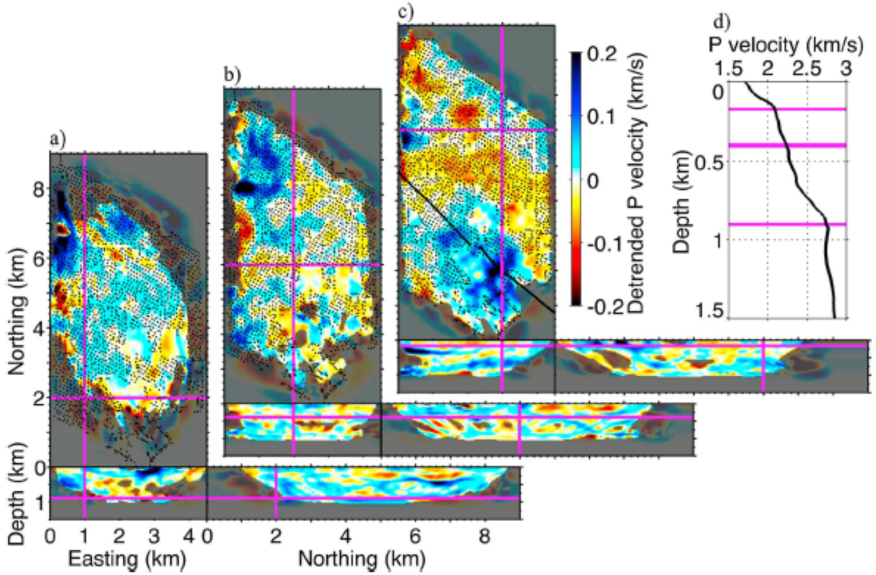

High resolution P wave tomography from seismic noise observed at the free surface

Direct inversion of surface data

Seismic noise adjoint tomography

More accurate forward modelling methods to minimize the frequency-dependent traveltime misfits between the synthetic Green's functions and the empirical Green's function using a preconditioned conjugate gradient method. Meanwhile the 3D model gets improved iteratively updating 3D finite-frequency kernels.

Adjoint Tomography of the Southern California Crust

Carl Tape,[1*] Qinya Liu,[2] Alessia Maggi,[3] Jeroen Tromp[4]

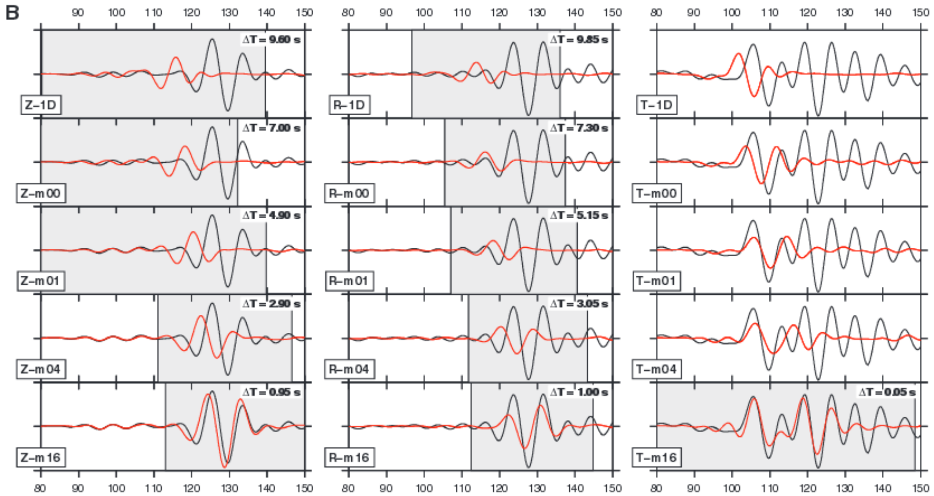

Fig. 1. Iterative improvement of a three-component seismogram. **(A)** Cross section of the V_S tomographic models for a path from a M_w 4.5 earthquake (stars) on the White Wolf fault to station DAN (triangles) in the eastern Mojave Desert. Vertical exaggeration is 3.0. Upper right is the initial 3D model, $\mathbf{m}_{00}$; lower right is the final 3D model, $\mathbf{m}_{16}$; and lower left is the difference between the two, $\ln(\mathbf{m}_{16}/\mathbf{m}_{00})$. Faults labeled for reference are San Andreas (SA), Garlock (G), and Camp Rock (CR). **(B)** Iterative three-component seismogram fits to data for models $\mathbf{m}_{00}$, $\mathbf{m}_{01}$, $\mathbf{m}_{04}$, and $\mathbf{m}_{16}$. Also shown are synthetic seismograms computed for a standard 1D model (table S1). Synthetic seismograms (red) and recorded seismograms (black), filtered over the period range 6 to 30 s. Left column, vertical component (Z); center column, radial component (R); right column, transverse component (T). Inset "ΔT" label indicates the time shift between the two windowed records that provides the maximum cross-correlation (*16*, *21*).

Direct inversion of surface data

Seismic noise adjoint tomography

Allows a good resolution of low velocities zones

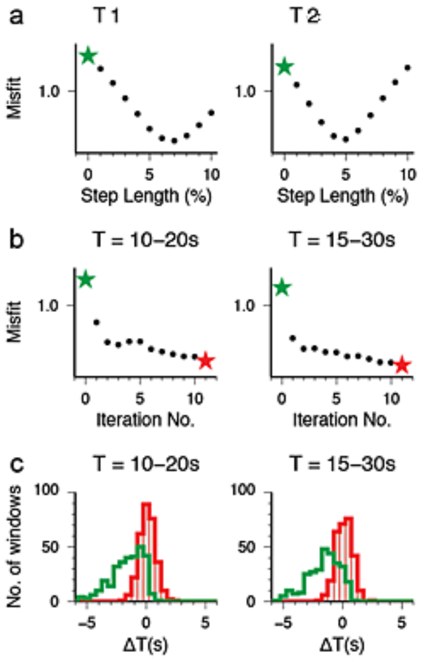

Chen et al. (2014)

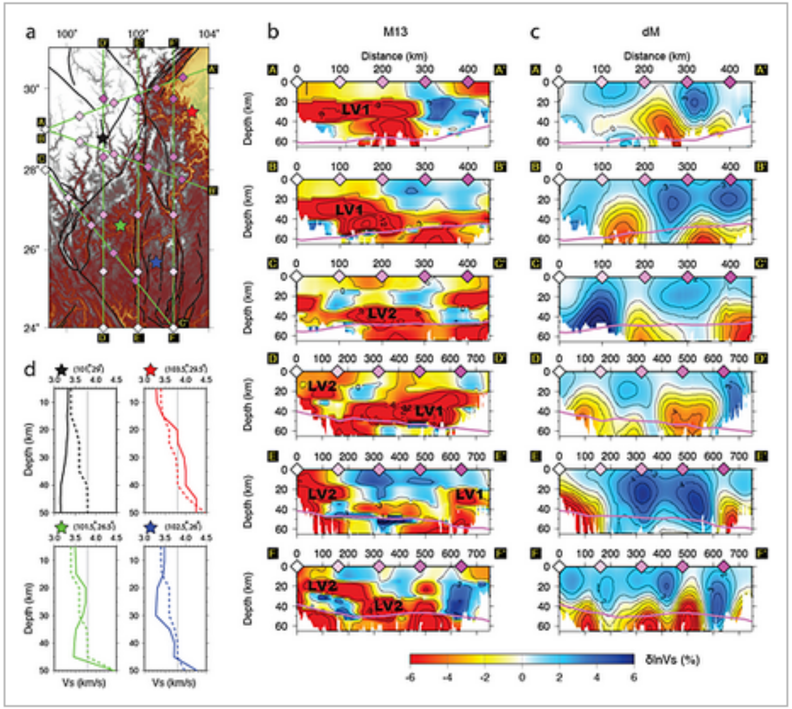

Figure 4.

Open in figure viewer | Download Powerpoint slide

(a) Map indicating six profiles with green lines anchored by light to deep pink diamonds, with their vertical cross sections of shear wave speed anomalies shown in Figure 4b for M13 and Figure 4c for dM. LV1 and LV2 mark the low wave speed zones with 6 – 12% wave speed reduction in Figure 4b. Solid pink line denotes the Moho interface in Figures 4b and 4c. (d) One-dimensional profiles of absolute shear wave speeds (solid line — M13, dash line — Mref) for four points in different tectonic regions marked by stars in map. Grey lines in the 1D profile plots are reference line of $V_S = 3.8$ km/s, which is the lower crust shear wave speed of Mref

High computational cost (in particular at high frequencies) until sufficiently accurate 3D models are found

Direct inversion of surface data

Ray tracing at each frequency

Avoiding assumption of great-circle propagation of surface waves

Iteratively updating sensitivity kernels and ray paths of frequency-dependent dispersion curves for directly deriving 3D v_s models

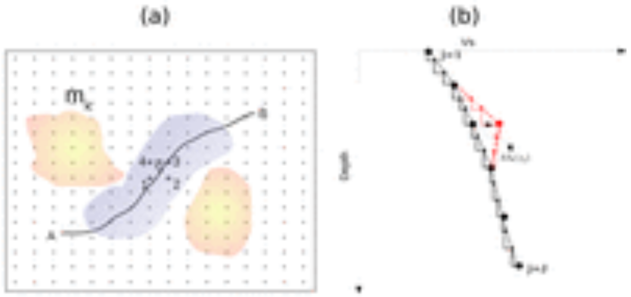

Fang et al. (2015)

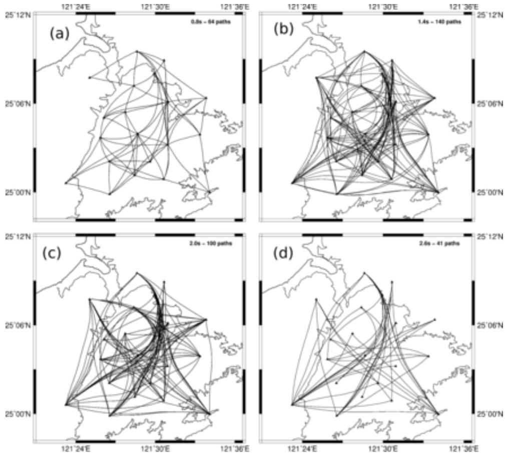

Higher resolution in regions with dense ray coverage

But problems in regions with poor or even no data constraint reported

Direct inversion of surface data

The linear tomography problem of computing the integral travel time (t) for a given slowness (s) along a raypath is given by

$$t = \int s \cdot dl$$

where the *dl* is the line element along the raypath. Equation can also be expressed in a simple discrete matrix form,

$$\mathbf{t} = \mathbf{L_1 s}$$

t is the vector of observed travel times, **s** is the slowness of the cells, and $\mathbf{L_1}$ is an *MxN* matrix of ray-path segments, namely, *M* rays crossing the medium, divided into *N* cells.

Direct inversion of surface data

This average slowness was the initial guess $s^{(k=1)}$ for the iterative scheme. Then, a new solution $s^{(k+1)}$ was determined by solving the following equation

$$\mathbf{W\Delta t^{(k)} = L_2 \Delta s^{(k)}}$$

in which $\mathbf{\Delta t}$ is the vector of the normalized misfit between the observed and theoretical travel times, $[t_o - t_t]/ t_o$.

$\mathbf{\Delta s}$ is the vector of the normalized slowness modification $[s^{(k)} - s^{(k-1)}]/s^{(k)}$.

The diagonal matrix $\mathbf{W}_{(MxM)}$ is made up of weighting factor elements defined by the adaptive bi-weight estimation method, and was introduced to stabilize the iteration process.

Direct inversion of surface data

The design matrix $\mathbf{L_2}$ is derived from $\mathbf{L_1}$. After that some proper modification was included to account for *a priori* constraints on the solution. In particular, it is expressed as

$$\mathbf{L}_2 = \begin{bmatrix} \mathbf{W}\mathbf{L}_1 \\ \mathbf{K}(\delta^2)\mathbf{M} \end{bmatrix} \qquad (9)$$

where the upper block is the ray-path segment matrix $\mathbf{L_1}$ properly weighted by the matrix **W**, while, the damping coefficient δ^2 and the matrices **K** and **M** describe the *a priori* constraints imposed on the solution.

Direct inversion of surface data

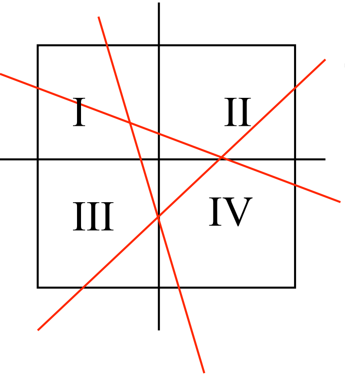

The matrix **K**(NxN) weights the data depending on the number, length, and orientation of each ray-path segment crossing each *Ni* cell.

Each cell *Ni* is first divided into four quadrants. Then, the length of the rays passing through each sector is summed, resulting in a 2x2 ray density matrix. The ray density matrix was factorized by performing the singular value decomposition (SVD).

The singular values ($\lambda 1$, $\lambda 2$) were used to compute the ellipticity ($\lambda min/\lambda MAX$) of the ray density matrix.
Ellipticity close to 1, means that a good resolution for a given cell is achieved

The elements of the matrix **K** were computed by multiplying the ellipticity for the number of rays crossing each cell.

Direct inversion of surface data

Matrix **M** constrains the solution to vary smoothly over the 2D domain. It increases the stability of the inverse problem by reducing of the influence of travel time errors.
The implementation of that smoothness constraint consists in adding a system of equations to the original travel time inversion problem,

$$s_{x,y} - \sum_{i=1}^{R} a_i s_{x-dx_i, y-dy_i} = 0$$

where R is the number of cells surrounding the selected one, $s_{x,y}$, and a_i are the normalized weights.

Direct inversion of surface data

Assigning proper weights to each of the subcells

Horizontal weights

a)

-0.4	-0.2
1	-0.4

b)

-0.1	-0.15	-0.1
-0.15	**1**	-0.15
-0.1	-0.15	-0.1

c)

-0.15	-0.2	-0.15
-0.2	**1**	-0.2

Vertical weights

Weighting scheme based on the analytical solution of displacement components for surface waves in a half space (Aki and Richards 1980, Borcherdt 2008)

Rayleigh waves

$$u_3(|\mathbf{z}|) = \mathrm{l}e^{\mathrm{l}k\mathrm{z}\cdot e_z} - \mathrm{s}e^{\mathrm{p}k\mathrm{z}\cdot e_z}$$

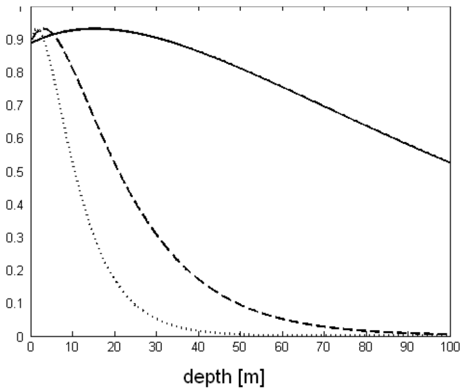

Love waves

$$u(|\mathbf{z}|) = \cos(\mathrm{Re}[B_n]\mathbf{z}\cdot\mathbf{e}_z)e^{i\frac{\omega}{c_{Love}}\mathbf{x}\cdot\mathbf{e}_x}$$

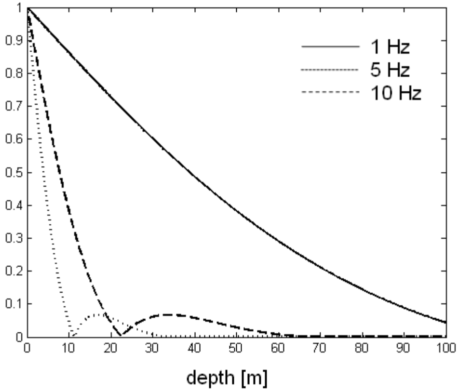

Direct inversion of surface data

Linearization of the inversion

Allows accounting for the effect of topography

$f_1 > f_2 > f_3$

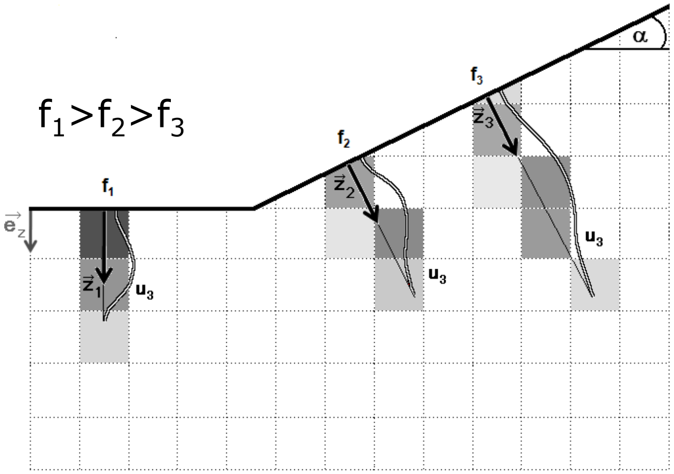

Pilz et al. (2013)

Direct inversion of surface data

$$\mathbf{L_2} = \begin{bmatrix} \mathbf{WL_1} \\ \mathbf{K}(\delta^2)\mathbf{M} \end{bmatrix}$$

The term δ^2 is a damping coefficient introduced to balance resolution and instability in the inversion analysis

After some trial and error tests, $\delta 2$ was fixed to 0.5

Application to near-surface imaging

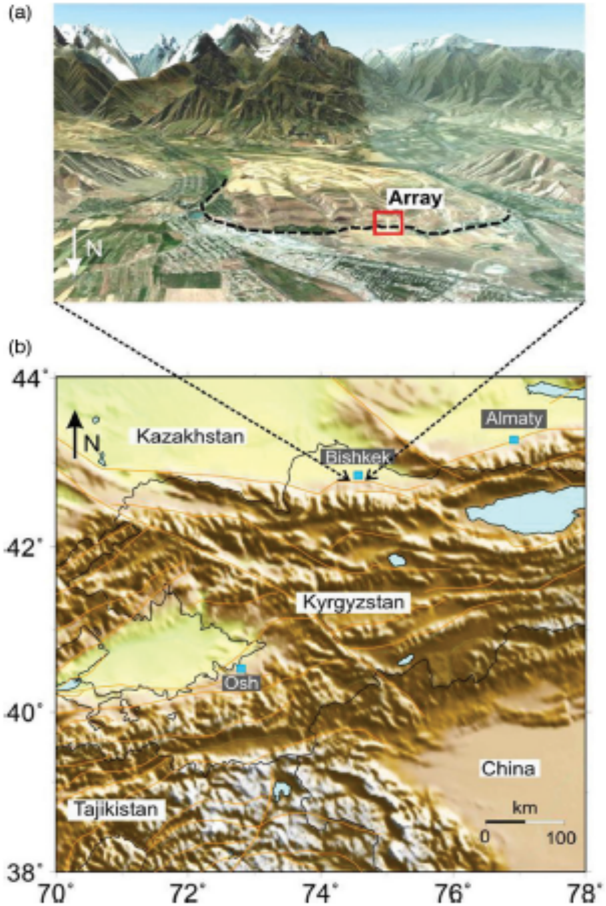

Figure 6. (a) Satellite image showing the southern outskirts of Bishkek facing the Ala-Too range. The topography is exaggerated by two times. Location of the array measurement is indicated. The dotted line shows the Issyk-Ata fault following Chediya *et al.* (2000). Google Earth, © 2012, CNS Spot Image © 2012, Digital Globe © 2012. (b) Map of Central Asia. Major faults are mapped in orange.

Geophysical Journal International

Geophys. J. Int. (2013) doi: 10.1093/gji/ggt214
Geophysical Journal International Advance Access published June 18, 2013

Three-dimensional passive imaging of complex seismic fault systems: evidence of surface traces of the Issyk-Ata fault (Kyrgyzstan)

Marco Pilz, Stefano Parolai and Dino Bindi
Helmholtz Center Potsdam – GFZ German Research Center for Geosciences, Helmholtzstr. 7, 14467 Potsdam, Germany. E-mail: pilz@gfz-potsdam.de

Application to near-surface imaging

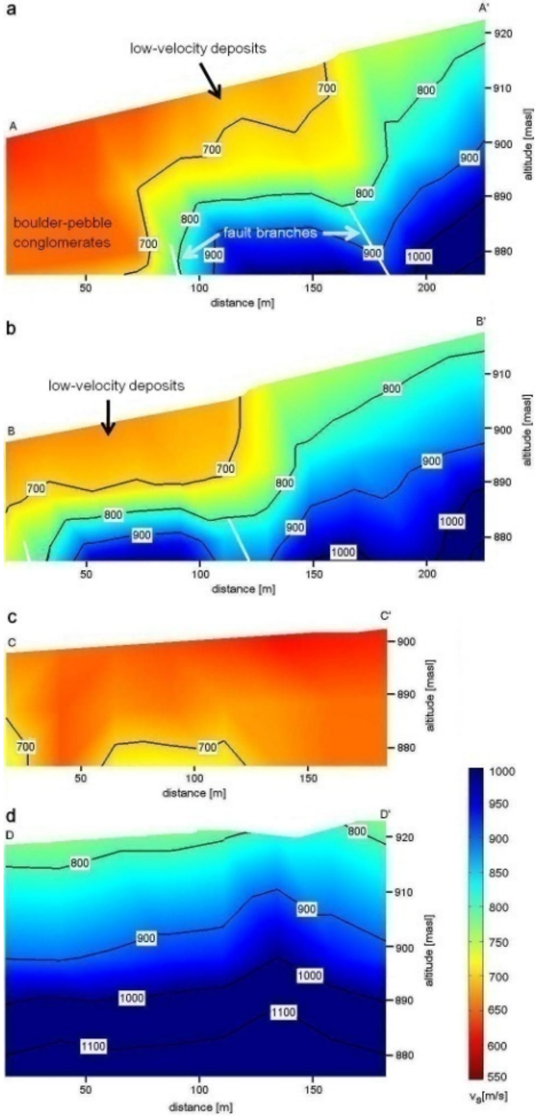

Geophysical Journal International

Geophys. J. Int. (2013)
doi: 10.1093/gji/ggt214
Geophysical Journal International Advance Access published June 18, 2013

Three-dimensional passive imaging of complex seismic fault systems: evidence of surface traces of the Issyk-Ata fault (Kyrgyzstan)

Marco Pilz, Stefano Parolai and Dino Bindi
Helmholtz Center Potsdam – GFZ German Research Center for Geosciences, Helmholtzstr. 7, 14467 Potsdam, Germany. E-mail: pilz@gfz-potsdam.de

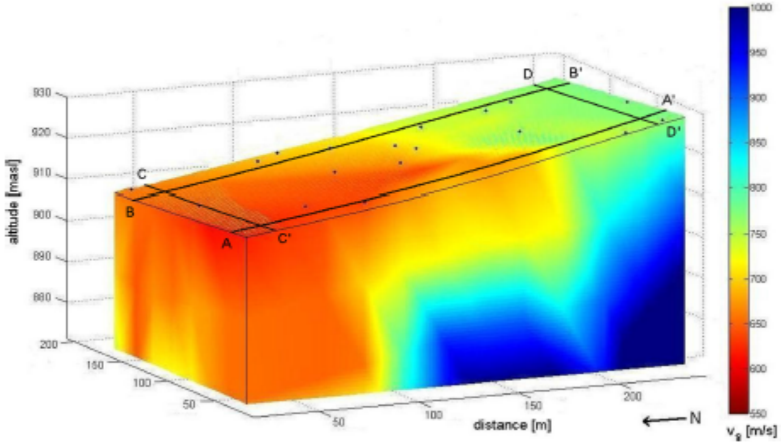

Figure 7. Inversion results of measurements on the Issyk-Ata fault obtained after 500 iterations. Topography is exaggerated about three times. The dots represent locations of the sensors. Locations of cross-sections shown in Fig. 8 are indicated by straight black lines.

Application to near-surface imaging

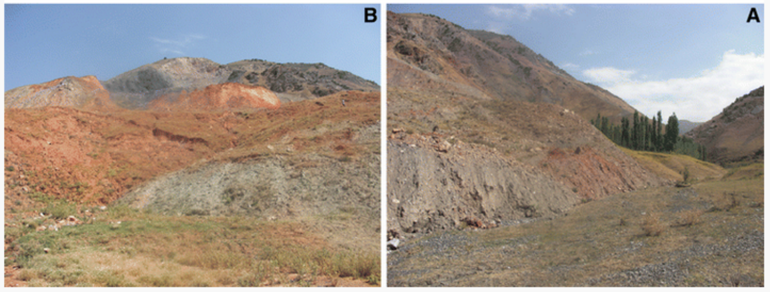

Pure and Applied Geophysics
August 2014, Volume 171, Issue 8, pp 1729–1745

Combining Seismic Noise Techniques for Landslide Characterization

Marco Pilz, Stefano Parolai, Dino Bindi, Annamaria Saponaro, Ulan Abdybachaev

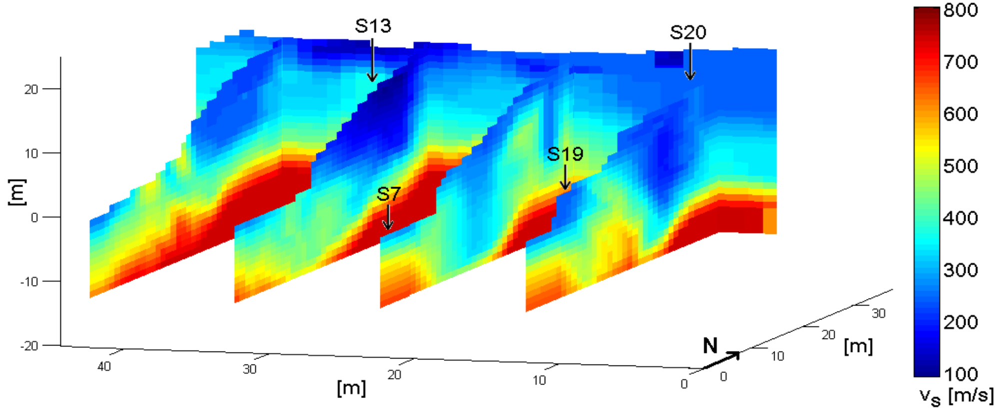

Resolution capabilities

Be aware of the limitations! While modern inversion methods are providing unprecedented resolution for 3-D seismic structure models, there remains a lack of meticulous validation and uncertainty assessment in 3-D Earth imaging.

Geophysical Journal International

Geophys. J. Int. (2013) 192, 676–680 doi: 10.1093/gji/ggs057

EXPRESS LETTER

Resolution tests revisited: the power of random numbers

Jeannot Trampert,[1] Andreas Fichtner[1] and Jeroen Ritsema[2]

[1]*Department of Earth Sciences, Utrecht University, P.O. Box 80021, NL-3508 TA, Utrecht, The Netherlands. E-mail: jeannot@geo.uu.nl*
[2]*Department of Earth and Environmental Sciences, University of Michigan, 2534 C. C. Little Building, 1100 North University Ave., Ann Arbor, MI, 48109-1005, USA*

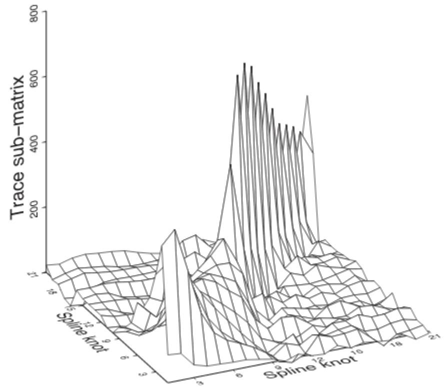

Figure 3. Traces of the 21 × 21 submatrices for model S40RTS.

... has significantly lower vertical and horizontal resolution in the transition zone despite the use of many high-quality overtone surface wave data. The reason for this is probably a **specific choice for the weighting parameters in the inversion**.

Resolution capabilities

AGU PUBLICATIONS

Geophysical Research Letters

RESEARCH LETTER
10.1002/2014GL062571

On the validation of seismic imaging methods

Monica Maceira[1], Carene Larmat[1], Robert W. Porritt[2,3], David M. Higdon[1], Charlotte A. Rowe[1], and Richard M. Allen[3]

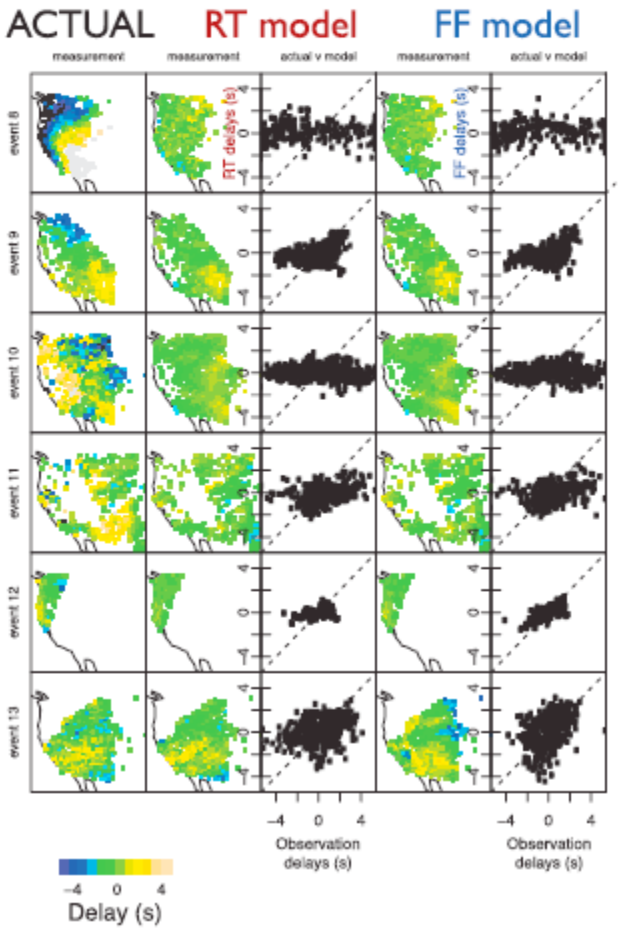

Velocity variations depending on the algorithm used.

Resolution capabilities

Geophysical Journal International

Geophys. J. Int. (2016) **205**, 1221–1243
Advance Access publication 2016 March 7
GJI Seismology
doi: 10.1093/gji/ggw084

On the use of sensitivity tests in seismic tomography

N. Rawlinson[1] and W. Spakman[2,3]
[1]*School of Geosciences, University of Aberdeen, Aberdeen, Scotland AB24 3UE. E-mail: nrawlinson@abdn.ac.uk*
[2]*Department of Earth Sciences, Faculty of Geosciences, Utrecht University, PO BOX 80115, 3584 TC, Utrecht, The Netherlands*
[3]*Centre of Earth Evolution and Dynamics (CEED), University of Oslo, 0316 Oslo, Norway*

Sensitivity analysis with synthetic models is widely used in seismic tomography as a means for assessing the spatial resolution of solutions produced by, in most cases, linear or iterative nonlinear inversion schemes.
The most common type of synthetic reconstruction test is the so-called **checkerboard resolution** test in which the synthetic model comprises an alternating pattern of higher and lower wave speed (or some other seismic property such as attenuation) in 2-D or 3-D.

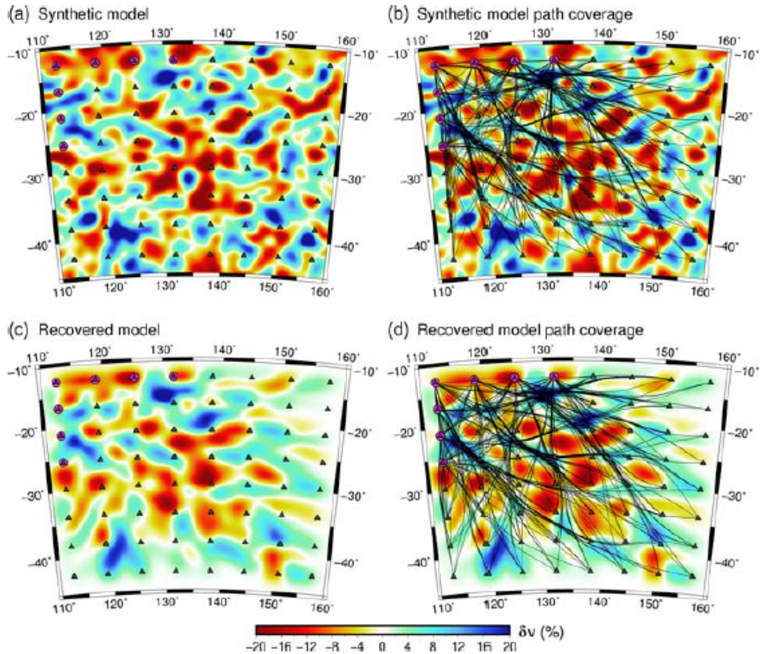

Resolution capabilities

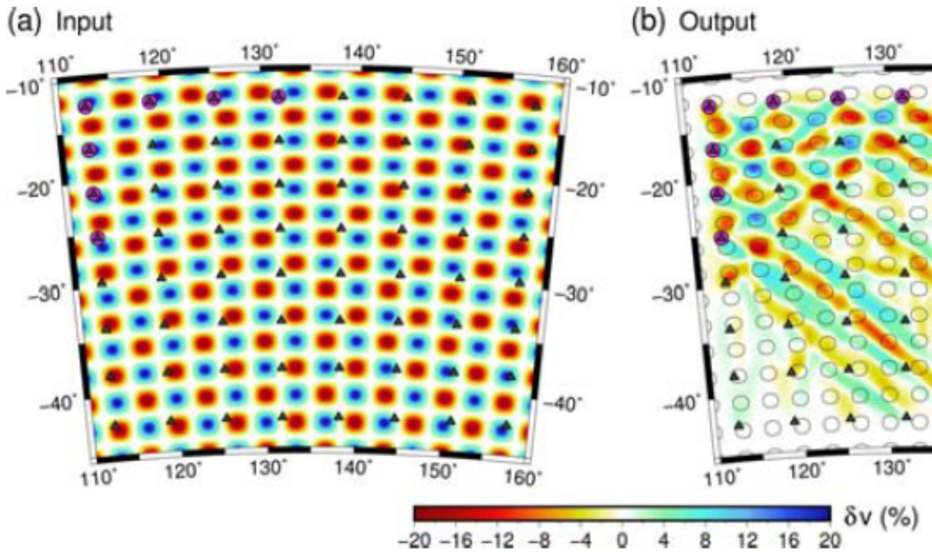

Figure 2. (a) Input checkerboard model; (b) recovered model using the path geometry of Fig. 1(d). Black contour lines represent the ±10 per cent contour interval of the input checkerboard.

(a) Input (b) Output

Checkerboard-tests only provide indirect evidence of quantitative measures of reliability such as resolution and uncertainty, giving a potentially misleading impression of the range of scale-lengths that can be resolved, and not giving a true picture of the structural distortion or smearing that can be caused by the data coverage.

Resolution capabilities

A better alternative: Spike-tests

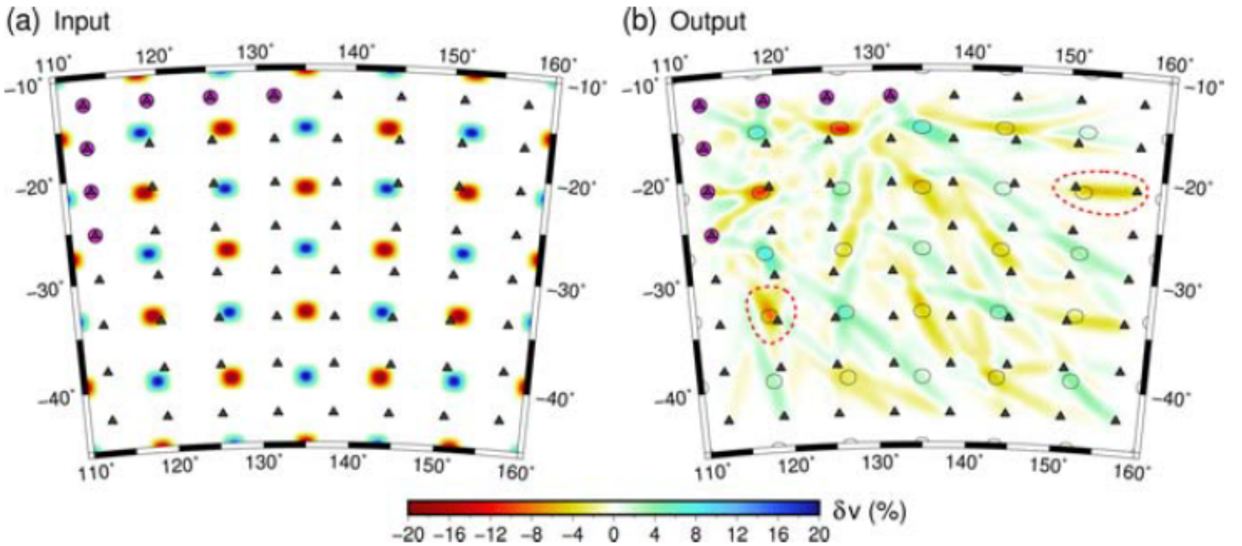

Figure 3. (a) Input spike model; (b) recovered model using the path geometry of Fig. 1(d). Black contour lines represent the ±10 per cent contour interval of the input spikes. Closed dashed red lines highlight the locations of features discussed in the text.

Resolution capabilities

Error propagation

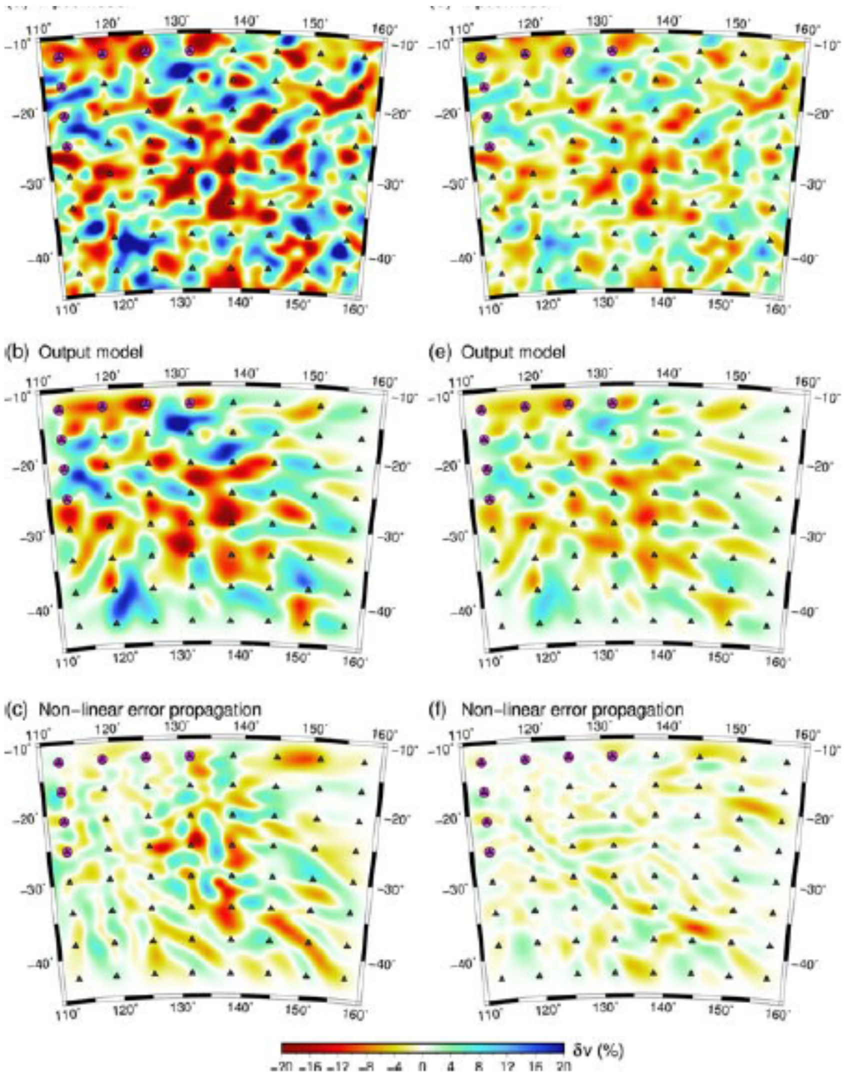

Figure 8. Test results illustrating the influence of nonlinear error propagation in the solution. Left column uses the same input model as in Fig. 1, while the input model for the right column has an identical pattern of anomalies but with a 50 per cent reduction in amplitude. (a), (d) Input model; (b), (e) output model from iterative nonlinear inversion; (c), (f) estimate of nonlinear error propagation as given by the term $\mathbf{G}^{-g}\mathbf{E}\mathbf{m}_p$ in eq. (18).

Resolution capabilities

(i) As for formal resolution analysis, sensitivity tests only strictly apply to linear tomographic problems. However, they can provide useful insight in the presence of weakly nonlinear inverse problems.

(ii) Theoretical prediction errors (e.g. the use of approximate forward theory like ray tracing) are ignored in sensitivity analysis, yet it is conceivable that they may influence the results significantly.

(iii) Sensitivity tests are only useful for the detection of *lack of resolution and not the detection of model recovery. Good recovery* of one particular test model is relatively meaningless.

(iv) Theoretical prediction errors (e.g. the use of approximate forward theory like ray tracing) are ignored in sensitivity analysis, yet it is conceivable that they may influence the results significantly.

Resolution capabilities

(v) Discrete spike tests are more useful for assessing the resolving power of the data set to recover structure compared to traditional checkerboards, which feature a tight oscillatory pattern of positive and negative anomalies.

(vi) Synthetic experiments should test lack of resolution across at least the same range of scale lengths that are found or interpreted in the observational model. For synthetic models containing only one wavelength of structure, multiple tests involving different-sized anomalies should be used.

(vii) Input structures that closely resemble the output structure from the observational model should not be used in synthetic tests, as they cannot detect lack of resolution.

(viii) It is important to use sensible colour scales that avoid large fluctuations in intensity and gradient.

From imaging to monitoring

For monitoring of volcanoes, fault zones, dams, and hydro-carbon or geothermal reservoirs, it is valuable to observe changes of elastic properties like seismic velocity.

Popular technique:

GEOPHYSICAL RESEARCH LETTERS, VOL. 33, L21302, doi:10.1029/2006GL027797, 2006

Passive image interferometry and seasonal variations of seismic velocities at Merapi Volcano, Indonesia

C. Sens-Schönfelder[1] and U. Wegler[1]

Received 9 August 2006; revised 25 September 2006; accepted 2 October 2006; published 1 November 2006.

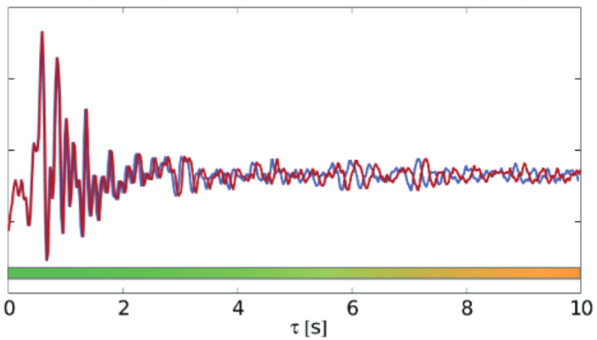

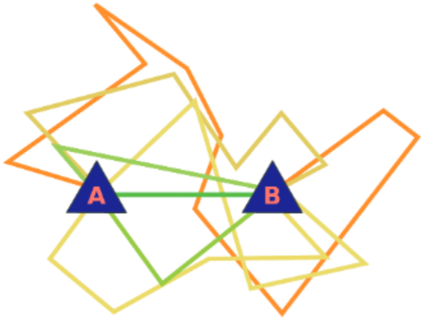

GFZ

Helmholtz Centre
Potsdam

www.seismo.ethz.ch

From imaging to monitoring

It allows to infer changes in the medium by comparing the GFs retrieved from the noise records at different time periods.

GEOPHYSICAL RESEARCH LETTERS, VOL. 33, L21302, doi:10.1029/2006GL027797, 2006

Passive image interferometry and seasonal variations of seismic velocities at Merapi Volcano, Indonesia

C. Sens-Schönfelder[1] and U. Wegler[1]

Received 9 August 2006; revised 25 September 2006; accepted 2 October 2006; published 1 November 2006.

First, a reference autocorrelation ϕref is computed as the mean over all available daily autocorrelations.
Then the daily autocorrelations ϕd are stretched and compressed on the time axis with respect to zero lag time. For determining traveltime fluctuations, the similarity between the unstretched reference and the stretched daily autocorrelation function in the chosen time window is determined for each stretching factor ϵ by the correlation coefficient cc

$$\mathrm{cc}(\epsilon) = \frac{\int_{t_1}^{t_2} \phi_{\mathrm{d}}(t(1+\epsilon))\phi_{\mathrm{ref}}(t)\mathrm{d}t}{\left(\int_{t_1}^{t_2} \phi_{\mathrm{d}}^2(t(1+\epsilon))\mathrm{d}t \int_{t_1}^{t_2} \phi_{\mathrm{ref}}^2(t)\mathrm{d}t\right)^{1/2}}$$

$$\mathrm{d}t = -t\,\frac{\mathrm{d}v}{v}$$

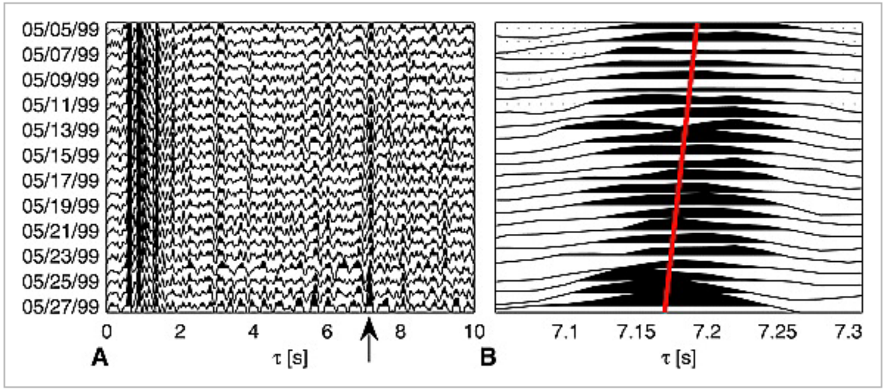

From imaging to monitoring

Seismic velocity variations at TCDP are controlled by MJO driven precipitation pattern and high fluid discharge properties

G. Hillers[a,*], M. Campillo[a], K.-F. Ma[b]

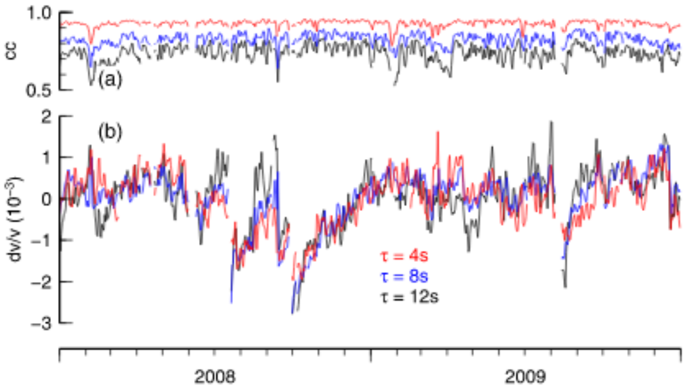

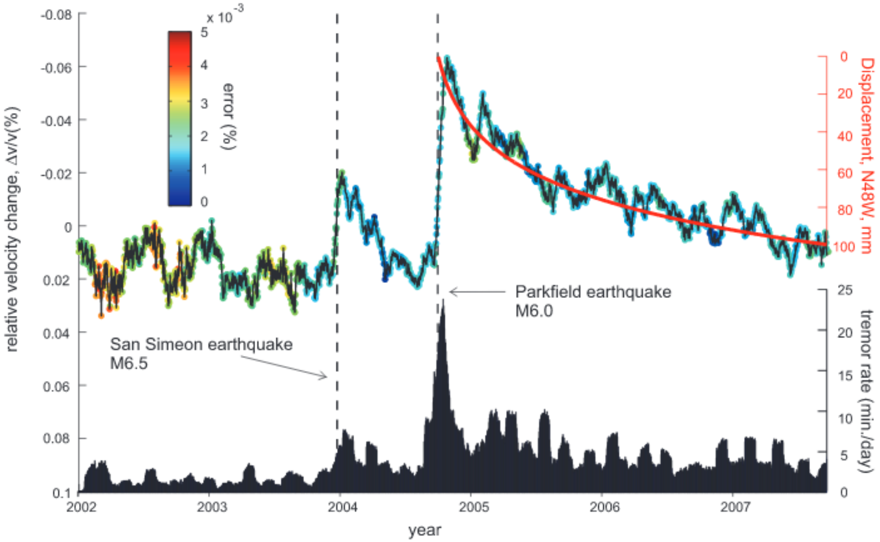

Postseismic Relaxation Along the San Andreas Fault at Parkfield from Continuous Seismological Observations

F. Brenguier,[1,2*] M. Campillo,[2] C. Hadziioannou,[2] N. M. Shapiro,[1] R. M. Nadeau,[3] E. Larose[2]

From imaging to monitoring

To be used with caution!

GFZ
Helmholtz Centre POTSDAM

www.seismo.ethz.ch

From imaging to monitoring

EARTHQUAKE DYNAMICS

Mapping pressurized volcanic fluids from induced crustal seismic velocity drops

F. Brenguier,[1*] M. Campillo,[1] T. Takeda,[2] Y. Aoki,[3] N. M. Shapiro,[4] X. Briand,[1] K. Emoto,[2] H. Miyake[3]

We used the approach of Gomberg and Agnew (*15*) to estimate the level of dynamic strain $\Delta\xi$ and dynamic stress $\Delta\sigma$ from the observed peak ground velocity (PGV), such that $\Delta\xi \approx v/c$ and $\Delta\sigma \approx \mu v/c$, where μ is the mean crustal shear modulus (~30×10^9 Pa), v is the PGV (measured by the KiK-net, strong-motion seismograph network installed in boreholes together with the Hi-net sensors), and c is the mean wave phase velocity of the Rayleigh waves that propagate within the upper crust (~3 km/s). The dynamic strain caused by the passing of the seismic waves was one to two orders of magnitude higher than the static coseismic strain for Honshu Island. We thus con-

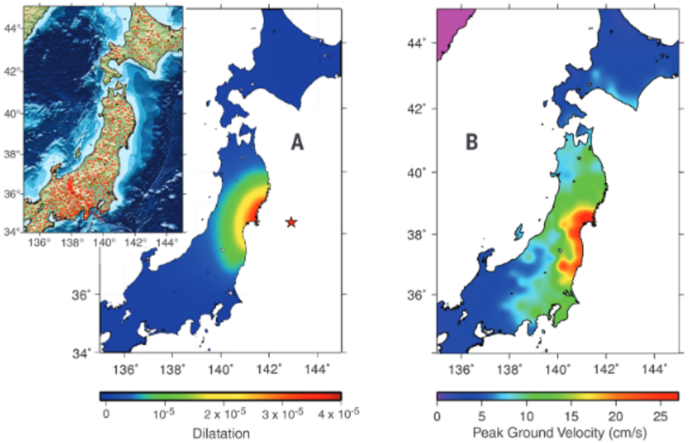

Fig. 1. Static strain and ground shaking caused by the Tohoku-Oki earthquake. (**A**) Modeled coseismic dilatation static strain at 5 km in depth (*7*). The red star shows the position of the epicenter of the Tohoku-Oki earthquake. (Inset) Positions of the Hi-net seismic stations (red points). (**B**) Averaged peak ground velocity measured using the KiK-net strong-motion network (*7*).

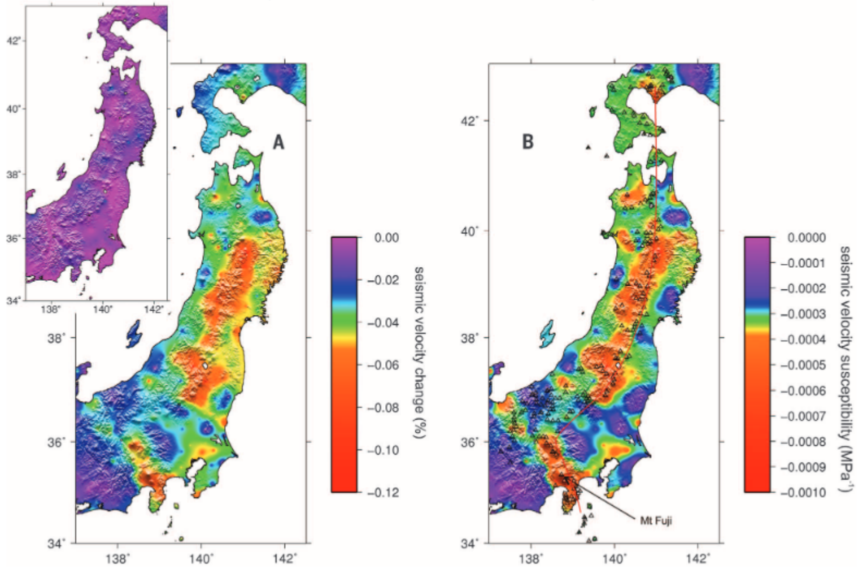

g. 2. Crustal seismic velocity perturbations caused by the Tohoku-Oki earthquake. (**A**) Coseismic crustal seismic velocity changes induced by the 2011 ohoku-Oki earthquake. (Inset) Velocity changes averaged over 5 days preceding the day of the Tohoku-Oki earthquake. (**B**) Seismic velocity susceptibility omputed using the seismic velocity changes shown in (A). Black triangles denote Quaternary period volcanoes, and the red line depicts the main volcanic fronts.

From imaging to monitoring

We used the approach of Gomberg and Agnew (15) to estimate the level of dynamic strain $\Delta\xi$ and dynamic stress $\Delta\sigma$ from the observed peak ground velocity (PGV), such that $\Delta\xi \approx v/c$ and $\Delta\sigma \approx \mu v/c$, where μ is the mean crustal shear modulus (~30×10^9 Pa), v is the PGV (measured by the KiK-net, strong-motion seismograph network installed in boreholes together with the Hi-net sensors), and c is the mean wave phase velocity of the Rayleigh waves that propagate within the upper crust (~3 km/s). The dynamic strain caused

$$\begin{cases} \epsilon_{11} = \partial u_1/\partial x_1 = \dfrac{q}{k}\left(-qe^{-qx_1} + s\dfrac{2k^2}{s^2+k^2}e^{-sx_1}\right) \\ \quad \cdot C\cos[\omega(t - x_2/c)] \\ \epsilon_{22} = \partial u_2/\partial x_2 = \left(e^{-qx_1} - \dfrac{2qs}{s^2+k^2}e^{-sx_1}\right) \\ \quad \cdot (C\omega/c)\cos[\omega(t - x_2/c)] \\ \epsilon_{12} = \dfrac{1}{2}\left(\dfrac{\partial u_1}{\partial x_2} + \dfrac{\partial u_2}{\partial x_1}\right) \\ \quad = \dfrac{1}{2}\left[\dfrac{q}{k}\left(e^{-qx_1} - \dfrac{2k^2}{s^2+k^2}e^{-sx_1}\right)\dfrac{\omega}{c}\right. \\ \quad \left. + \left(qe^{-qx_1} - s\dfrac{2qs}{s^2+k^2}e^{-sx_1}\right)\right] \cdot C\sin[\omega(t - x_2/c)] \end{cases}$$

$$\gamma_{R\max} = \max\left[2\sqrt{\left(\frac{\epsilon_{11} - \epsilon_{22}}{2}\right)^2 + \epsilon_{12}^2}\right]$$

From imaging to monitoring

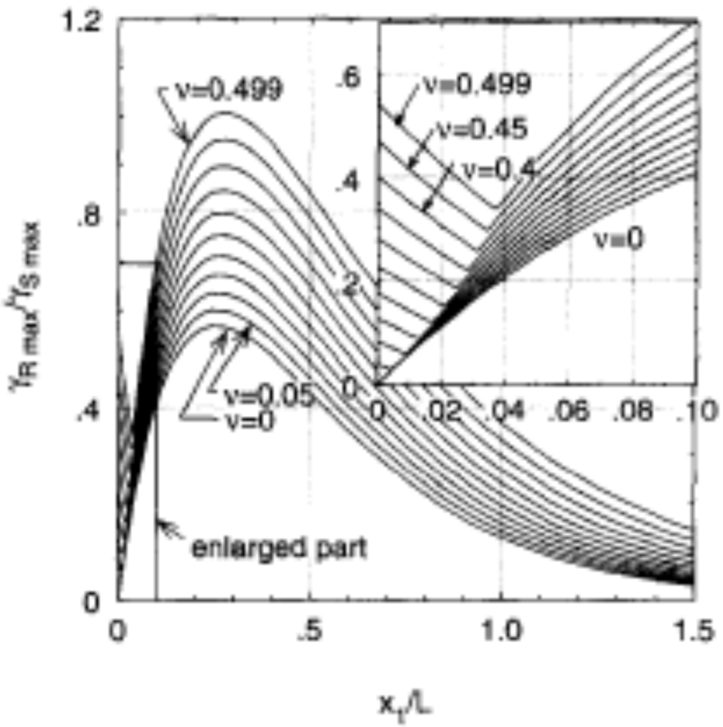

Fig. 1. With a given vertical velocity $\dot{u}_1(x_1 = 0)$ of a material point on the ground surface, the shear strain amplitude $\gamma_{R\max}$ obtained from the equation of the Rayleigh wave is much smaller than the $\gamma_{S\max}$ obtained from the equation of the shear wave. Moreover, the amplitude $\gamma_{R\max}$ changes with the depth and at $x_1/L \approx 0{\cdot}25$ reaches the maximum; e.g. for $\nu = 0{\cdot}2$, this maximum is about 30% smaller than $\gamma_{S\max}$.

However, while this approach is certainly valid for body waves it might be not appropriate for Rayleigh waves.

This means that the Poisson´s ratio should be taken also into account.

This would imply that for different parts of the area under investigation, the values of shear strain should be calculated considering the spatial variability of the Poisson´s ratio.

Influence of source properties

Influence of Wind Turbines on Seismic Records of the Gräfenberg Array

by Klaus Stammler and Lars Ceranna

temporal variability of the raw noise frequency content

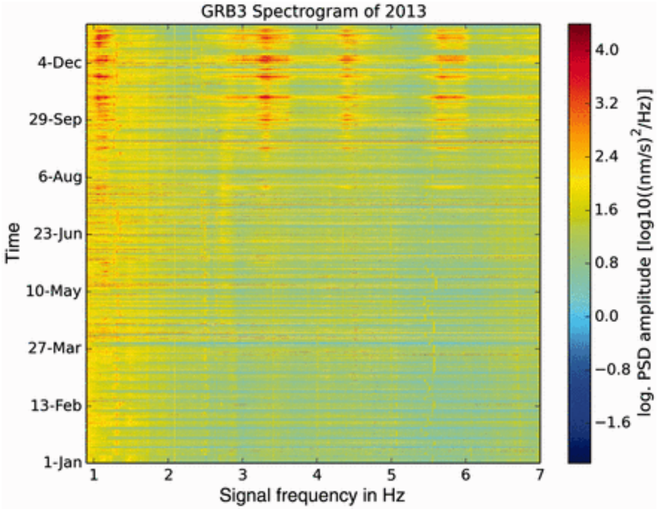

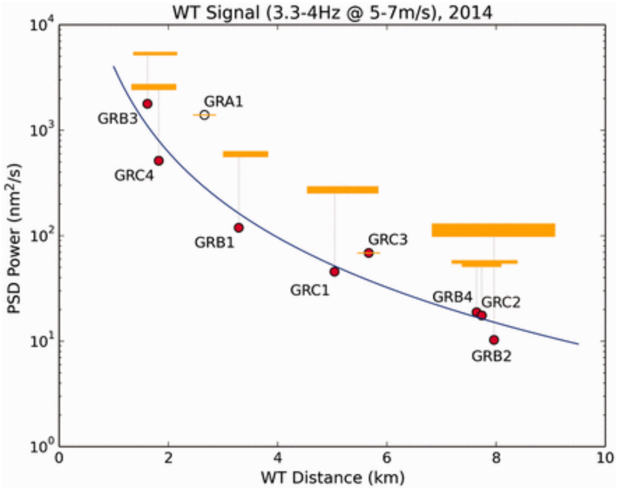

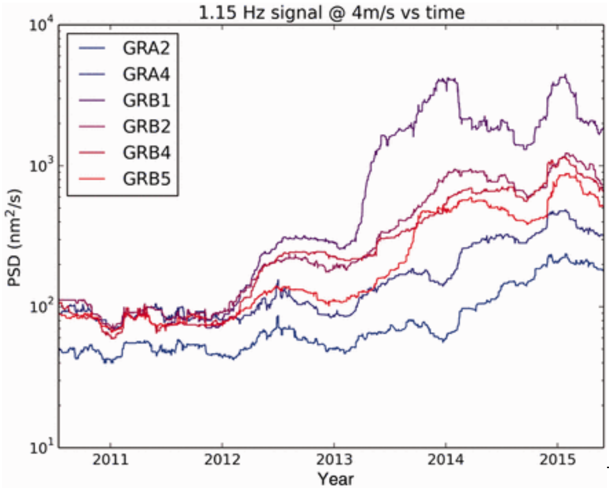

Influence of source properties

Geophysical Journal International
Geophys. J. Int. (2013) **194**, 1574–1581
Advance Access publication 2013 May 27
doi: 10.1093/gji/ggt170

Spurious velocity changes caused by temporal variations in ambient noise frequency content

Zhongwen Zhan, Victor C. Tsai and Robert W. Clayton
Seismological Laboratory, California Institute of Technology, 1200 E. California Blvd., Pasadena, CA 91125, USA. E-mail: zwzhan@gmail.com

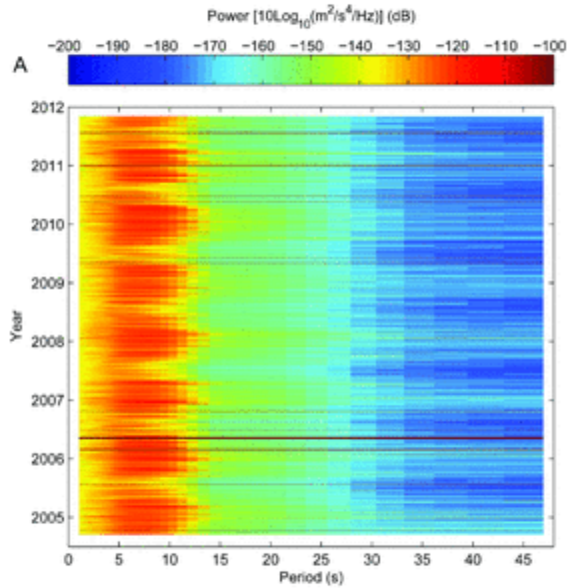

temporal variability of the raw noise frequency content

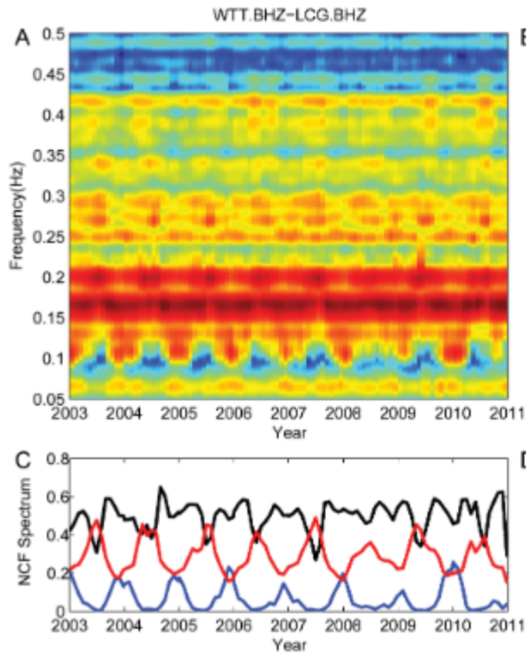

temporal variability of the noise correlation function frequency content

Influence of source properties

J Seismol (2016) 20:921–934
DOI 10.1007/s10950-016-9571-y

ORIGINAL ARTICLE

On the use of the autocorrelation function: the constraint of using frequency band-limited signals for monitoring relative velocity changes

Marco Pilz · Stefano Parolai

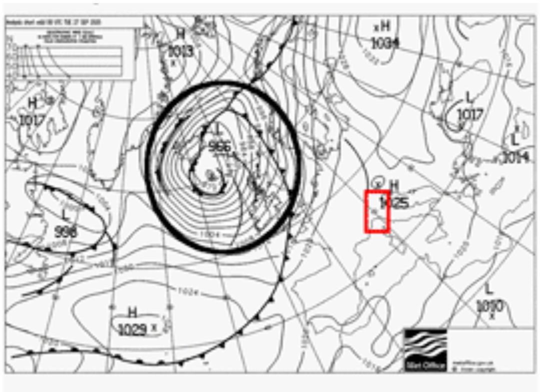

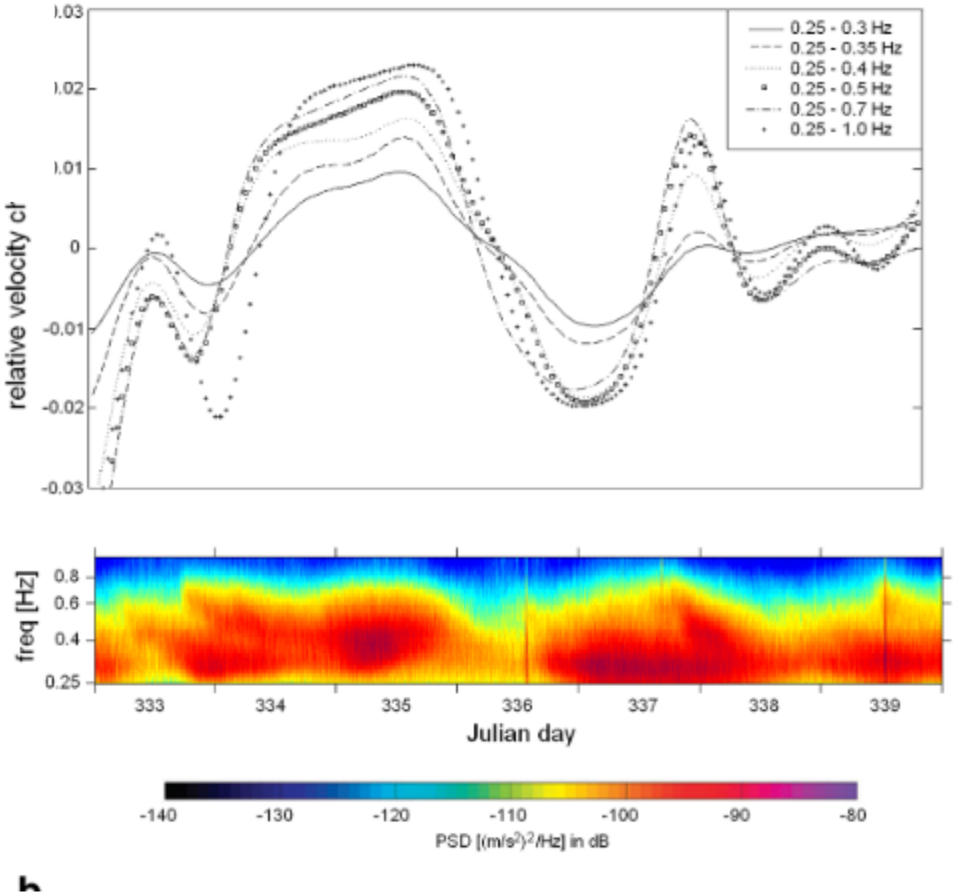

Influence of frequency content and bandwidth

Already early works detected a frequency dependence of the velocity changes.

Geophysical Journal International

Geophys. J. Int. (2010) 181, 985–996 doi: 10.1111/j.1365-246X.2010.04550.x

Detecting seasonal variations in seismic velocities within Los Angeles basin from correlations of ambient seismic noise

Ueli Meier,* Nikolai M. Shapiro and Florent Brenguier
Institut de Physique du Globe de Paris, Equipe de Sismologie 4 Place Jussieu Case 89, 75252 Paris cedex 05, France. E-mail: meierue@ipgp.jussieu.fr

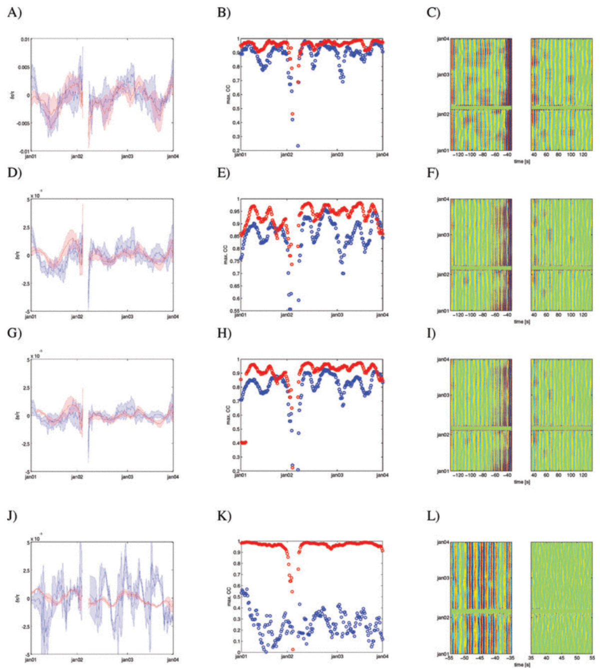

Influence of frequency content and bandwidth

Temporal Variations of Seismic Velocity at Paradox Valley, Colorado, Using Passive Image Interferometry

by Arantza Ugalde, Beatriz Gaite, and Antonio Villaseñor

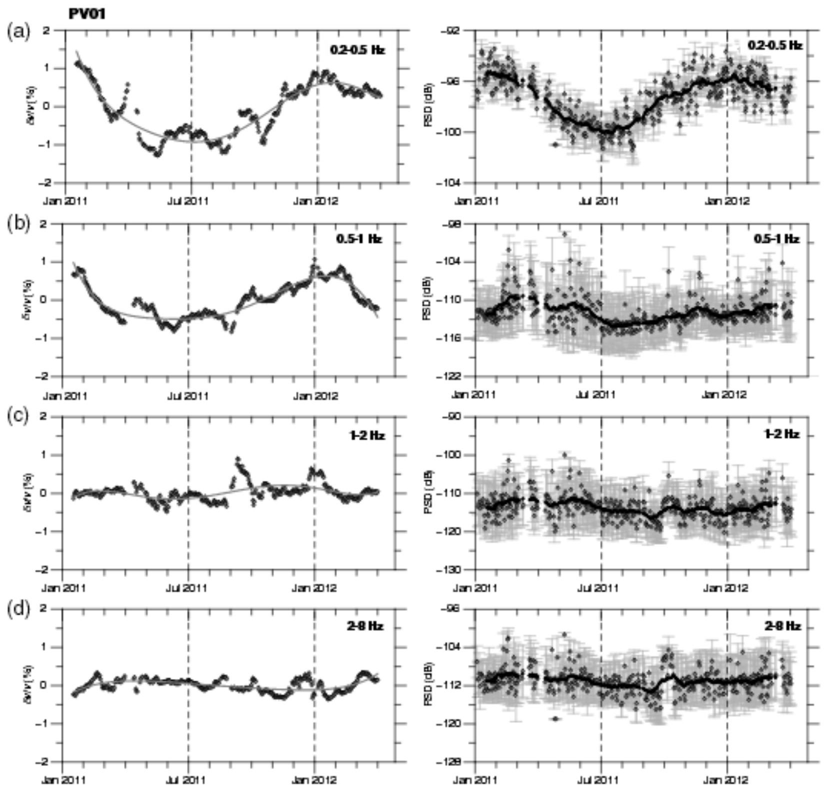

Figure 7. (a–d, left panels) Relative velocity variations at station PV01 for the studied frequency range using the MWCS technique; the gray solid line plots the long-term variation. (a–d, right panels) Amplitude of the PSD function of seismic noise and standard deviation at station PV01 for four frequency ranges from 0.2 to 8 Hz. The solid line is the 30-day data running average.

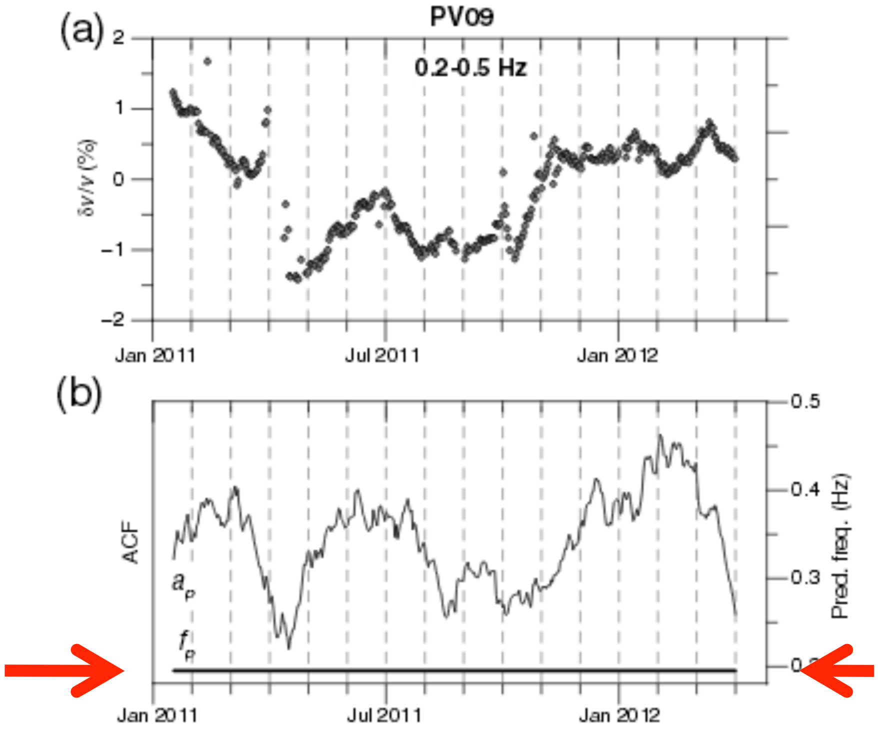

Figure 8. (a) Relative velocity variations at station PV09 using the MWCS technique; and (b) spectral amplitude and predominant frequency of the ACF for the 0.2–0.5 frequency range.

Influence of frequency content and bandwidth

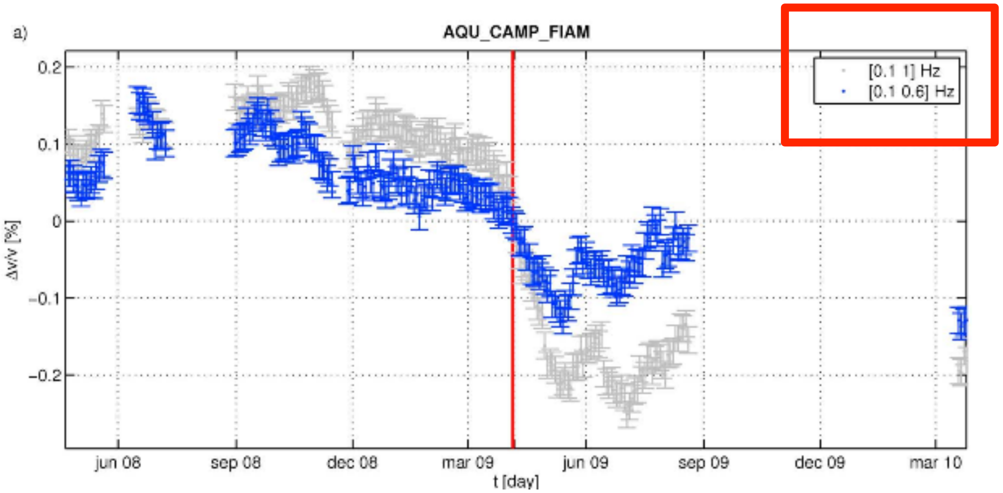


GEOPHYSICAL RESEARCH LETTERS, VOL. 38, L24304, doi:10.1029/2011GL049750, 2011

Variations of crustal elastic properties during the 2009 L'Aquila earthquake inferred from cross-correlations of ambient seismic noise

L. Zaccarelli,[1] N. M. Shapiro,[1] L. Faenza,[2] G. Soldati,[2] and A. Michelini[2]

Received 21 September 2011; revised 7 November 2011; accepted 8 November 2011; published 17 December 2011.

Similar observations in many further publications but no discussion about the theoretical background!

Influence of frequency content and bandwidth

There is a significant influence of the processing!

Inherent properties of the ACF

The autocorrelation has always zero phase!

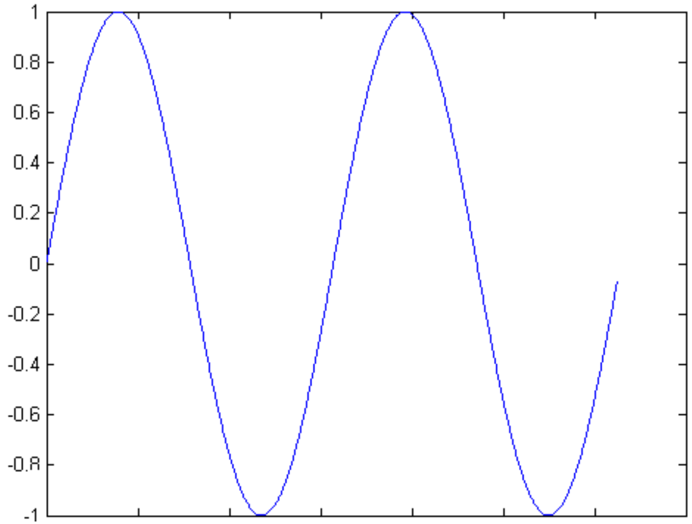

pure sinusoid

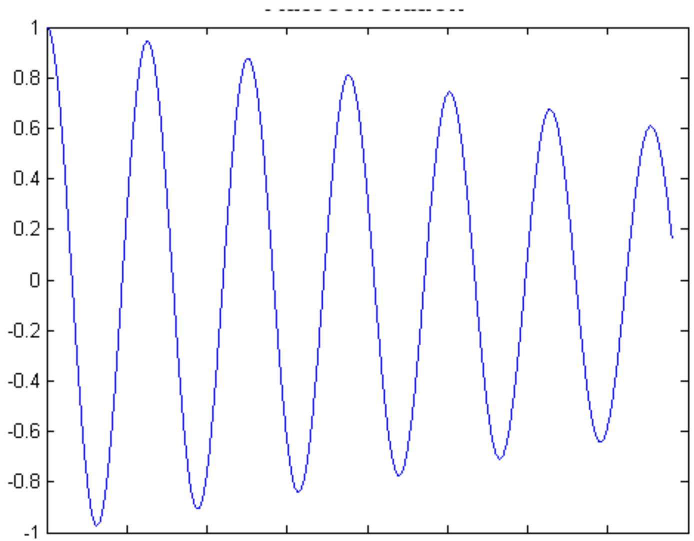

corresponding ACF

Inherent properties of the ACF

The autocorrelation has always zero phase!

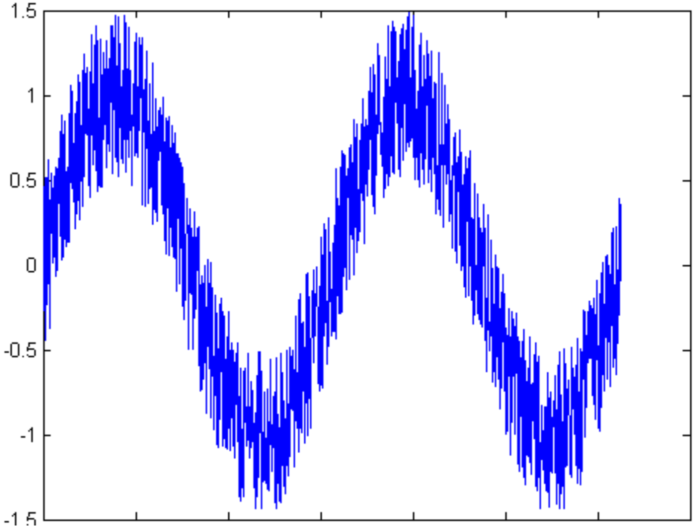

add noise

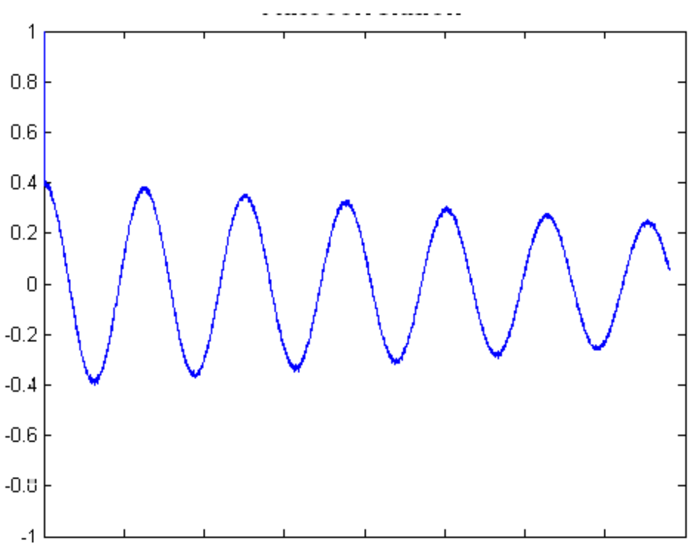

corresponding ACF
still zero phase

Influence of frequency content and bandwidth

However, such influence is already known for a long time!

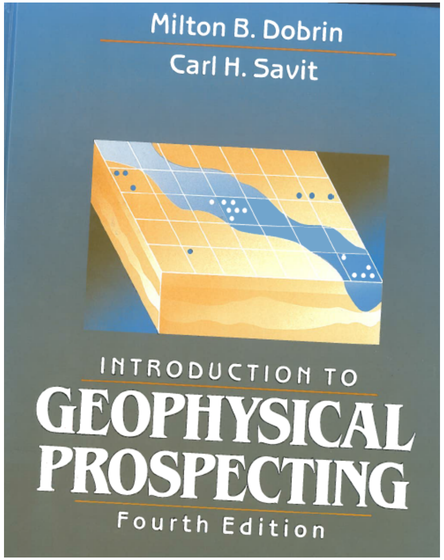

Frequency Spectrum and Time Resolution

FIGURE 7-3 Determination using convolution theorem of waveform corresponding to a symmetrical frequency spectrum with flat response from 10 to 90 Hz and sharp cutoffs at both limits. Narrowness of resultant pulse (upper right) should result in good resolution.

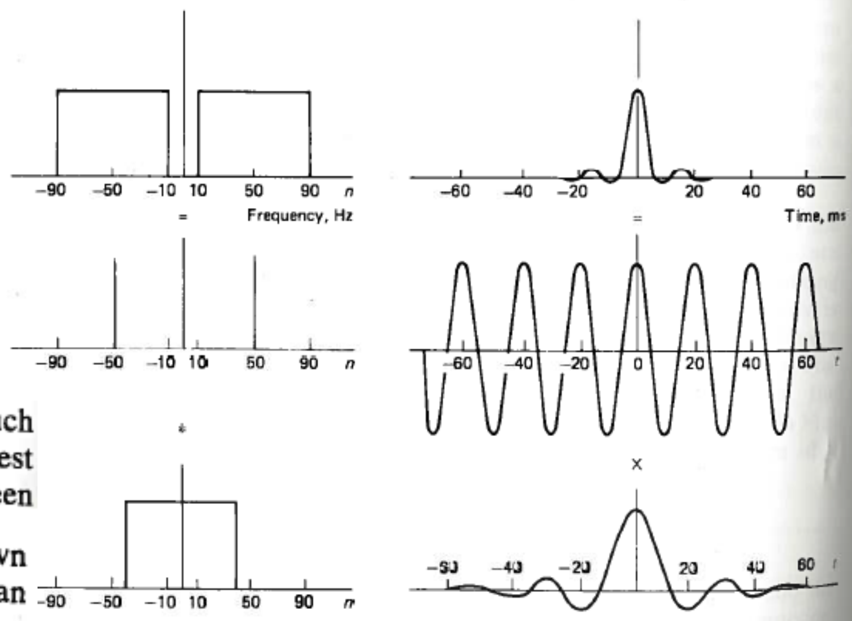

As the frequency content of reflections with which we work is seldom much below 10 Hz or above 90 Hz, the frequency spectrum representing the best resolution we can normally expect consists of a pair of rectangles lying between these limits on the positive and negative sides of the frequency axis, as shown in Fig. 7-3. This spectrum can be obtained by convolving the transform of an infinitely long cosine wave having a frequency of 50 Hz with a rectangular frequency function 80 Hz in breadth. The time signal corresponding to the rectangular frequency function is a sinc function with a central peak 0.025 s wide having side bands 0.0125 s in breadth. Multiplying this by a cosine wave with a period of 0.020 s (the reciprocal of 50 Hz) results in a pulse 0.010 s wide at its first zero crossings. This waveform represents the best resolution that can be expected from a reflection signal traveling in a medium that passes frequencies from 10 to 90 Hz.

Influence of frequency content and bandwidth

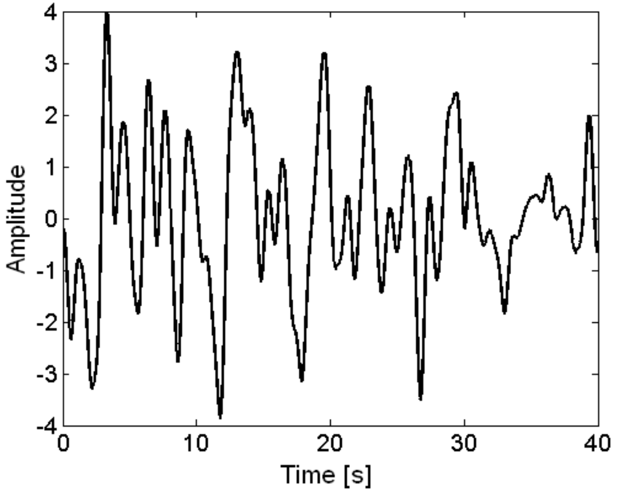

Synthetic time series as a sum of four different sinusoids with different but constant amplitude and frequency values

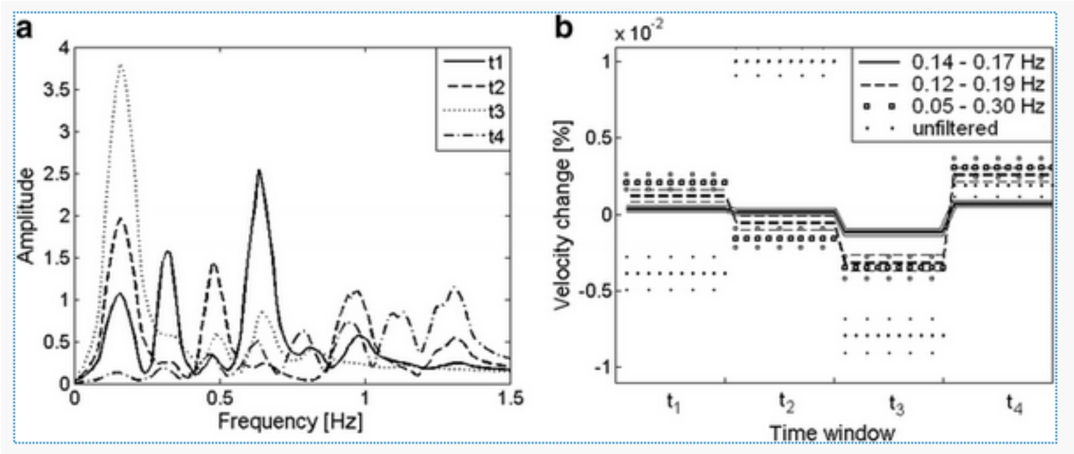

Influence of frequency content and bandwidth

There is a theoretical limit on the resolution of narrow-band filtered signals.

$$\sigma_{\mathcal{T}} = \Delta(\Delta t) = \sqrt{\frac{3}{2\pi^2 T f_0^3 \left(B^3 + 12B\right)} \left(\frac{1}{\rho^2}\left(1 + \frac{1}{\mathrm{SNR}^2}\right)^2 - 1\right)}$$

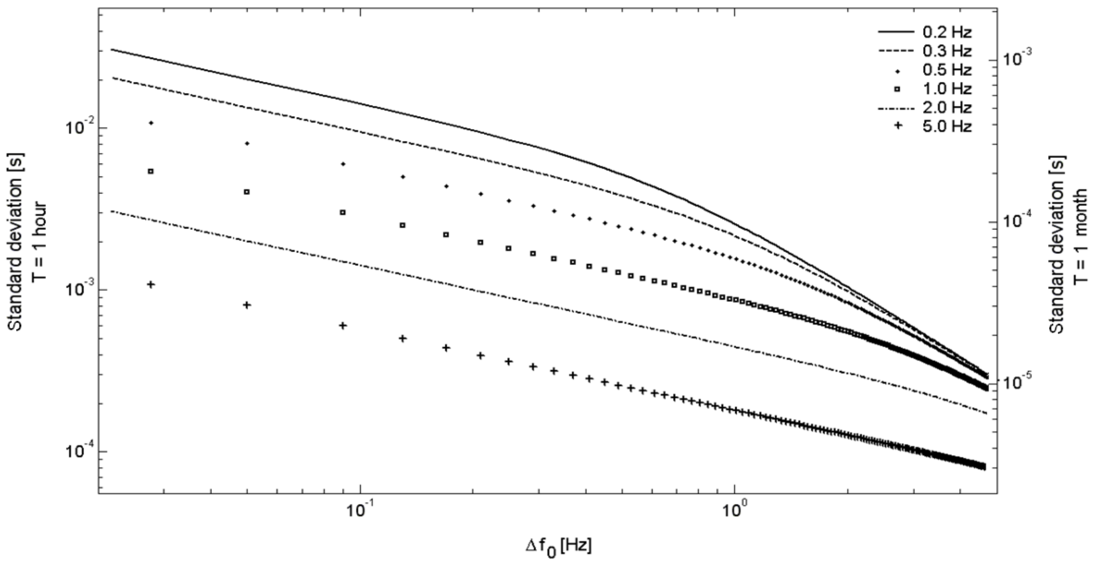

J Seismol (2016) 20:921–934
DOI 10.1007/s10950-016-9571-y

ORIGINAL ARTICLE

On the use of the autocorrelation function: the constraint of using frequency band-limited signals for monitoring relative velocity changes

Marco Pilz · Stefano Parolai

Using narrow filters with a width of <0.1 Hz and correspondingly small dominant frequencies (f <<1 Hz), the uncertainty in relative velocity variation estimates reaches up to 0.1 % even for long correlated time series with a length of several days!

Time-resolved 3D tomography

Fast inversion algorithms allow the 4D monitoring of the shallow subsurface

Given stable noise conditions and sufficiently fast converging Green´s functions

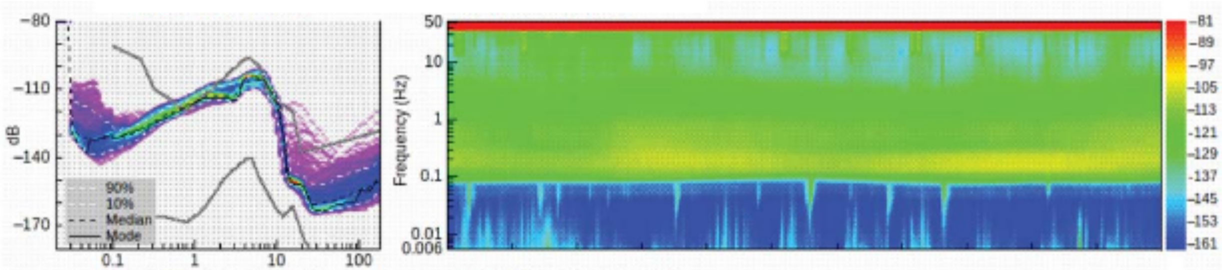

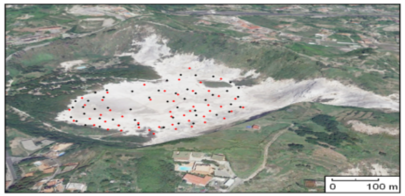

Solfatara crater (Italy)

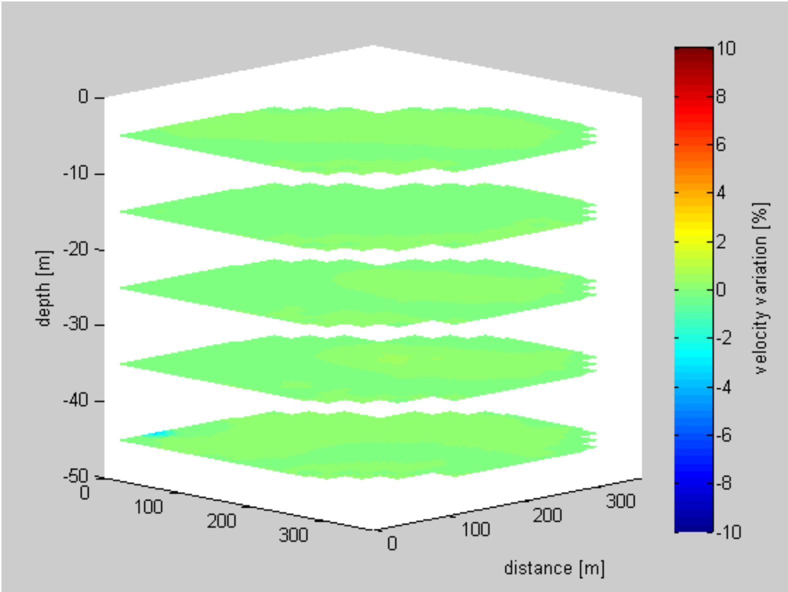

precise location of velocity changes in 3D

fast inversion algorithms needed

Multi-parameter early warning

Technical Data	
Size	from 100 x 160 x 60 to 220 x 140 x 70 mm
Weight	from 0.75 to 2 kg
2 x WLAN	2.4 GHz / 5.0 GHz
Power Supply	5V DC
ADC	3 or 6 x ADC (24Bit)
Sensors	Ext. Seismometer, Camera, Temp. Humidity, GPS, ...,

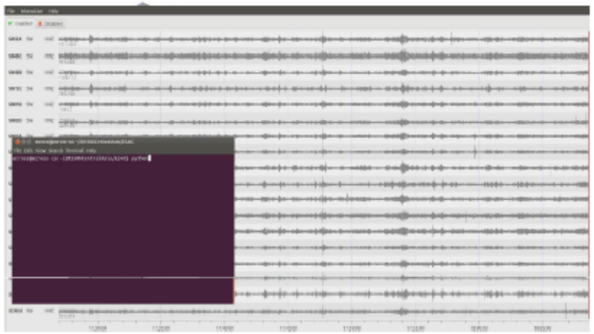

Multi-parameter early warning

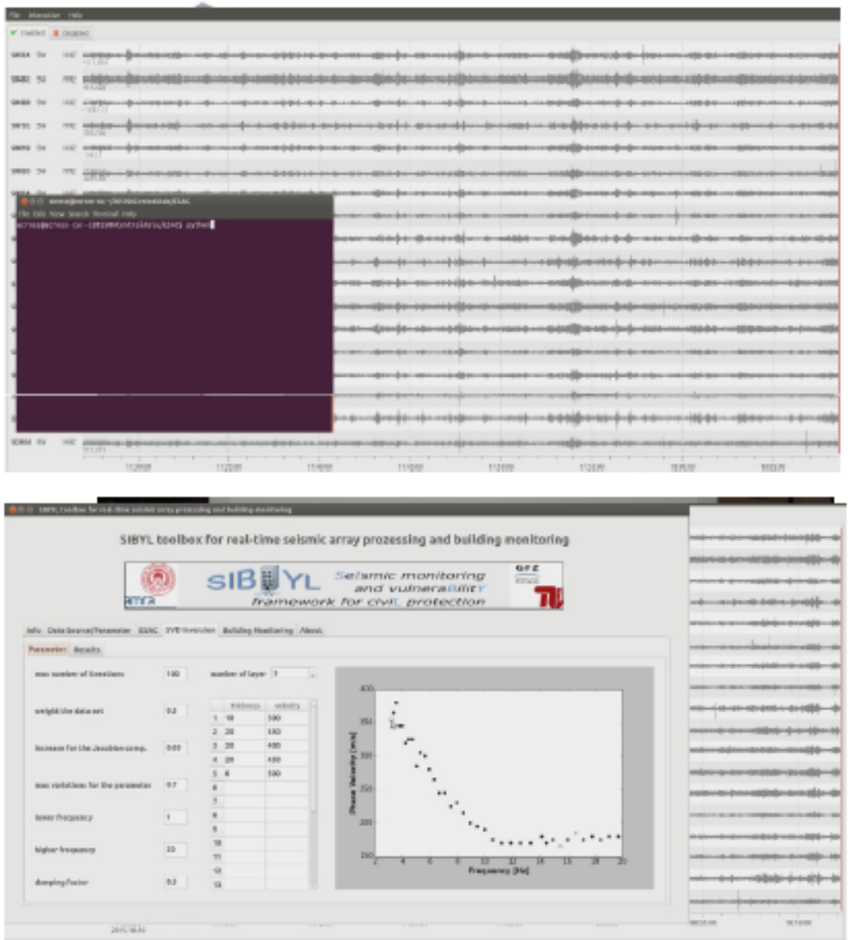

Sensor layer:
- standard strong motion and weak motion sensor
- broadband seismic sensors
- MEMS sensor including accelerometer and gyroscope
- camera
- temperature and humidity sensor
- low cost GNSS system

Communication layer:
- self organizing wireless network
- WLAN on the local scale
- UMTS

Continuous scenario update and calculations on the sensor level

Webinterface for configuration, network information and monitoring the status of acquisition

Real time monitoring

Of course, such monitoring approaches can be applied not only to the ground but also for buildings.

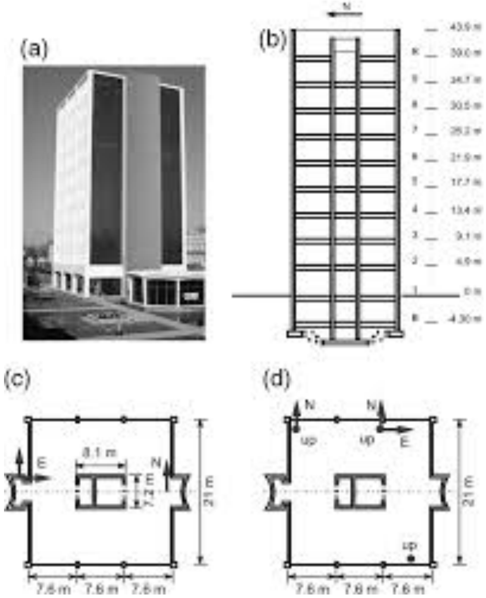

Millikan library, Pasadena, California

Monitoring of the building stock

Extracting the Building Response Using Seismic Interferometry: Theory and Application to the Millikan Library in Pasadena, California

by Roel Snieder and Erdal Şafak

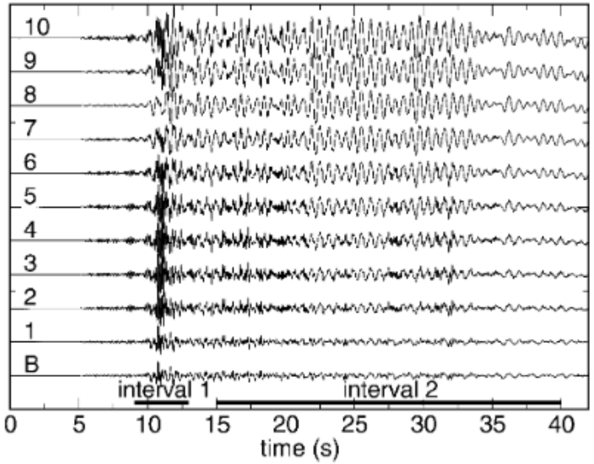

Figure 3. The north–south component of acceleration in the west side of the Millikan Library after the Yorba Linda earthquake of 3 September 2002 (M_L 4.8; time, 02:08:51 PDT; 33.917° N 117.776° W; depth, 3.9 km). The traces are labeled with the floor number (B indicates basement).

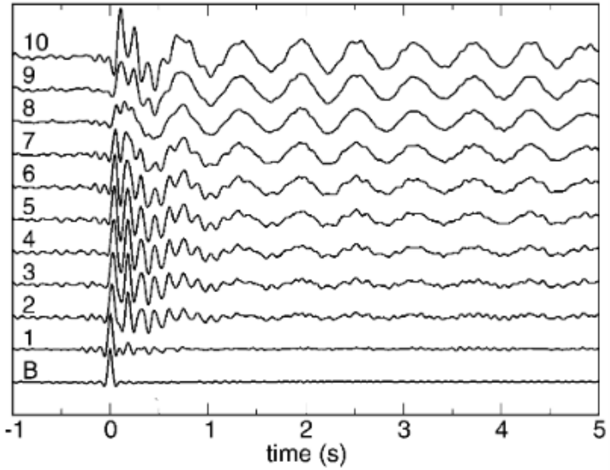

Figure 4. The waveforms of Figure 3 at the different floors after deconvolution with the waves recorded in the basement.

Monitoring of the building stock

Extracting the Building Response Using Seismic Interferometry: Theory and Application to the Millikan Library in Pasadena, California

by Roel Snieder and Erdal Şafak

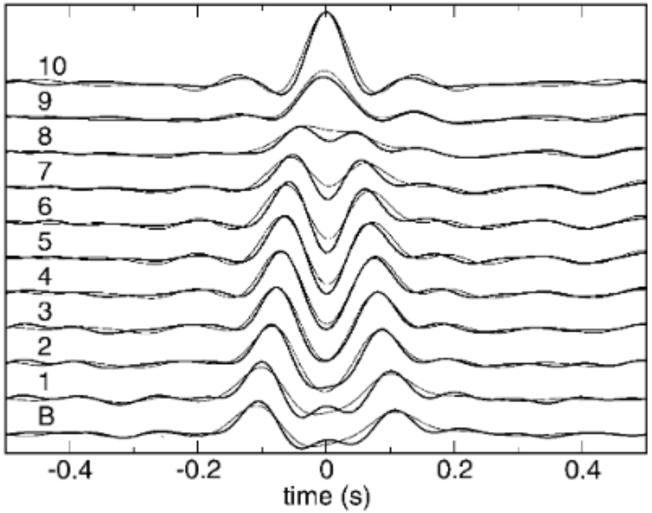

Figure 7. The waveforms of Figure 3 at the different floors after deconvolution with the waves recorded in the top floor using only part of the data of Figure 3. The deconvolved waves shown in thick lines are obtained by using only the data in interval 1 of Figure 3, whereas the deconvolved waves shown in the thin lines are computed from the data in interval 2.

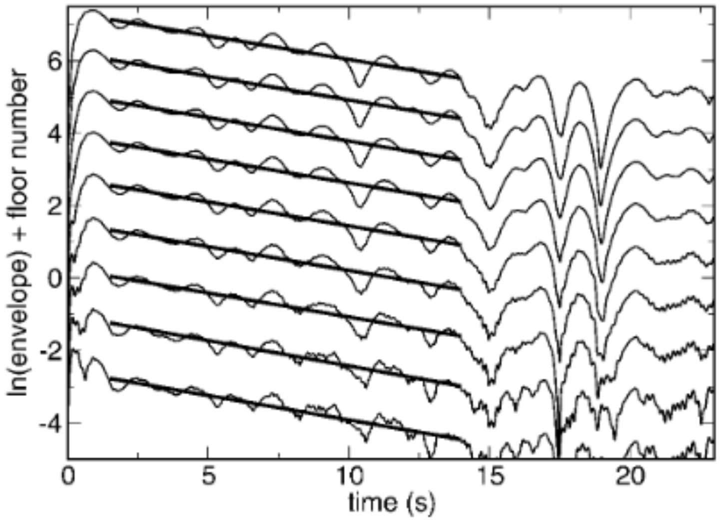

Figure 12. The natural logarithm of the envelope of the deconvolved waves in Figure 4 after applying a bandpass filter with corner frequencies of 1 Hz and 3 Hz, respectively. For clarity the floor number is added to each curve. The best-fitting straight line to each curve is indicated with thick solid lines.

Monitoring of the building stock

ELSEVIER

Soil Dynamics and Earthquake Engineering 28 (2008) 387–404

SOIL DYNAMICS AND EARTHQUAKE ENGINEERING

www.elsevier.com/locate/soildyn

Earthquake damage detection in the Imperial County Services Building III: Analysis of wave travel times via impulse response functions

Maria I. Todorovska*, Mihailo D. Trifunac

Department of Civil Engineering, University of Southern California, Los Angeles, CA 90089-2531, USA

Received 4 May 2006; received in revised form 16 June 2007; accepted 1 July 2007

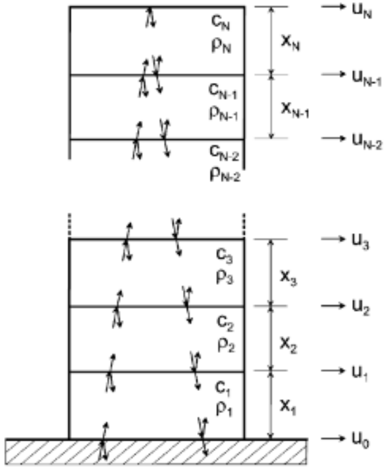

Fig. 1. The model.

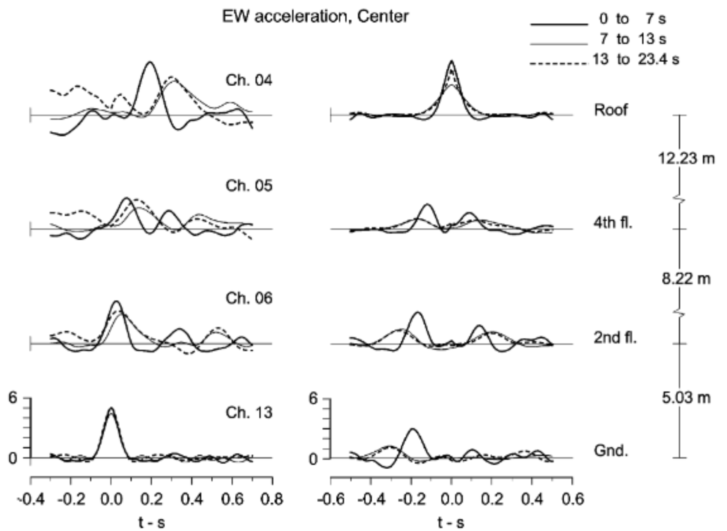

Fig. 8. Impulse response functions for EW motions and for input impulse at the ground floor (left) and at the roof (right).

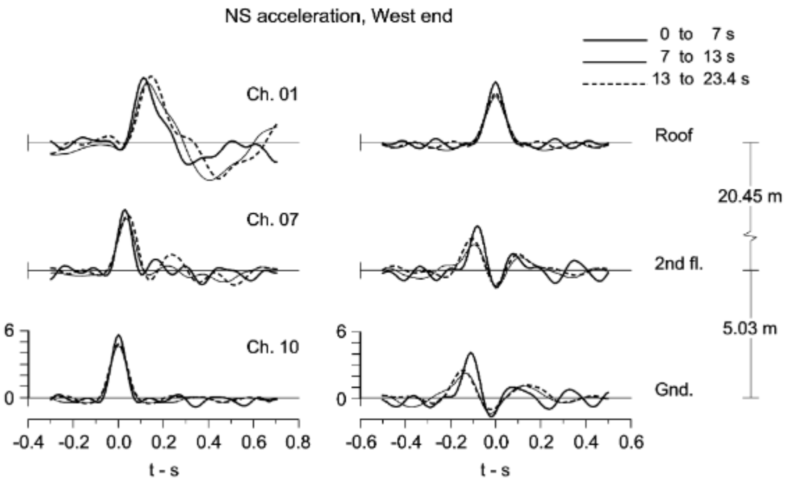

Fig. 9. Same as Fig. 8 but for NS motions recorded at the west side of the building.

Monitoring of the building stock

Also here, a lot of the work has already been done in the past.

Bulletin of the Earthquake
Research Institute
Vol. 41 (1963), pp. 825-833

50. *Some New Problems of Seismic Vibrations of a Structure. Part 1.*

By Kiyoshi Kanai and Shizuyo Yoshizawa,

Earthquake Research Institute.

(Read Oct. 15, 1946 and Sept. 17, 1963.—Received Sept. 30, 1963.)

Monitoring of the building stock

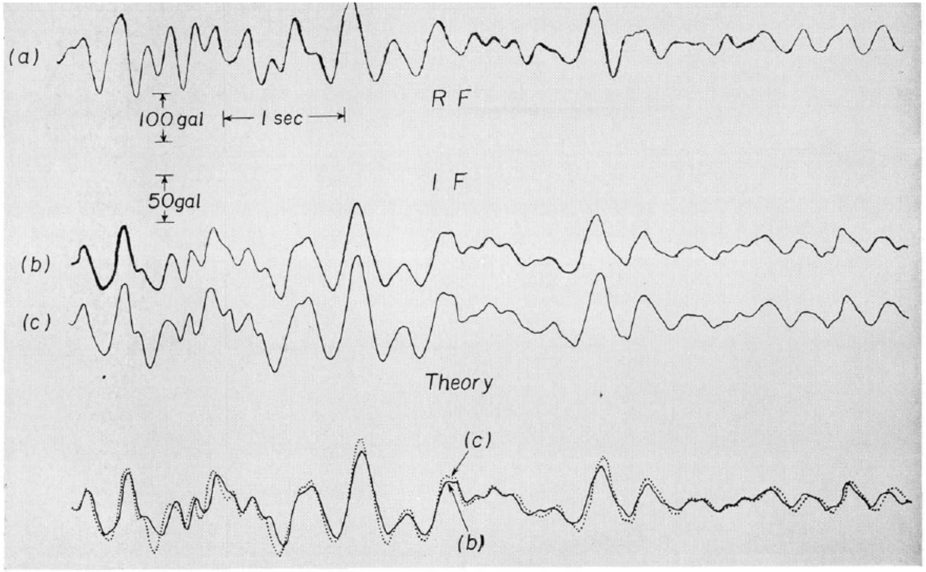

Fig. 7b. M Building. EW component. Original ×2.5. RF; roof floor, 1F; first floor.

Some New Problems of Seismic Vibrations of a Structure.

By

Kiyoshi KANAI.*

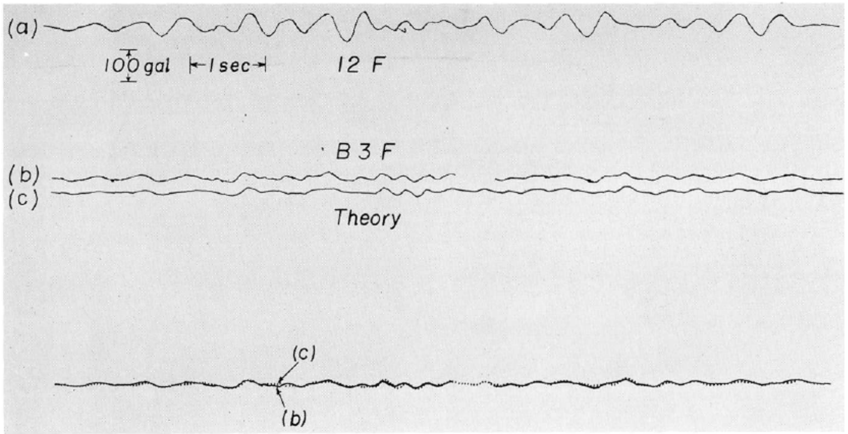

Fig. 8a. K Building. NS component. Original ×1.5. 12F; twelfth floor, B3F; basement third floor.

Combining recordings in buildings and underground

Joint Deconvolution of Building and Downhole Strong-Motion Recordings: Evidence for the Seismic Wavefield Being Radiated Back into the Shallow Geological Layers

by Bojana Petrovic and Stefano Parolai

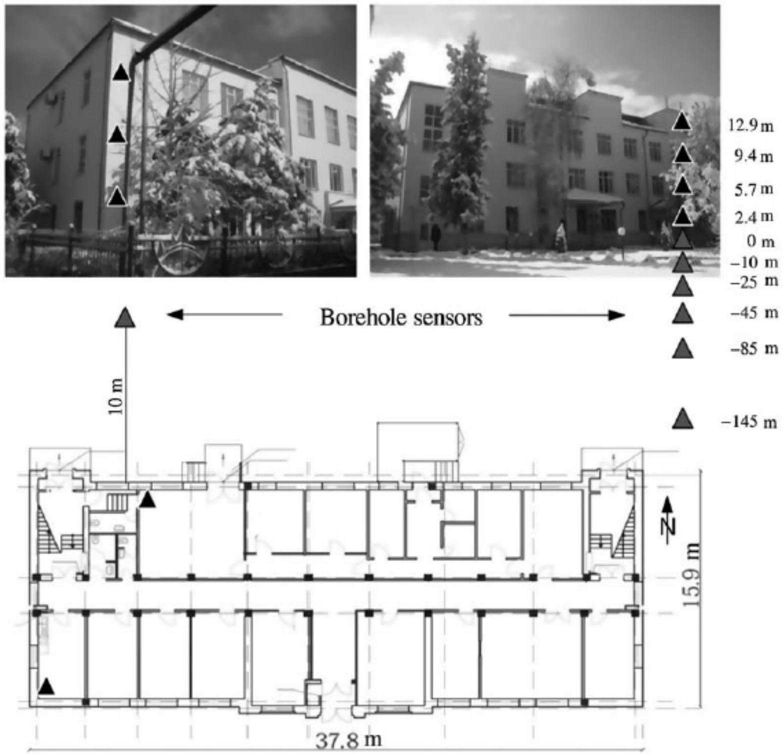

Combining recordings in buildings and underground

6

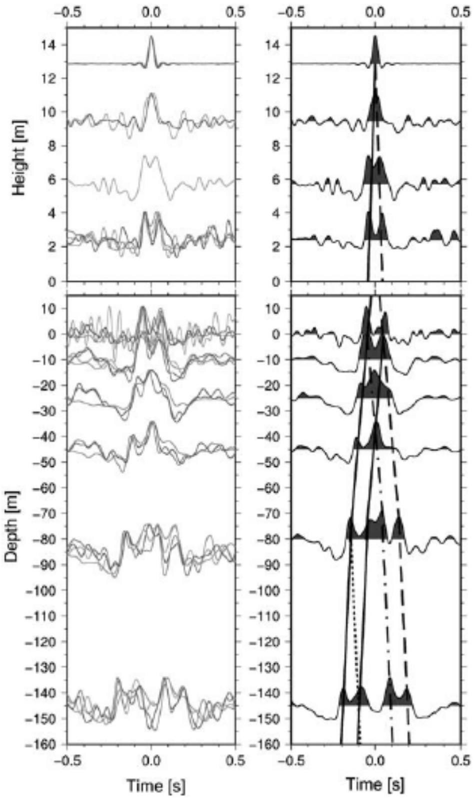

Figure 4. (Left panel) Deconvolved wavefields obtained for the north–south component of ground motion arising from the four considered events (Table 1) using the recordings from the top of the building as the reference. There is only one line at 6 m, because the sensor at the 2nd floor had some problems and hence, registered only one of the four analyzed earthquakes. (Right panel) The results obtained after stacking the results shown in the left panel. The upward-going waves (black lines), the downward-going waves reflected at the interface at 75 m depth (black-dotted line), at the Earth's surface (black dashed-dotted line) and at the top of the building (dashed line) are also shown.

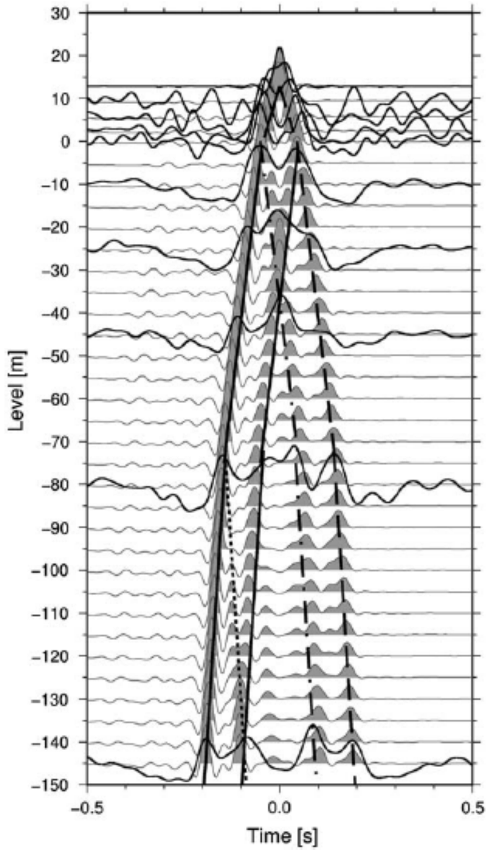

Figure 6. Deconvolved wavefield obtained by the use of synthetic seismograms (gray) and the observed data after stacking the results of all events (black). The upward propagating waves (black lines), the downward-going waves reflected at the interface at 75 m depth (black-dotted line), at the Earth's surface (black dashed-dotted line) and at the top of the building (dashed line) are also shown.

Some remarks

In the end, it is not important what you do but you have to do it properly.

Think about the available techniques but also about their theoretical limitations.

Already in the past, a lot of work has been done and has been published. Refer to the old papers.

Space and time spectra of stationary stochastic waves, with special reference to microtremors
K Aki - 1957 - repository.dl.itc.u-tokyo.ac.jp
ここで複雑な波動というのは，stationary stochastic wave と呼ぶべきものである．
これまで地震記象は位相的な立場から主に解析されて来ているが，位相的には取扱い得ない波動も
地震学の分野には数多くある．たとえば，地震波のなかの複雑な部分，脈動，常時微動，火山微動 …
Cited by 1074

Publication List of Keiiti Aki

Compiled by T. Miyatake[1]

SELECTED PUBLICATIONS:

Aki, K. (1965). Maximum likelihood estimate of b in the formula log N=a-bM and its confidence limits, *Bull. Earthq. Res. Inst., Univ. Tokyo*, **43**, 237-239.

Aki, K. (1966). Generation and propagation of G waves from the Niigata earthquake of June 16, 1964: Part 2. Estimation of earthquake moment, released energy and stress drop from the G wave spectra, *Bull. Earthq. Res. Inst., Univ. Tokyo*, **44**, 73-88.

Aki, K. (1967). Scaling law of seismic spectra, *J. Geophys. Res.*, **72**, 1217-1231.

Aki, K. (1968). Seismic displacement near a fault, *J. Geophys. Res.*, **73**, 5359-5376.

Aki, K. (1969). Analysis of the seismic coda of local earthquakes as scattered waves, *J. Geophys. Res.*, **74**, 6215-6231.

Aki, K. and B. Chouet (1975). Origin of coda waves: source, attenuation and scattering effects, *J. Geophys. Res.*, **80**, 3322-3342.

Aki, K. and W. H. K. Lee (1976). Determination of three dimensional velocity anomalies under a seismic array using first P arrival times from local earthquakes, 1. A homogeneous initial model, *J. Geophys. Res.*, **81**, 4381-4399.

Aki, K., A. Christofferson, and E. S. Husebye (1977). Determination of the three-dimensional seismic structure of the lithosphere, *J. Geophys. Res.*, **82**, 277-296.

Aki, K., M. Fehler, and S. Das (1977). Source mechanism of volcanic tremors: fluid driven crack models and their application to the 1963 Kilauea eruption, *J. Volcanol. Geotherm. Res.*, **2**, 259-287.

Aki, K. (1979). Characterization of barriers on an earthquake fault, *J. Geophys. Res.*, **84**, 6140-6148.

Aki, K. and P. Richards (1980). "Quantitative Seismology: theory and methods", Freeman, San Francisco, 932 pp.

Aki, K. (1980). Attenuation of shear waves in the lithosphere for frequencies from 0.05 to 25 Hz, *Phys. Earth Planet. Inter.*, **21**, 50-60.

Papageorgiou, A. S. and K. Aki (1983). A specific barrier model for the quantitative description of inhomogeneous faulting and prediction of strong ground motion, Part I and II, *Bull. Seis. Soc. Am.*, **73**, 693-722, and 953-978.

Aki, K. (1993). Local site effects on weak and strong ground motion, *Tectonophysics*, **218**, 93-111.

Li, Y. G., K. Aki, D. Adams, A. Hasemi, and W. H. K. Lee (1994). Seismic guided waves trapped in the fault zone of the Landers, California, earthquake of 1992, *J. Geophys. Res.*, **99**, 11705-11722.

Aki, K. (1996). Scale dependence in earthquake phenomena and its relevance to earthquake prediction, *Proc. Natl. Acad. Sci., USA*, **93**, 3740-3747.

More than 200 papers but no paper in *Nature* or *Science*!